GROWTH AND CHARACTERIZATION OF ULTRATHIN InAs/GaAs AND GaSb/GaAs QUANTUM WELLS

by

Oliver James Pitts

B.Sc., McGill University, 1996

THESIS SUBMITTED IN PARTIAL FULFILLMENT

OF THE REQUIREMENTS FOR THE DEGREE OF

DOCTOR OF PHILOSOPHY

IN THE DEPARTMENT

OF

PHYSICS

SIMON FRASER UNIVERSITY

February 2004

APPROVAL

Name:	Oliver James Pitts
Degree:	Doctor of Philosophy
Title of Thesis:	Growth and Characterization of Ultrathin InAs/GaAs and GaSb/GaAs Quantum Wells
Examining Committee:	Howard D. Trottier, Professor, Department of Physics (Chair)

Simon P. Watkins (Senior Supervisor)
Professor, Department of Physics

Colombo R. Bolognesi (Supervisor)
Professor, Department of Physics and School of Engineering Science

Michael L. W. Thewalt (Supervisor)
Professor, Department of Physics

Karen L. Kavanagh (Internal Examiner)
Professor, Department of Physics

Thomas Tiedje (External Examiner)
Professor, Department of Physics and Astronomy, University of British Columbia

Date Approved: February 12, 2004

PARTIAL COPYRIGHT LICENSE

I hereby grant to Simon Fraser University the right to lend my thesis, project or extended essay (the title of which is shown below) to users of the Simon Fraser University Library, and to make partial or single copies only for such users or in response to a request from the library of any other university, or other educational institution, on its own behalf or for one of its users. I further agree that permission for multiple copying of this work for scholarly purposes may be granted by me or the Dean of Graduate Studies. It is understood that copying or publication of this work for financial gain shall not be allowed without my written permission.

Title of Thesis/Project/Extended Essay

GROWTH AND CHARACTERIZATION OF ULTRATHIN InAs/GaAs AND GaSb/GaAs QUANTUM WELLS

Author: _____
(signature)

_____
(name)

_____
(date)

Abstract

GaSb/GaAs and InAs/GaAs multiple quantum wells are grown by organometallic vapour phase epitaxy and characterized by x-ray diffraction, transmission electron microscopy and photoluminescence spectroscopy. Reflectance-difference spectroscopy is used to identify a characteristic signature of Sb on the GaAs (001) surface and to show that Sb has a strong tendency to segregate to the surface. The incorporation of Sb results in a graded GaAs-on-GaSb interface which is well described by a one-dimensional model with a segregation coefficient of ~ 0.95. Desorption of the surface Sb layer is enhanced by exposure to tertiarybutylarsine; the interface abruptness is dramatically increased by employing a flashoff sequence in which the accumulated Sb is desorbed prior to GaAs overgrowth. Atomic force microscope images show that the transition from planar GaSb growth on GaAs to island formation occurs for a submonolayer coverage under equilibrium conditions. If the layer is immediately capped by GaAs overgrowth, however, a monolayer of GaSb can be grown without dots forming. Low-temperature photoluminescence spectra of abrupt and graded GaSb/GaAs quantum wells are compared; the luminescence line is at a lower energy for the more abrupt structures. For InAs/GaAs quantum wells, the luminescence line is at a higher energy than for the GaSb/GaAs quantum wells. The experimentally determined transition energies are compared with calculations using the envelope function approximation.

Acknowledgments

I would like to thank my senior supervisor, Prof. Simon Watkins, for making this work possible and for his guidance and support during my research.

James Stotz worked tirelessly to obtain the photoluminescence spectra reported herein and was always happy to take on a new batch of samples. I would also like to acknowledge Thomas Meyer for providing additional data and Prof. Mike Thewalt for the use of his laboratory and for helpful discussions on the interpretation of the photoluminescence data. Victoria Fink prepared numerous cross-sectional samples and recorded the transmission electron microscope images presented in this thesis. Prof. Karen Kavanagh was very helpful in discussing the interpretation of these images and her enthusiasm was particularly encouraging.

I would also like to thank a number of other researchers I have had the pleasure of collaborating with during my studies at Simon Fraser University: Rod Wiersma, Chengxin Wang, Rao Tatavarti, Michael Chen, Martin Dvorak, Georg Soerensen, and Prof. Colombo Bolognesi.

Contents

List of Tables

List of Figures

List of Abbreviations

2D two-dimensional

3D three-dimensional

AFM atomic force microscope

ALE atomic layer epitaxy

APD avalanche photodiode

CAS calorimetric absorption spectroscopy

CBM conduction band minimum

EFA envelope function approximation

EPD excitation power density

FCC face-centred cubic

FME flow rate modulation epitaxy

FWHM full width at half-maximum

GIXS grazing incidence x-ray scattering

GRI growth interruption

KP Kronig-Penney

LEED low-energy electron diffraction

LEO linear electro-optic

LO longitudinal optical

LT-GaAs low-temperature-grown GaAs

MBE molecular beam epitaxy

MEE migration enhanced epitaxy

MET macroscopic elasticity theory

MFC mass flow controller

ML monolayer

MQW multiple quantum well

OMVPE organometallic vapour phase epitaxy

PEM photoelastic modulator

PL photoluminescence

RD reflectance-difference

RDS reflectance-difference spectroscopy

RHEED reflection high-energy electron diffraction

RMS root-mean-square

SFU Simon Fraser University

SQW single quantum well

STM scanning tunnelling microscopy

STP standard temperature and pressure

TBAs tertiarybutylarsine

TBP tertiarybutylphosphine

TEGa triethylgallium

TEM transmission electron microscopy

TMIn trimethylindium

TMSb trimethylantimony

UHV ultra-high vacuum

VBM valence band maximum

XAFS x-ray absorption fine structure

XPS x-ray photoelectron spectroscopy

XRD x-ray diffraction

XSW x-ray standing wave

Chapter 1

Introduction

Semiconductor quantum wells are a practical realization of the textbook example of a particle confined in a square potential. In a semiconductor quantum well, charge carriers (electrons or holes, or both) are confined in a thin layer of a semiconductor material bounded on both sides by barrier layers of a different material. The resulting quantized energy levels give the quantum well structure electronic and optical properties which are fundamentally different from those of the constituent materials. Far from being confined to the academic interest in the basic properties of this model quantum mechanical system, the study of such structures has resulted in major advances in technology, particularly the now widespread semiconductor quantum well laser. Research on semiconductor quantum wells dates back to the initial proposal of a superlattice structure by Esaki and Tsu [1] in 1969, and there is now a large body of literature on the subject. Current research continues on a number of topics, including confinement in two and three dimensions (quantum wires and quantum dots, respectively), novel material combinations, ultrathin quantum well layers with thicknesses on the order of a single monolayer (ML), and new device applications.

Quantum well structures may be fabricated from a wide variety of semiconducting materials, including group IV elemental semiconductors and II-VI and III-V compounds. For epitaxial growth of compound semiconductors, the two dominant techniques are organometallic vapour phase epitaxy (OMVPE) and molecular beam epitaxy (MBE). This thesis deals with OMVPE-grown heterostructures consisting of ultrathin InAs or GaSb quantum wells in GaAs. The experiments involved both the

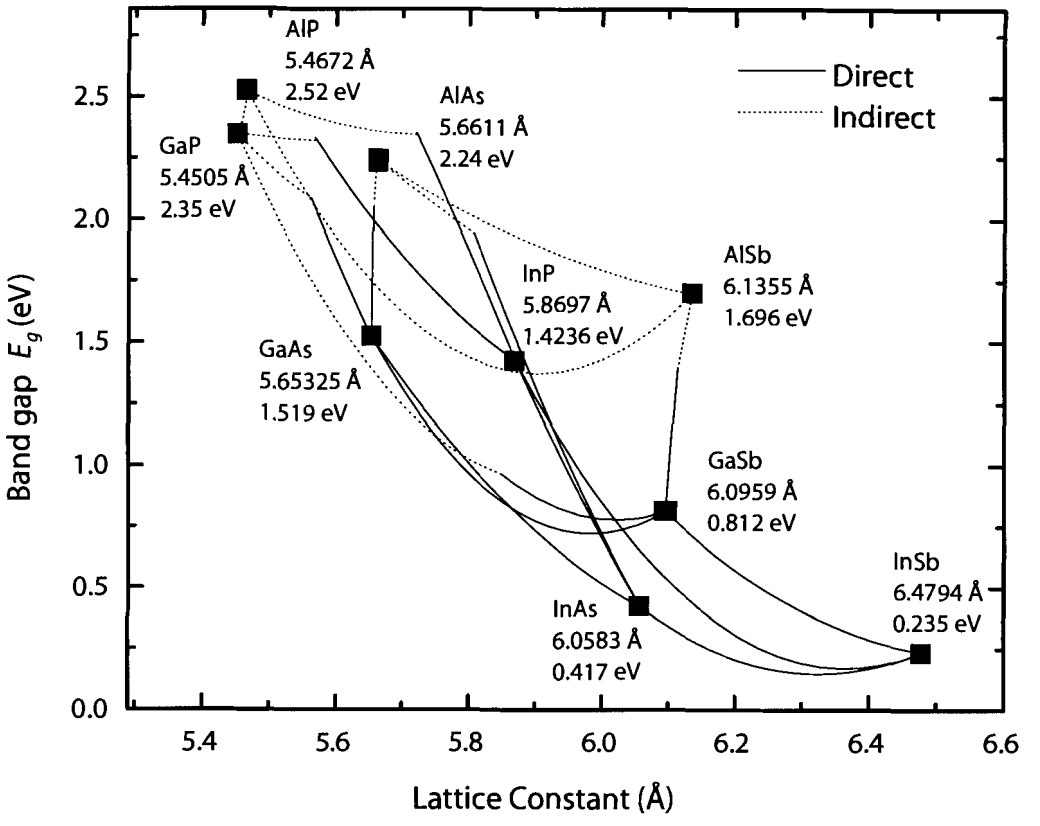

Figure 1.1: Energy gap vs. lattice constant for common binary III-V compounds and their alloys at $T = 0$ K. Data are from Ref. [2].

growth and the characterization of structural and optical properties of these heterostructures. Fig. 1.1 shows two of the fundamental material properties, the band gap and lattice constant, for common binary III-V compounds and their ternary alloys. The band gaps of the binary endmembers and the bowing parameters used to calculate the band gap of each ternary alloy as a function of its composition are taken from the compilation by Vurgaftman *et al.* [2]. The energy gap is categorized according to the region of the conduction band where the minimum occurs; for the materials discussed in this thesis, the conduction band minimum (CBM) and valence band maximum (VBM) are both in the Γ-valley, i.e. at $\mathbf{k} = 0$. A material in which

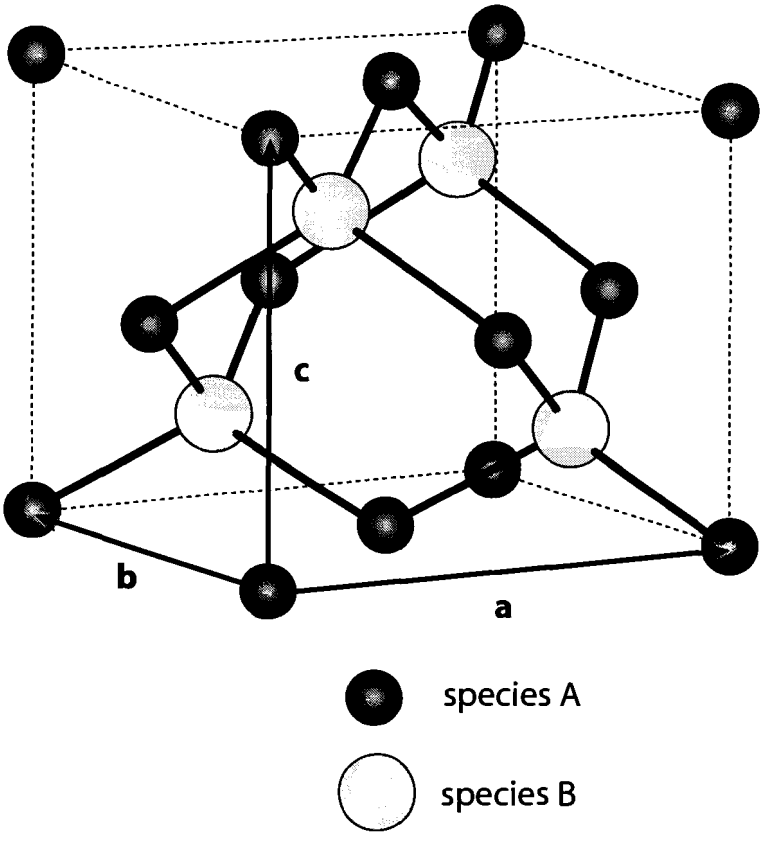

Figure 1.2: Conventional unit cell of the zincblende structure.

the CBM and VBM are at the same value of **k** is referred to as a direct gap semiconductor. In a direct gap semiconductor, photons with an energy equal to the band gap are easily absorbed and emitted, since there is no change in momentum between the CBM and VBM. In an indirect gap semiconductor, on the other hand, the CBM and VBM are at different values of **k**, and optical emission and absorption require the interaction of a phonon to conserve momentum.

GaAs, InAs, and GaSb share the zincblende crystal structure illustrated in Fig. 1.2. In this structure, each of the two atomic species occupies a face-centred cubic (FCC) sublattice within the crystal. The vectors **a**, **b**, and **c** define the conventional unit cell; these vectors are mutually perpendicular and have the same length, which is the lattice constant, a. In units of a, the atomic coordinates within the unit cell of

species A are (0,0,0); $(0,\frac{1}{2},\frac{1}{2})$; $(\frac{1}{2},0,\frac{1}{2})$; and $(\frac{1}{2},\frac{1}{2},0)$, while those of species B are $(\frac{1}{4},\frac{1}{4},\frac{1}{4})$; $(\frac{1}{4},\frac{3}{4},\frac{3}{4})$; $(\frac{3}{4},\frac{1}{4},\frac{3}{4})$; and $(\frac{3}{4},\frac{3}{4},\frac{1}{4})$.

The lattice constant is a crucial parameter, as it must be sufficiently similar for the constituent materials, if a heterostructure is to be successfully grown. A lattice matched heterostructure is composed of materials having the same lattice constant. A strained-layer structure, on the other hand, is composed of materials whose bulk lattice constants differ. If the layer thickness is below a certain critical thickness, an epitaxially grown layer can accommodate strain elastically, adopting the lattice constant of the substrate in the lateral directions, while its lattice constant in the perpendicular direction changes according to the particular elasticity properties of the material. For highly strained epilayers, it becomes energetically favourable for the material to form three-dimensional islands on the surface, if deposition is continued once the critical thickness is reached. This is referred to as the Stranski-Krastanov growth mode. For InAs and GaSb grown on GaAs, the bulk lattice constants of the substrate and epilayer differ by 7.2% and 7.8%, respectively, and the critical thickness is on the order of a single monolayer [3]. Quantum wells of these materials are thus limited to the ultrathin quantum well regime.

A semiconductor heterostructure can be described in terms of the elementary quantum mechanical square potential well, using the envelope function approximation (EFA). This approximation extends the concept of the band structure of a perfect semiconductor crystal to a crystal perturbed by a spatially varying potential. In the EFA, the rapidly varying crystal potential is no longer explicitly considered, and the dynamics of the crystal is represented by electrons and holes with effective masses, which account for the effects of the crystal lattice. The wavefunction of an electron or hole consists of the product of a function with the periodicity of the lattice, and an envelope function. The envelope functions obey an equation which is similar in form to the Schrödinger equation, which allows the use of the solutions similar to those of the elementary square well problem to determine the energy levels and envelope functions [4, 5]. The confinement potentials for electrons and holes are given by the difference in the relative positions of the respective band edge energies at the interfaces. Interfaces are classified according to the band alignment, as shown in Fig. 1.3. At a type-I interface, the conduction band edge is lower and the valence band edge is higher in

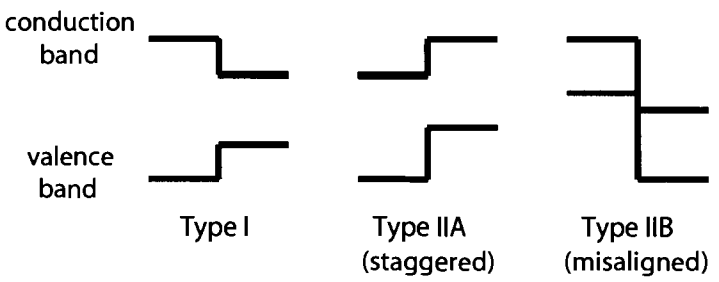

Figure 1.3: Schematic representation of the different types of band lineup.

the lower band gap material; in type-I quantum wells, such as those formed from InAs and GaAs, electrons and holes are both confined in the lower band gap material. At a type-IIA (staggered band lineup) interface, both the conduction band edge and the valence band edge are higher in energy in one material than in the other. Only one type of carrier is confined in a type-IIA quantum well; for example, the holes are confined in GaSb quantum wells while the electrons are localized in the GaAs barriers [6]. Misaligned band lineup or type-IIB interfaces are those in which the valence band edge of one material lies above the conduction band edge of the other material. There also exist occasional references in the literature to type-III heterostructures, formed by a semiconductor and a zero-gap semiconductor [4].

The remaining chapters of the thesis are organized as follows: Chapter 2 introduces the experimental methods that were used to grow and characterize the samples. For each experimental technique, the apparatus and procedures are described, and the theory necessary to interpret the data is summarized. Chapter 3 deals with surface studies of GaAs exposed to Sb; this topic is of importance in understanding the formation of the GaSb/GaAs interface. The chapter begins with a review of the known surface reconstructions of the GaAs (001) surface and their optical anisotropy. A number of previous studies of Sb on the GaAs (001) surface are also reviewed. The chapter concludes by discussing experimental results obtained by *in situ* monitoring, using reflectance-difference spectroscopy, of the GaAs surface exposed to trimethylantimony (TMSb). Chapter 4 deals with the interface quality of GaSb/GaAs and InAs/GaAs multiple quantum well (MQW) structures. The abruptness of the interfaces in these material systems is particularly affected by the surface segregation

of Sb and In, respectively. For each material system, a brief review of previously published work is included. The results of structural studies using x-ray diffraction and transmission electron microscopy are then presented. Chapter 5 discusses the electronic and optical properties of GaSb/GaAs and InAs/GaAs MQW structures. The chapter begins with a review of the relevant literature and continues with a discussion of the EFA and calculations to predict the transition energy at which optical emission occurs. The results of low-temperature photoluminescence measurements are then compared with the theoretical calculations. Finally, important conclusions drawn from this work are summarized in Chapter 6.

Chapter 2

Experimental methods

This chapter discusses the experimental techniques and instruments that were used to grow and characterize the MQW heterostructures, which are the subject of this thesis. For each experimental technique, an overview of the method is given, and the details of the apparatus are described. In the case of reflectance-difference spectroscopy (RDS) and x-ray diffraction (XRD), the theory required to interpret the data is discussed, and derivations of the principal formulæ are outlined. A number of results from the literature are summarized, where they are relevant to the interpretation of the data from a particular type of experiment.

2.1 Organometallic vapour phase epitaxy

OMVPE is a crystal growth technique used to deposit epitaxial films of compound semiconductors onto single-crystal substrates. The epitaxial film is formed from precursor compounds, which include organometallic compounds in the vapour phase, and may also include hydrides (supplied as gases) and halogen-containing compounds. The precursors are carried in an inert carrier gas stream, and arrive at the crystal surface by diffusion through a boundary layer of gas above the surface. The precursors decompose at the heated surface, and the metal atoms are incorporated into the epitaxially growing film.

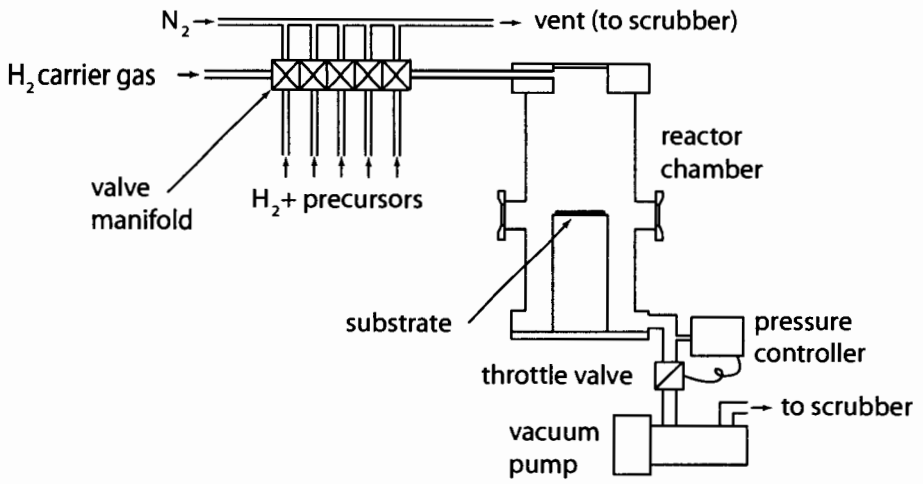

Figure 2.1: Schematic diagram of the OMVPE system

2.1.1 Details of the OMVPE system

The samples studied in this work were grown in a OMVPE system built by Thomas Swan (Cambridge, UK) in 1993. The reactor chamber is a stainless steel design with vertical gas flow. A schematic diagram of the apparatus is shown in Fig. 2.1. Organometallic precursors are used for the supply of both group III (Ga,In,Al) and group V (P,As,Sb) elements, as well as Zn and C, which are used as dopants. The system also includes input channels for compressed-gas sources, which are dopant precursors for S, C and Si, diluted in hydrogen. The carrier gas is hydrogen. As with all modern OMVPE systems, a "vent/run" switching scheme is employed, in which the precursor flows are normally kept constant. A valve manifold, located close to the reactor, switches the precursors between the reactor (or run line) and a vent line which bypasses the reactor, exhausting the precursors directly to the scrubber for toxic component removal. This procedure allows fast switching between different precursor flows into the reactor, which is crucial in the growth of abrupt heterointerfaces. All switching during a growth run is computer-controlled in order to ensure precise timing of the growth steps.

In order to ensure reproducibility of the growth conditions, it is necessary to control

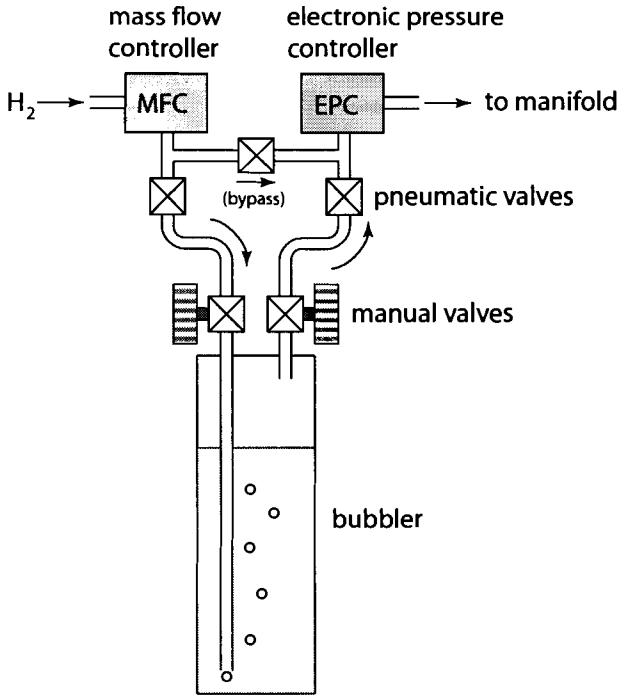

Figure 2.2: Schematic diagram of a bubbler designed for organometallic compounds, with flow and pressure control systems.

the temperature of the substrate, the ambient pressure in the reactor chamber, the carrier gas flow and the molar rate at which the precursors are introduced into the reactor chamber. The systems needed to ensure precise control over these parameters account for the considerable complexity of the apparatus.

2.1.2 Organometallic precursors

The organometallic precursors are stored in stainless steel bubblers, as shown in Fig. 2.2. With the exception of trimethylindium (TMIn) and CBr_4,which are solid, they are liquid at the storage temperature (usually between -15 °C and 18 °C.) The rate of supply is controlled by a mass flow controller (MFC), which sets the mass flow rate of hydrogen into the bubbler. The hydrogen rises through the liquid as bubbles, and emerges saturated with the organometallic compound. The ratio of organometal-

Table 2.1: Properties of organometallic precursors. MP: melting point; BP: boiling point.

Abbreviation	Formula	MP (°C)	BP (°C)	a	b (K)
TEGa	$C_6H_{15}Ga$	-82.5	143	9.172	2532
TBAs	$C_4H_{11}As$	-1	65	7.243	1509
TMSb	C_3H_9Sb	-87.6	80.6	7.707	1697
TMIn	C_3H_9In	88	135.8	10.520	3014

lic molecules to those of hydrogen is then equal to the ratio of their partial pressures. The molar supply rate of the precursor, f_p, is the product of this ratio and the molar rate of hydrogen flow:

$$f_p = n_0 F_{sccm} \frac{P_V(T)}{P_B - P_V(T)} \tag{2.1}$$

where F_{sccm} is the hydrogen flow, expressed as a volume flow (cm^{-3}/min) at standard temperature and pressure (STP), n_0 is the constant expressing the number of moles per cm^{-3} in an ideal gas at STP, and $P_V(T)$ and P_B are the precursor vapour pressure and the total pressure in the bubbler, respectively. The dependence of the vapour pressure on the temperature is given by the empirical relation

$$P_V(T) = 10^{a-b/T} \tag{2.2}$$

where a and b are constants which are characteristic of a particular compound. The temperature is kept constant by placing the bubbler in a temperature-controlled bath of ethylene glycol/water solution, and the bubbler pressure is controlled by an electronic pressure controller. The properties of the compounds used as precursors for the samples studied in this thesis are shown in Table 2.1.

2.1.3 Reactor design

A more detailed view of the OMVPE reactor is shown in Fig. 2.3. The group III and group V precursors enter the reactor through separate lines, to minimize any reactions between these precursors in the gas phase. They are mixed by a perforated mixing ring, and the gas mixture travels downwards toward the substrate surface. The

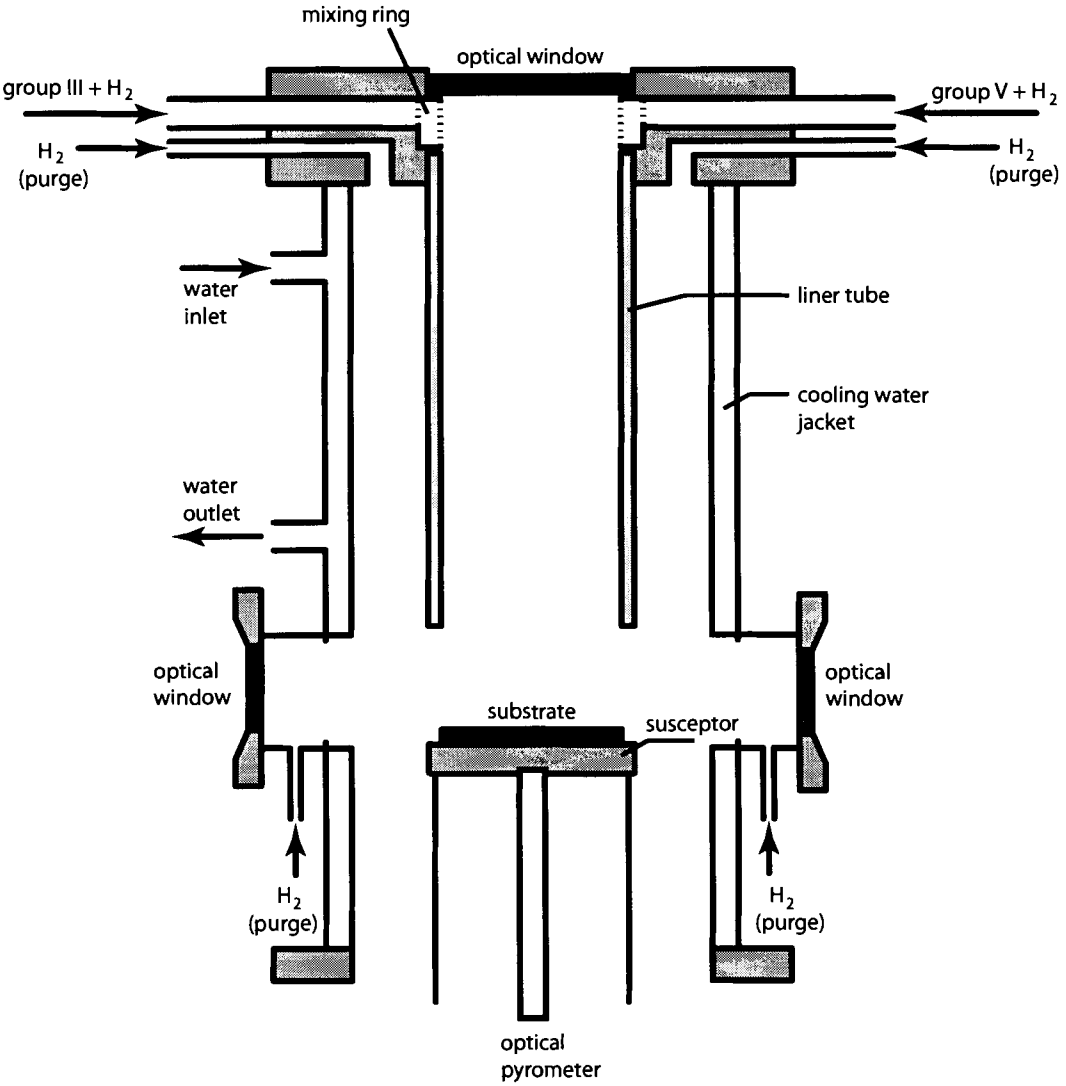

Figure 2.3: Diagram of the OMVPE reactor chamber (based on a figure by Wiersma [7]).

hydrodynamics of gas flow in the OMVPE reactor is complex. The ideal situation for achieving high quality, uniform layers with abrupt interfaces is a steady laminar flow, but this is difficult to achieve in practice. Recirculating gas currents can appear above the sample due to thermal convection. Reactor flow dynamics have been investigated using computational methods [8] and gas flow visualization [9]. These studies indicated that a rotating susceptor can improve the flow conditions. While the OMVPE reactor used in this work has the capability for susceptor rotation, rotation was not employed because of the difficulties it introduces for *in situ* monitoring. A relatively low reactor pressure of 50 Torr was employed to minimize recirculating currents. Other reactor design considerations include avoiding abrupt changes in diameter, and obstacles in the path of the gas flow. The reactor used in this work employs a cylindrical inner liner tube to provide a constant cross-section for the gas flow.

Heating of the substrate to the growth temperature is accomplished by an electrical resistance heater. The substrate is placed on a graphite susceptor which is heated from below. The thermal mass of the susceptor helps to stabilize the temperature. In order to keep the temperature steady, the heater output is adjusted by feedback from an optical pyrometer, which measures the temperature of the underside of the susceptor. Achieving accurate temperature control of the substrate surface is, however, a difficult issue in OMVPE, due to the potential variability of the heat transfer rates between the susceptor, the substrate, and the surrounding environment. The practice employed in this study is to rely on calibration of the optical pyrometer reading to a measurement of the surface temperature, using a thermocouple. This calibration is performed as part of regular reactor cleaning and maintenance procedures. Nevertheless, all growth temperatures that are reported should be understood to be subject to some variability. Routine adjustments to the pyrometer calibration are typically less than 5 °C, but adjustments as great as 10–20 °C are occasionally necessary after susceptor cleaning.

2.1.4 Decomposition of the precursors

Near the substrate surface, the gas flow is horizontal, with the flow velocity approaching zero at the surface itself. The precursor molecules therefore arrive at the surface by

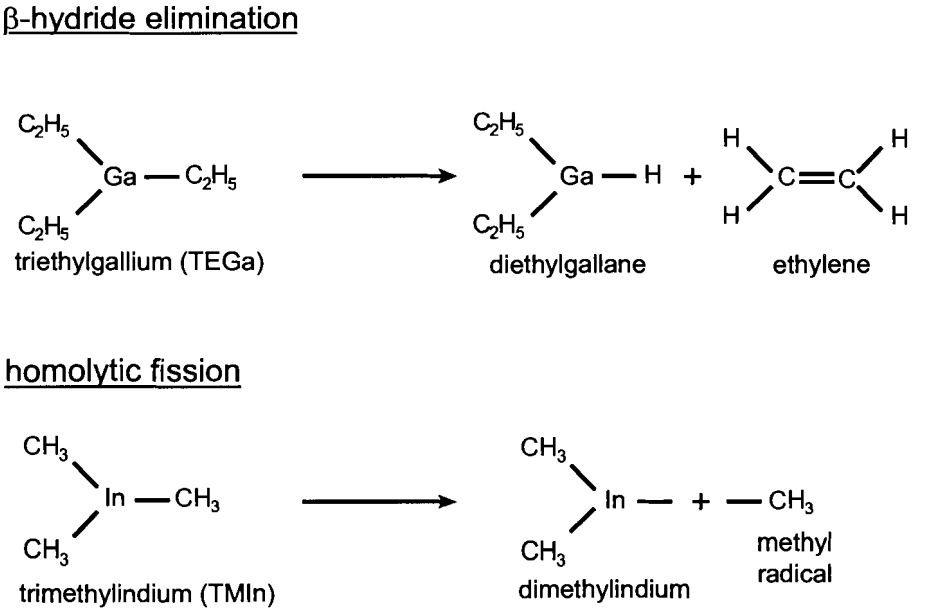

Figure 2.4: Examples of the two decomposition reactions: β-hydride elimination and homolytic fission.

diffusion through a stagnant boundary layer. As the molecules are heated to the temperature of the substrate, they undergo pyrolysis, decomposing into their constituent metal atoms and organic radicals. The different types of pyrolysis reactions which can occur are discussed in detail by Stringfellow [10]. Two of these reactions are shown in the diagrams in Fig. 2.4. The compound triethylgallium (TEGa) decomposes by a reaction known as β-hydride elimination, in which each ethyl group leaves behind a hydrogen atom bonded to the Ga, forming ethylene. The trimethyl compounds, on the other hand, dissociate by homolytic fission, in which each methyl radical in turn simply breaks its bond with the metal atom. The exact decomposition mechanism of tertiarybutylarsine (TBAs) is uncertain; a number of candidate reaction sequences involving β-hydride elimination have been proposed [10].

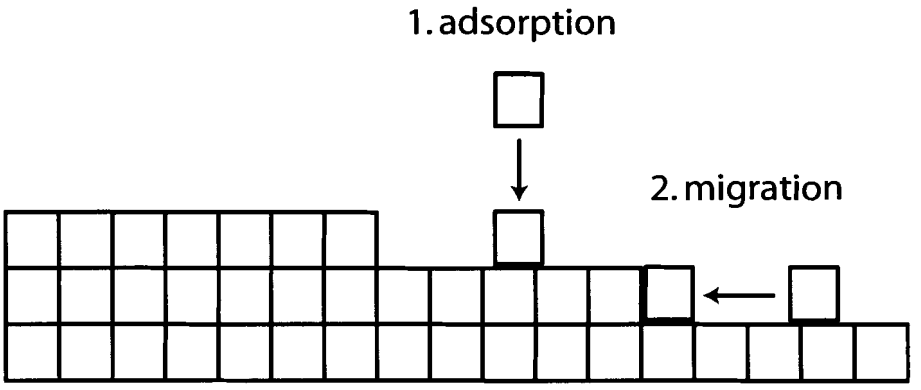

Figure 2.5: Illustration of step flow growth: atoms are adsorbed on the surface, then migrate to step edges.

2.1.5 Epitaxial growth

The metal atoms produced in the boundary layer by the pyrolysis reactions are subsequently adsorbed onto the surface of the growing crystal. The adsorbed atoms are mobile and can migrate across the sample surface until they are incorporated into the crystal structure. In practice, no macroscopic crystal surface is atomically flat over its entire area; there are always atomic terraces bounded by step edges. Under typical OMVPE conditions, adsorbed atoms are preferentially incorporated at step edges, as shown in Fig. 2.5. A step edge will therefore propagate across the surface until it merges with another step or reaches the edge of the sample — this is referred to as step flow growth.

Epitaxial growth is fundamentally driven by thermodynamics at the solid/vapour interface. The system strives to reduce the difference in chemical potentials

$$\Delta\mu = \mu_v - \mu_s \tag{2.3}$$

where μ_v and μ_s are the chemical potentials of the vapour and solid, respectively [10]. However, other factors are also involved, chiefly the kinetics of surface diffusion and surface reactions, and the hydrodynamics of mass transport to the growing surface. Studies of the growth rate as a function of growth temperature have revealed three growth regimes [10]: at low temperatures, the growth rate is limited by kinetics and

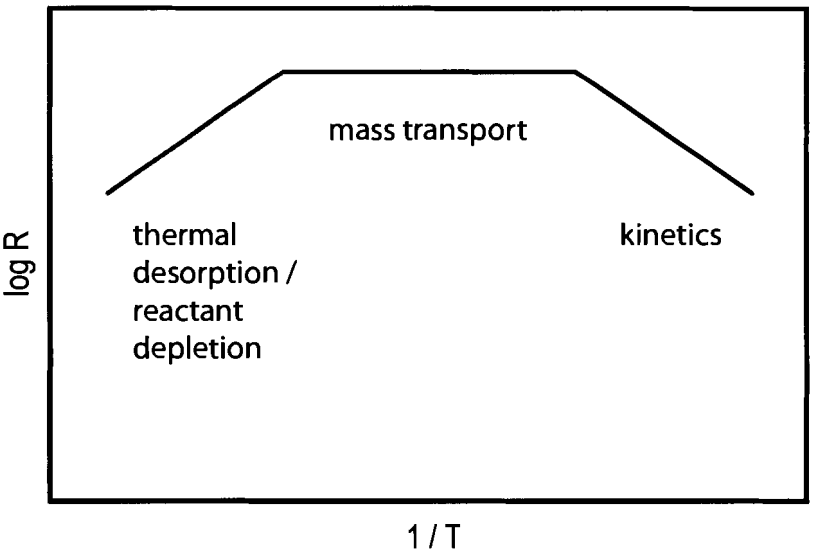

Figure 2.6: Schematic plot of the growth rate as a function of inverse temperature, showing three growth regimes and the factors limiting the growth rate in each case.

increases with temperature; the decomposition of the group III precursor is thought to be the rate limiting step. At higher temperatures, roughly 550 °C–750 °C, mass transport (diffusion of the reactants through the boundary layer) is the limiting factor. In this growth regime, which is the one almost always used for OMVPE in practice, the growth rate is only weakly temperature-dependent and depends nearly linearly on the group III flow rate. At higher temperatures, the growth rate decreases with increased temperature, which may be due either to thermal desorption of the group III element from the surface or to depletion of the reactants from the gas stream. The three growth regimes are shown schematically in Fig. 2.6. Since OMVPE is typically performed with an oversupply of the group V precursor or precursors, the group III flow is the one which controls the growth rate. The oversupply of group V is necessary to prevent the desorption of the more volatile group V element(s) from the surface, and it also enhances step flow growth. For many common compounds, (e.g. GaAs), the ratio of the molar supply rate of group V to that of group III (the "V–III ratio") can be chosen in a wide range, whereas for certain compounds, high quality epilayers

can only be grown in a limited range. For example, successful growth of antimonide compounds requires a V–III ratio close to unity [10].

2.2 Reflectance-difference spectroscopy

In order to effectively study processes occurring during crystal growth, *in situ* characterization of the semiconductor surface is desirable. Due to the relatively high pressure of the OMVPE environment, electron diffraction techniques cannot be applied. Instead, an optical characterization method is required. Optical data are typically dominated by the contribution from the bulk crystal, which overwhelms any signal arising from the surface. RDS overcomes this difficulty by measuring the difference in the reflectance of light polarized along two orthogonal crystal axes. Since the bulk reflectance is isotropic for cubic crystals, the RDS signal is primarily sensitive to the lower-symmetry crystal surface. The apparatus used in this work is a custom-built system based on the setup described by Aspnes [11].

2.2.1 The RDS apparatus

A diagram of the RDS apparatus is shown in Fig. 2.7. A xenon arc lamp is used as a white light source. Spherical and planar mirrors are used to focus and direct the beam. The beam is first linearly polarized by using a Rochon prism. The polarized beam, which has equal components of polarization along the [110] and [$\bar{1}$10] axes, reflects from the sample and is then directed through a photoelastic modulator (PEM) oriented parallel to the direction of polarization. The PEM consists of an optical wave plate, the retardation of which is periodically modulated by applying piezoelectric strain. The rate of the modulation is 50 kHz, which avoids coupling of the measurement to any mechanical vibration modes. For spectroscopic measurements, the PEM control circuitry is adjusted for each wavelength, λ, so that the retardation oscillates between $\lambda/2$ and $-\lambda/2$. The beam then passes through an analyzer consisting of a second Rochon prism with its axis of polarization at 45 ° to the original polarization direction. The beam is dispersed through a grating spectrometer and detected by a photomultiplier tube. A lock-in amplifier, with its reference frequency

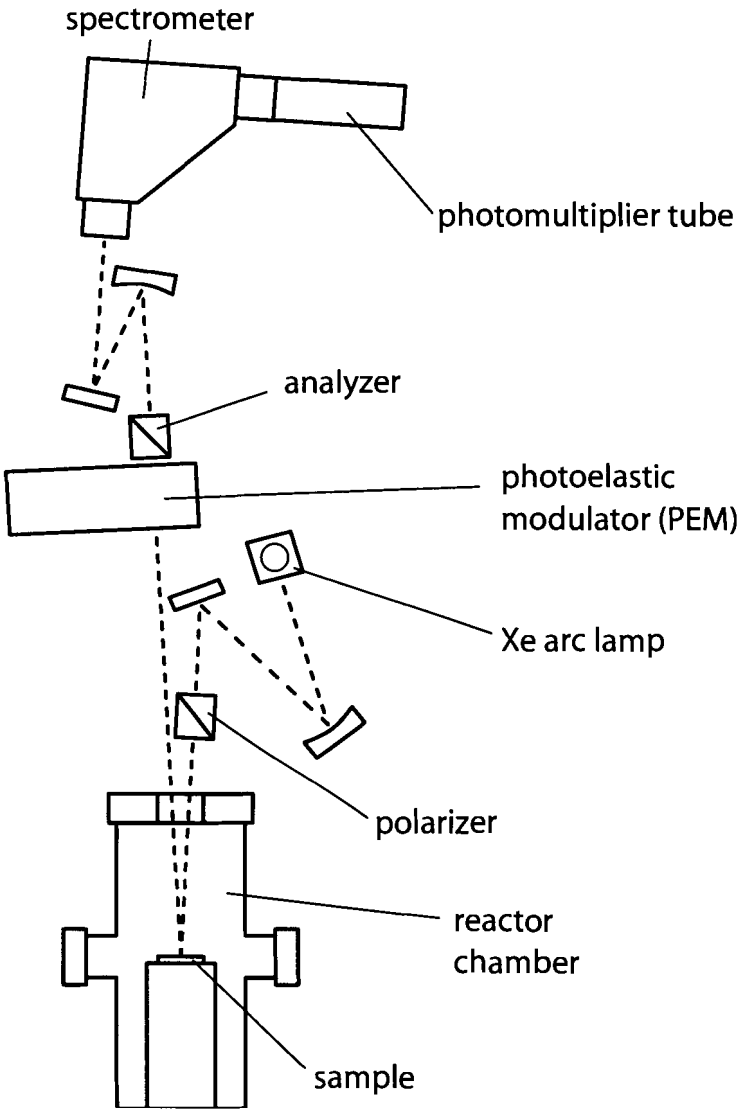

Figure 2.7: Diagram of the RDS apparatus

determined by the PEM modulation, extracts the component of the signal desired. The signal includes harmonics at integer multiples of the modulation frequency, ω; as shown in the derivation in section 2.2.2, the 2ω component is directly proportional to the real part of the reflectance anisotropy, whereas the ω component depends on both the real and imaginary parts. In the present work, only the 2ω component of the reflectance-difference (RD) signal was measured.

RD spectra are typically collected in the range 1.5–5 eV, which requires roughly two minutes. In order to obtain spectroscopic information about processes occurring on a shorter time scale, time-resolved RDS was employed. Time-resolved RDS runs involve a periodically repeated OMVPE sequence, with the RD transient collected as a function of time, for a single wavelength, during each period. The data collection is synchronized to a reference time point in the OMVPE sequence. The spectra can then be constructed from the RD transients for each wavelength point. For this type of experiment to provide useful data, the periodic sequence must produce identical surface conditions each time the sequence is repeated. This was verified by monitoring a single wavelength during several repetitions of the OMVPE sequence, before collecting the time-resolved RDS data.

2.2.2 Optical response of the RDS system

In this work, the reflectance-difference signal is defined as the real part of the complex reflectance anisotropy

$$\frac{\Delta r}{r} \equiv 2Re\left[\frac{r_{\bar{1}10} - r_{110}}{r_{\bar{1}10} + r_{110}}\right] \tag{2.4}$$

where r_{110} and $r_{\bar{1}10}$ are the complex reflectances of light polarized along the [110] and [$\bar{1}$10] axes, respectively. The analysis which follows, however, involves the measured intensities, so it is helpful to relate the above quantity to the reflectance intensity anisotropy

$$\frac{\Delta R}{R} \equiv 2\frac{|r_{\bar{1}10}|^2 - |r_{110}|^2}{|r_{\bar{1}10}|^2 + |r_{110}|^2} \tag{2.5}$$

By expanding these two expressions in terms of r_{110}, $r_{\bar{1}10}$, and their respective complex conjugates, and using the fact that $(\Delta r)^2 \ll r^2$ for the [001] surfaces of interest, one

obtains

$$\frac{\Delta R}{R} = 2\frac{\Delta r}{r} \tag{2.6}$$

In order to analyze the optical response of the RD apparatus, it is convenient to make use of the Jones Matrix Calculus [12]. The polarized light is represented by a Jones vector, denoted here as $\boldsymbol{E_j}$, and each optical element is represented by a 2×2 Jones matrix. The coordinate system is chosen so that the components of the Jones vectors correspond to the [110] and [$\bar{1}$10] crystal axes. The initial polarized beam has equal components along each of these directions, and is thus given by

$$\boldsymbol{E_0} = \varepsilon_0 \begin{pmatrix} 1 \\ 1 \end{pmatrix} \tag{2.7}$$

where ε_0 is proportional to the amplitude of the electric field. Applying the Jones matrix for reflection, one obtains the Jones vector for the beam reflected from the sample:

$$\boldsymbol{E_1} = \begin{pmatrix} r_{110} & 0 \\ 0 & r_{\bar{1}10} \end{pmatrix} \varepsilon_0 \begin{pmatrix} 1 \\ 1 \end{pmatrix} = \varepsilon_0 \begin{pmatrix} r_{110} \\ r_{\bar{1}10} \end{pmatrix} \tag{2.8}$$

The Jones matrix for a retarder with phase shift ϕ is given by [12]

$$\mathsf{M} = \begin{pmatrix} e^{i\phi/2} & 0 \\ 0 & e^{-i\phi/2} \end{pmatrix} \tag{2.9}$$

In the case of the PEM, the phase shift is modulated so that $\phi(t) = \pi \sin \omega t$. The PEM is at 45° to the crystal axes, so the Jones matrix for the PEM is $\mathsf{J}^T\mathsf{M}\,\mathsf{J}$ where J is the rotation matrix

$$\mathsf{J} = \begin{pmatrix} \cos 45 & \sin 45 \\ -\sin 45 & \cos 45 \end{pmatrix} = \frac{1}{\sqrt{2}} \begin{pmatrix} 1 & 1 \\ -1 & 1 \end{pmatrix} \tag{2.10}$$

and the beam emerging from the PEM is given by

$$\boldsymbol{E_2} = \mathsf{J}^T\mathsf{M}\,\mathsf{J}\boldsymbol{E_1} = \varepsilon_0 \begin{pmatrix} r_{110} \cos\frac{\phi(t)}{2} + i r_{\bar{1}10} \sin\frac{\phi(t)}{2} \\ r_{\bar{1}10} \cos\frac{\phi(t)}{2} + i r_{110} \sin\frac{\phi(t)}{2} \end{pmatrix} \tag{2.11}$$

The analyzer is a polarizing prism oriented along [110]; applying its Jones matrix, one obtains

$$\boldsymbol{E_3} = \begin{pmatrix} 1 & 0 \\ 0 & 0 \end{pmatrix} \boldsymbol{E_2} = \varepsilon_0 \begin{pmatrix} r_{110} \cos\frac{\phi(t)}{2} + i r_{\bar{1}10} \sin\frac{\phi(t)}{2} \\ 0 \end{pmatrix} \tag{2.12}$$

The photomultiplier current is proportional to the intensity $|\boldsymbol{E_3}|^2$;

$$\begin{aligned} |\boldsymbol{E_3}|^2 = \varepsilon_0^2 \Bigg(& |r_{110}|^2 \cos^2 \frac{\phi(t)}{2} + |r_{\bar{1}10}|^2 \sin^2 \frac{\phi(t)}{2} \\ & + i \left(r_{\bar{1}10} r_{110}^* - r_{110} r_{\bar{1}10}^* \right) \cos \frac{\phi(t)}{2} \sin \frac{\phi(t)}{2} \Bigg) \end{aligned} \tag{2.13}$$

Using the appropriate half-angle formulæ, this simplifies to

$$\begin{aligned} |\boldsymbol{E_3}|^2 = \frac{\varepsilon_0^2}{2} \Bigg(& |r_{110}|^2 + |r_{\bar{1}10}|^2 + \left(|r_{110}|^2 - |r_{\bar{1}10}|^2 \right) \cos \phi(t) \\ & + \left(r_{\bar{1}10} r_{110}^* - r_{110} r_{\bar{1}10}^* \right) \sin \phi(t) \Bigg) \end{aligned} \tag{2.14}$$

The trigonometric functions can be expanded in Bessel function series:

$$\begin{aligned} \cos \phi(t) &= J_0(\pi) + 2 \sum_{m=1}^{\infty} J_{2m}(\pi) \cos(2m\omega t) \\ \sin \phi(t) &= 2 \sum_{m=1}^{\infty} J_{2m+1}(\pi) \sin \left((2m+1)\, \omega t \right) \end{aligned} \tag{2.15}$$

The RDS system measures the 2ω term — the lock-in amplifier is set to use 100 kHz (twice the modulation frequency) as its reference frequency. The photomultiplier current may be expressed as $I(t) = I_0 + \Delta I(\omega t) + \Delta I(2\omega t) + \cdots$. From the above expression for $|\boldsymbol{E_3}|^2$, the relation between the 2ω component of the time-varying current, and the real part of the reflectance anisotropy is

$$\begin{aligned} \frac{\Delta I(2\omega t)}{I_0} &= 2 J_2(\pi) \left(\frac{|r_{110}|^2 - |r_{\bar{1}10}|^2}{|r_{110}|^2 + |r_{\bar{1}10}|^2} \right) \cos 2\omega t \\ &= 2 J_2(\pi) \frac{\Delta r}{r} \cos 2\omega t \end{aligned} \tag{2.16}$$

In practice, the photomultiplier tube current must first be amplified and converted into a voltage before being measured by the lock-in amplifier. A simple home-built preamplifier is used for this purpose. The preamplifier does not have a flat frequency response, so its attenuation at 100 kHz must be taken into account to calculate $\Delta r/r$ from the measured AC and DC voltages. The attenuation was estimated by comparing the signal from the home-built preamplifier to the signal obtained with an EG&G

preamplifier, the bandwidth of which is well above 100 kHz according to the manufacturer's specifications. The home-built preamplifier was found to attenuate by a factor of $\sim$ 3.5 at 100 kHz, relative to the DC response. In normal use, the attenuating preamplifier is in fact beneficial since it filters out higher-frequency noise which was not effectively filtered when using the lock-in amplifier with the EG&G preamplifier. The RD signal, $\Delta r/r$, is thus related to the ratio of the AC and DC components of the voltage signal by

$$\frac{\Delta r}{r} \approx 3.5 \frac{\sqrt{2}}{2J_2(\pi)} \frac{V_{AC}}{V_{DC}} \approx 5 \frac{V_{AC}}{V_{DC}} \tag{2.17}$$

with the factor $\sqrt{2}$ accounting for the fact that V_{AC}, as measured by the lock-in amplifier, is the root-mean-square (RMS) value (the approximate value of $J_2(\pi)$ is 0.4854).

2.3 High resolution x-ray diffraction

High resolution XRD is the principal technique used in this work to determine the structural properties of the samples investigated. The technique consists in measuring the diffracted intensity in a small angular range about one of the Bragg diffraction peaks of the substrate crystal. The so-called rocking curves obtained in this way contain information about the thicknesses and strains of the epilayers, and provide an indication of the degree of layer perfection. Even complicated heterostructures may be analyzed, with the help of computer simulations of the rocking curves.

2.3.1 Generation of x-rays and beam conditioning

In the discussion of the theory of diffraction from crystals, we will assume that the incident field is a plane wave. In practice, however, the laboratory x-ray source generates a range of wavelengths and has a finite angular dispersion. The x-ray generator consists of a cathode ray tube with a metal target at the anode end. Electrons accelerate through the applied potential, then strike the target. The rapid deceleration of the electrons produces bremsstrahlung radiation in the x-ray region. Part of this radiation is absorbed by the target, through excitation of atoms from their ground

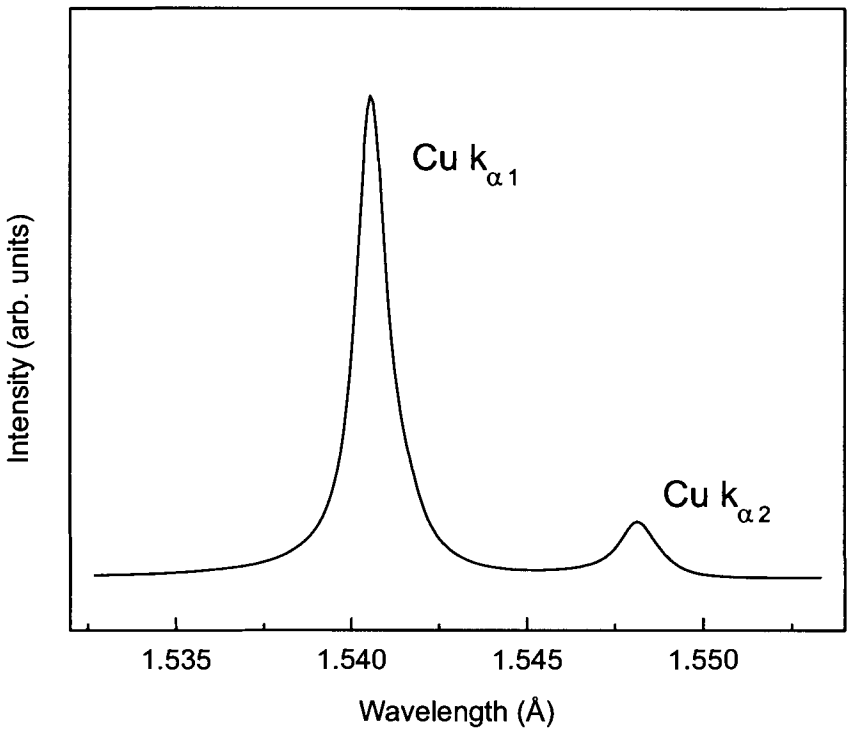

Figure 2.8: X-ray source spectrum in the region of the Cu $K_{\alpha 1}$ emission line, which is used for the diffraction experiments.

state into higher-lying levels. Transitions from these excited states result in sharp x-ray emission lines, which are superimposed on the broad bremsstrahlung background (see Fig. 2.8).

In order to obtain high quality rocking curves, it is necessary to use a beam conditioner to collimate the beam and make it monochromatic. The beam conditioner itself consists of one or more diffracting crystals, together with angular-limiting apertures. The measured rocking curve is in fact the correlation function of the rocking curves of the beam conditioner crystals and the specimen [13]. However, if the rocking curve widths of the beam conditioner crystals are much narrower than those of the specimen, the measured curve approaches the theoretical plane-wave rocking curve of the specimen. The availability of large, nearly defect-free crystals of silicon from the

electronics industry has allowed the design of beam conditioners with extremely narrow rocking curve widths, so that the above condition can be met for any specimens of practical interest.

2.3.2 Details of the x-ray diffractometer

The apparatus used for high-resolution XRD is a Bede D3 triple-axis diffractometer. The instrument is illustrated schematically in Fig. 2.9. The x-ray source uses a copper target and is normally operated at a voltage of 40 kV and a current of 30 mA. The beam conditioner consists of two silicon channel cut crystals, which are shown in detail in the inset. The beam conditioner crystals are positioned in the (220) diffraction condition (the notation for diffracting conditions is discussed in section 2.3.4.) Two settings of the beam conditioner are possible; the symmetrically cut (parallel to the diffracting planes) channels are used to obtain the highest possible resolution, with four reflections in each channel cut crystal. The asymmetrically cut channels are used to obtain higher intensity, with two reflections in each channel cut crystal. For the work reported in this thesis, the high intensity setting was used — this setting produces a higher signal-to-noise ratio with adequate resolution and is usually used unless the higher resolution is needed.

The specimen is mounted to a plate by means of small pieces of wax, which are melted, then allowed to solidify. This avoids placing any external stress on the specimen. The plate attaches magnetically to the sample holder on the diffractometer. In addition to the vertical axis ω, the sample may be rotated about the horizontal axis ϕ in the plane of the sample surface, and displaced perpendicular to the surface (z axis). These adjustments allow the accurate orientation of the specimen in a diffracting condition. Additionally, the specimen can be displaced parallel to its surface (x and y axes), in order to sample different regions of the crystal.

The detector is mounted on an arm, which can be rotated independently of the ω axis. The detector consists of a scintillator crystal, which converts x-ray photons into optical photons, which are then detected by a photomultiplier tube. The detector arm has attachments for placing apertures in front of the detector, and also carries a third channel cut crystal, which can be moved into or out of the path of the x-ray

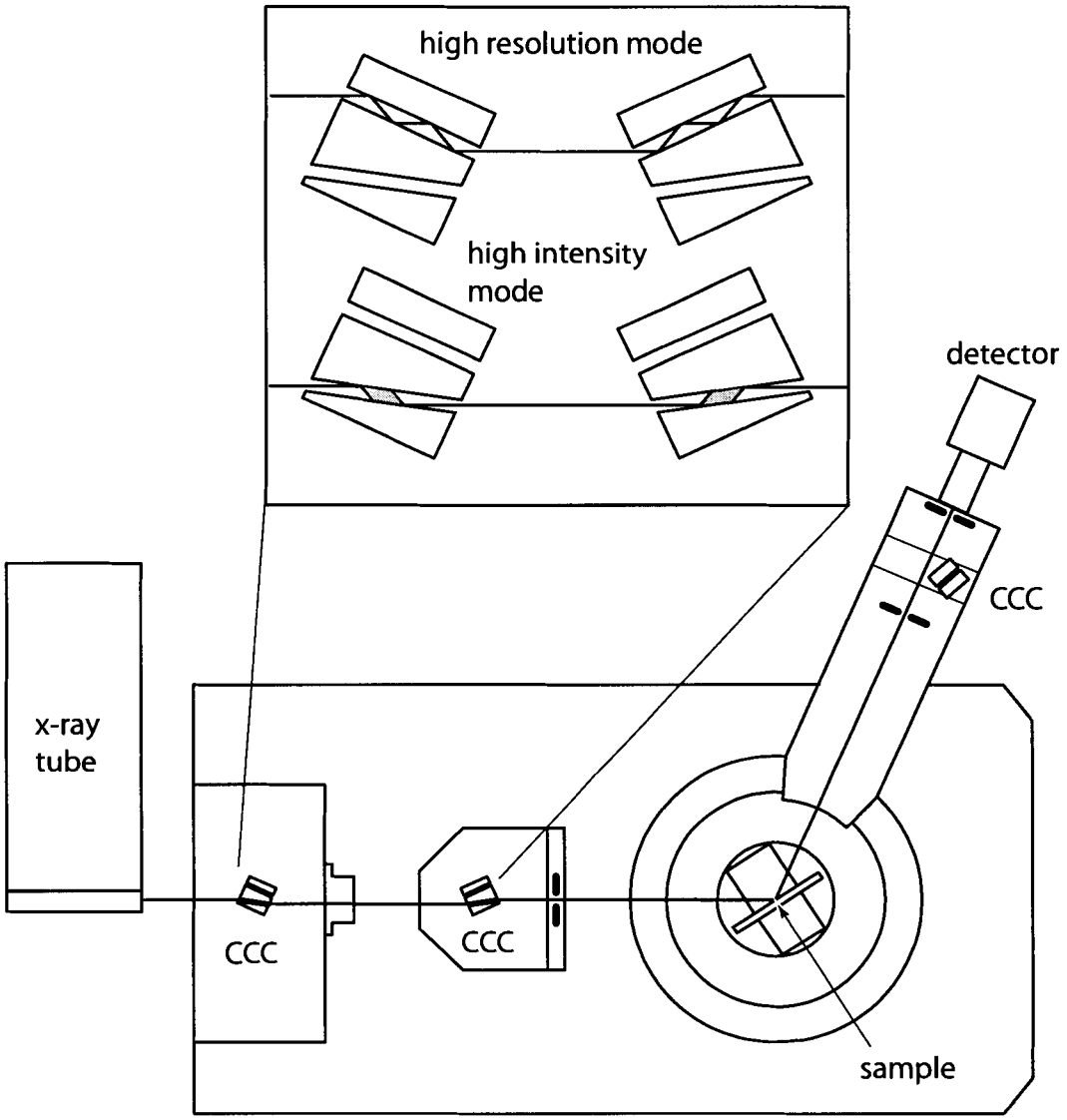

Figure 2.9: Schematic diagram of the high resolution x-ray diffractometer. The inset shows the two possible configurations of the beam conditioner channel cut crystals (CCC).

beam. The analyzer crystal serves to limit the angular acceptance of the detector to a very narrow range, and is primarily used for reciprocal space mapping, which was not employed in this work. For the collection of rocking curve data, the analyzer crystal is moved out of the beam path, so that all of the diffracted intensity is detected, for any given specimen orientation. Apertures are usually placed in front of the detector, even for rocking curve collection, in order to reduce background noise from diffusely scattered x-rays.

2.3.3 Diffraction of x-rays from a crystal

For radiation with a wavelength of the order of the interatomic spacing in crystals, diffraction effects are expected. The response of a crystal to an incident x-ray wave field can be approached on two different levels; the kinematical and dynamical diffraction theories. The kinematical theory assumes that the incident beam is the same throughout the crystal. This is, evidently, a poor assumption for thick specimens of nearly perfect crystals, such as those studied in this work, which diffract x-rays strongly. Nevertheless, the kinematic theory correctly predicts the positions of the diffraction peaks, and allows useful insight into the diffraction phenomenon. The dynamical theory, which treats the transfer of energy and momentum between the incident and diffracted beams in detail, is required to correctly predict the intensity profile of rocking curves. However, since it involves numerical solution of systems of partial differential equations, it is difficult to obtain any physical insight from the dynamical theory. The dynamical diffraction theory is the basis of the computer simulations discussed in Sect. 2.3.5, but its derivation is beyond the scope of this thesis. Instead, the kinematical diffraction theory is outlined. This will allow a discussion of the diffraction geometry of MQW structures.

The simplest description of diffraction from a crystal is Bragg's law. Bragg's law can be derived by assuming that part of the incident wave reflects specularly from successive crystal planes, as shown in Fig. 2.10. It is then evident from the geometry that the reflected waves will be in phase when the path length difference AOB is an integer number of wavelengths, which is the case when

$$n\lambda = 2d\sin\theta \tag{2.18}$$

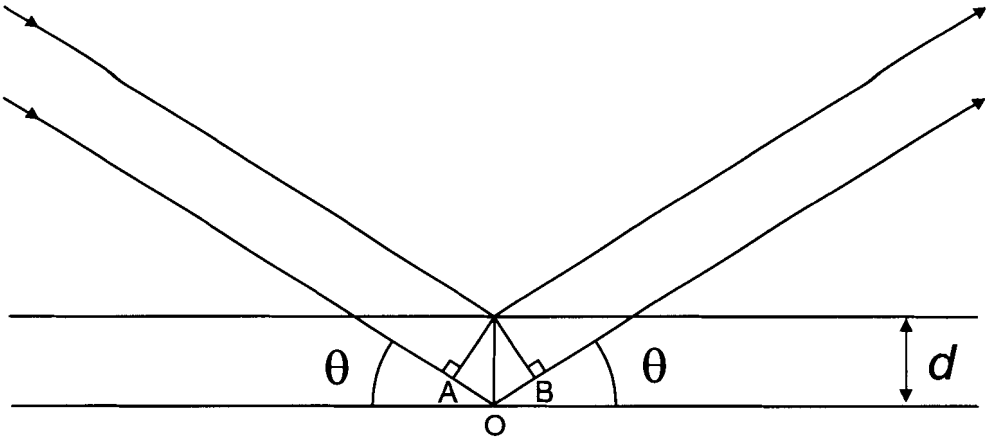

Figure 2.10: Diffraction of x-rays from parallel crystal planes. AOB is the path length difference (after Bowen and Tanner [13]).

where n is an integer, λ is the wavelength, d is the interplanar spacing and θ is the incident, and reflected, angle. However, it is not clear from the derivation of Bragg's Law, why the incident angle should equal the angle of reflection. To show this, one must consider the scattering from individual atoms within the crystal.

The scattering geometry for an incident x-ray beam scattered from two atoms is illustrated in Fig. 2.11. It is not necessary to consider scattering mechanisms in detail here, suffice it to state that the incident beam can be scattered in all directions, with some angular distribution $f(\theta)$. The scattering is elastic, so that $|\mathbf{k_0}| = |\mathbf{k_h}| = 1/\lambda$ (note that this convention, adopted in this section because it is common in crystallography texts [13, 14], is different from the convention which will used for the wave vector in Chap. 5, i.e. $|\mathbf{k}| = 2\pi/\lambda$). The observation point is sufficiently distant that the scattered beams from the two atoms may be considered parallel. The phase difference between the scattered beams is then given by

$$\exp\{-2\pi i(\mathbf{k_h} \cdot \Delta\mathbf{r} - \mathbf{k_0} \cdot \Delta\mathbf{r})\} = \exp\{-2\pi i\mathbf{Q} \cdot \Delta\mathbf{r}\} \tag{2.19}$$

where $\mathbf{Q} = \mathbf{k_h} - \mathbf{k_0}$ and $\Delta\mathbf{r}$ is the separation between the two atoms. Thus, the scattered waves from two atoms in the plane normal to the vector $\mathbf{Q}$ have the same phase. In general, the waves scattered from two atoms are in phase if the dot product $\mathbf{Q} \cdot \Delta\mathbf{r}$ is an integer.

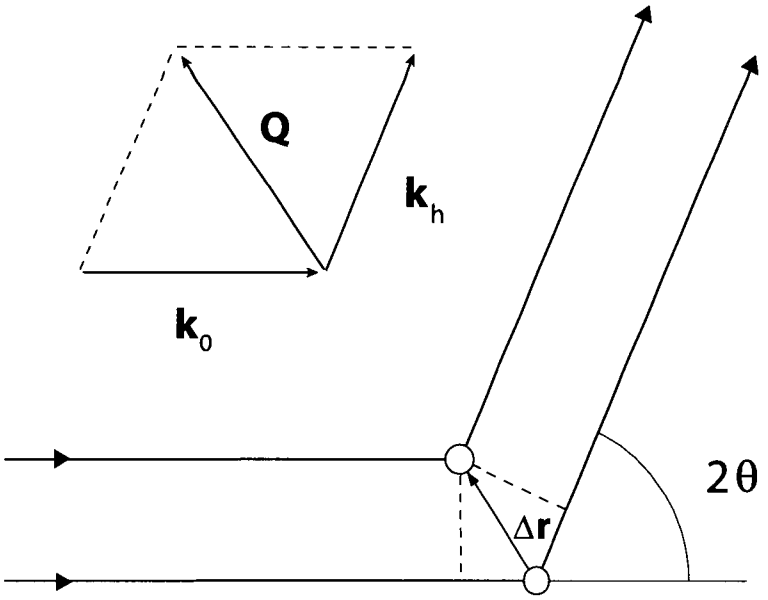

Figure 2.11: Geometry of x-ray scattering from two atoms separated by a vector $\Delta\mathbf{r}$ (after Bowen and Tanner [13]).

The phase difference obtained above is applicable to the x-rays scattered from the atoms making up a crystal. The x-ray beam scattered in a particular direction from a crystal is the sum of the scattered waves from the individual atoms. Clearly, a significant intensity will result only when all such waves are in phase. In other words, if the origin is chosen to correspond to the position of an atom, then the dot product $\mathbf{Q} \cdot \mathbf{r}_j$ must be an integer for any other atom j within the crystal. This can only occur when the arrangement is such that the atoms lie in planes which are normal to the vector $\mathbf{Q}$, and the plane spacing d is such that $|\mathbf{Q}|d$ is an integer. These two conditions are equivalent to Bragg's law (2.18).

2.3.4 The reciprocal space formulation

The concepts of reciprocal space, and the reciprocal lattice, are very helpful in understanding the geometry of diffraction. One can define vectors $\mathbf{a}^*$, $\mathbf{b}^*$, and $\mathbf{c}^*$, which are related to the real-space unit cell vectors $\mathbf{a}$, $\mathbf{b}$, and $\mathbf{c}$ by the following relations:

$\mathbf{a}^* \cdot \mathbf{a} = 1$, $\mathbf{b}^* \cdot \mathbf{b} = 1$, $\mathbf{c}^* \cdot \mathbf{c} = 1$, with all other dot products of $\mathbf{a}^*$, $\mathbf{b}^*$, or $\mathbf{c}^*$ and a real space unit cell vector being zero ($\mathbf{a}^* \cdot \mathbf{b} = 0$, etc.) The vectors $\mathbf{a}^*$, $\mathbf{b}^*$, and $\mathbf{c}^*$ define the reciprocal lattice. The real-space unit cell vectors $\mathbf{a}$, $\mathbf{b}$, and $\mathbf{c}$ need not be the primitive unit cell vectors; the vectors used to define the reciprocal lattice depend on the choice of unit cell, but it can be shown that the reciprocal lattice itself is unique for a given real space lattice [14]. In the cubic, tetragonal and orthorhombic crystal systems, the reciprocal lattice unit cell vectors $\mathbf{a}^*$, $\mathbf{b}^*$, and $\mathbf{c}^*$ are parallel to the corresponding real-space unit cell vectors, $\mathbf{a}$, $\mathbf{b}$, and $\mathbf{c}$, respectively, but this is not true in general. The relationship between the reciprocal lattice and the diffraction geometry is particularly simple for a crystal which contains a single atom per unit cell. In that case, the atomic positions are given by $\mathbf{r}_j = U_j\mathbf{a} + V_j\mathbf{b} + W_j\mathbf{c}$, where U_j, V_j, and W_j are integers, and the unit cells are indexed by j. The reciprocal lattice vectors are given by $\mathbf{d}_{hkl} = h\mathbf{a}^* + k\mathbf{b}^* + l\mathbf{c}^*$, where h, k, l are integers. From the relations between the real-space and reciprocal unit cell vectors, it follows that

$$\mathbf{d}_{hkl} \cdot \mathbf{r}_j = (hU_j + kV_j + lW_j) \tag{2.20}$$

which is an integer by definition. Diffraction will thus occur when $\mathbf{Q} = \mathbf{d}_{hkl}$. This relation can be represented graphically by means of the Ewald sphere construction. Since $\mathbf{k_0}$ and $\mathbf{k_h}$ are of length $1/\lambda$, the set of all possible incident and scattered beam vectors defines a sphere of radius $1/\lambda$. A two-dimensional section of this sphere is depicted in Fig. 2.12. The origin of the reciprocal lattice is at the point O on the surface of the sphere. Rotation of the crystal in real space corresponds to rotation of the Ewald sphere about the point O. Diffraction occurs when the Ewald sphere intersects a reciprocal lattice point (other than the origin); i.e. when the vector $\mathbf{Q}$ coincides with a reciprocal lattice vector.

The integers h, k, l are referred to as the *indices of the reflection* (the term *reflection* for a diffraction condition arises from the concept of reflecting planes in Bragg's law). If h, k and l have no common factor, they correspond to the Miller indices of the reflecting planes [14], and the reflection is the lowest order diffraction from that set of planes. Higher order diffraction conditions from the same set of planes have indices of reflection given by nh, nk, nl, where n is the diffraction order occurring in Bragg's Law (2.18). One also encounters the condition for diffraction written so as to incorporate

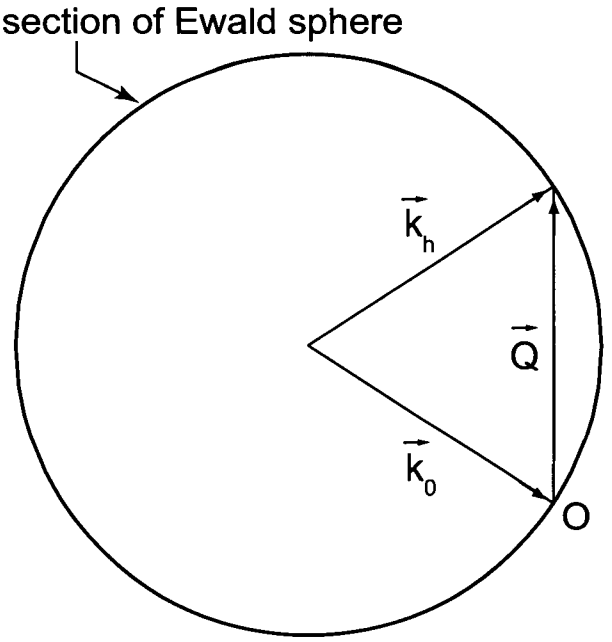

Figure 2.12: The Ewald sphere construction (after Bowen and Tanner [13]).

the diffraction order into the plane spacing:

$$\lambda = 2d_{hkl} \sin\theta \tag{2.21}$$

where d_{hkl} is the magnitude of the reciprocal lattice vector $\mathbf{d}_{hkl}$.

For crystals containing more than one atom per unit cell, the description of the diffraction geometry is similar, but the waves scattered from all the atoms within the unit cell must be taken into account. The positions of atoms in the unit cell are specified by $\mathbf{x}_m = u_m\mathbf{a} + v_m\mathbf{b} + w_m\mathbf{c}$, where the index m runs over atoms within a single unit cell. The scattering amplitude from the unit cell is the sum of the waves scattered by the individual atoms:

$$F_{hkl} = \sum_m f_m(\theta) \exp\{-2\pi i(hu_m + kv_m + lw_m)\} \tag{2.22}$$

where $f_m(\theta)$ are the scattering factors of the individual atoms, which depend on the type of atom and the scattering angle (F_{hkl} and $f_m(\theta)$ are actually ratios of the scattering amplitudes to that of a single electron at the origin). F_{hkl} is known as the

structure factor of the unit cell. The amplitude of the total scattered beam from the crystal, η_{hkl}, is obtained by summing the amplitudes from all unit cells:

$$\eta_{hkl} = \sum_j (hU_j + kV_j + lW_j)F_{hkl} \tag{2.23}$$

If the structure factor vanishes for a given reflection, because the sum of the waves from atoms within the unit cell is zero, then diffraction will not occur. These reflections are referred to as forbidden reflections. For example, for crystals with the diamond structure, reflections with indices $(0, 0, k)$ are forbidden except for values of k which are multiples of 4. For the III–V semiconductors having the zincblende structure (see Fig. 1.2), $(0, 0, k)$ reflections with odd k are forbidden, $k = 4, 8, \ldots$ reflections are strong and $k = 2, 6, \ldots$ reflections are weak, appearing only because of the small difference in the atomic scattering factors for the two elements, which results in incomplete cancellation of the waves.

2.3.5 Diffraction from periodic structures

The interference of x-rays provides a method to make accurate measurements of the structural properties of ultrathin layers [15]. Periodic structures, i.e. MQWs and superlattices, give rise to a characteristic diffraction pattern. This pattern consists of "satellite" peaks, whose spacing in reciprocal space corresponds to the real-space period of the structure. The pattern of satellite peaks is repeated at each reciprocal lattice point of the bulk crystal, as shown schematically in Fig. 2.13 — since the spatial period of the structure is greater than the lattice constant, the satellite peaks are more closely spaced in reciprocal space than the bulk reciprocal lattice points. The orientation of the satellite peak pattern is determined by the interface plane of the heterostructure, in this case (001). By scanning the sample axis ω, while moving the detector axis through twice the angular distance, a radial line is mapped out in reciprocal space. If the detector acceptance is only limited by a slit, as is the usual practice for rocking curve measurements, the line in reciprocal space is broadened into a wide path, with the detector integrating over a range of scattering angles.

Figure 2.14 shows a simulated rocking curve around the (004) reflection. The curve was computed by the Bede RADS software package, using dynamical diffrac-

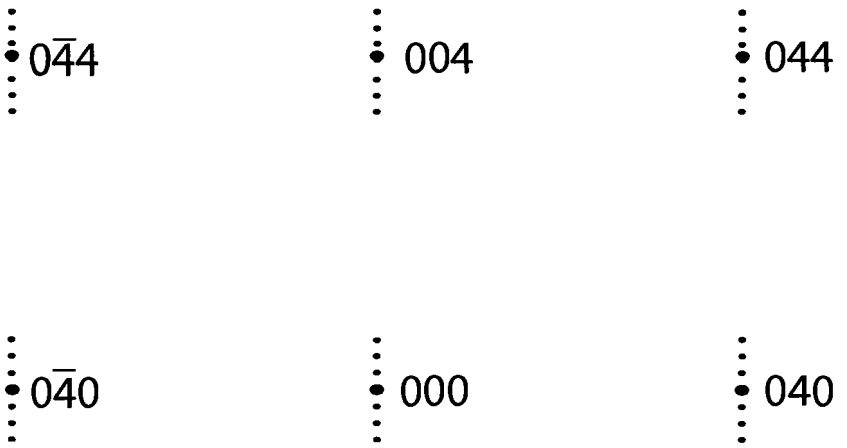

Figure 2.13: Diffraction from a periodic structure in a planar section of reciprocal space.

tion theory. The structural model for the computation consists of a 12-period MQW structure with 1 ML thick InAs quantum wells and 108 Å thick GaAs barrier layers. The satellite peaks (labelled SL, with the subscript denoting the diffraction order) appear to either side of the substrate diffraction peak. The spacing of the satellite peaks is determined by the MQW period. The weaker fringes appearing between the satellite peaks result are known as Pendellösung fringes, and their spacing is determined by the total thickness of the MQW structure [15]. The position in reciprocal space of the zeroth-order satellite SL_0 is determined by the average perpendicular lattice constant of the MQW structure:

$$a_{\perp}^{(av)} = \frac{L_w a_{\perp}^{(w)} + L_b a_{\perp}^{(b)}}{L_w + L_b} \tag{2.24}$$

For structures consisting of binary compounds, the lattice constants of the well and barrier materials, $a_{\perp}^{(w)}$ and $a_{\perp}^{(b)}$, are known — they can be computed from (5.16). Therefore, the thicknesses of the well and barrier layers, L_w and L_b, can be determined from the position of the SL_0 peak and the spacing of the satellite peaks, in the experimental rocking curve. For thick layers, kinematical theory is adequate for this purpose, but for heterostructures whose total thickness is less than 1000 Å, the SL_0 peak position predicted by kinematical theory diverges from the experimental values

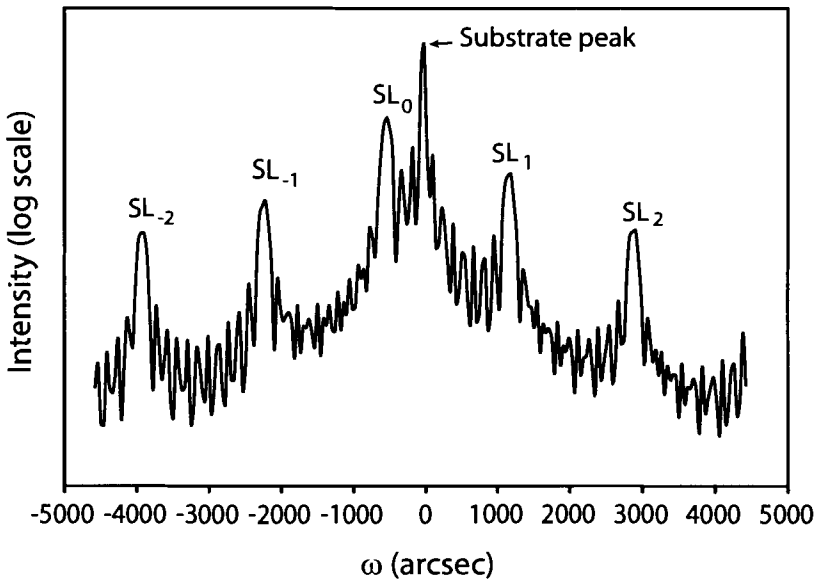

Figure 2.14: Example of a (004) rocking curve from a 12× MQW structure (simulated).

due to interference effects [13]. Dynamical diffraction theory correctly predicts the position of the peak for both thick and thin layers. Using the RADS software the layer thicknesses can be easily determined by adjusting the model input parameters until the positions of the peaks in the simulated curve match those in the experimental data.

If one or both of the materials in the MQW structure are alloys, then the perpendicular lattice parameters depend on the respective alloy compositions of the layers. The layer compositions are typically not accurately known *a priori*. The thicknesses and compositions of the layers cannot be determined unambiguously from the satellite peak positions in a MQW rocking curve; only the MQW period and the average strain are constrained. The intensities of the satellite peak positions can be used to place constraints on the alloy compositions, but the dependence of the intensities on the structural parameters is quite weak. Some examples of rocking curves of MQW structures with the same average strain, but different layer compositions and thicknesses, are discussed in section 4.1.1.

2.4 Atomic force microscopy

Atomic force microscopy is a scanning probe technique used to map the surface topography of a sample. In the work presented in this thesis, it is used to study the critical thickness of strained GaSb layers, by checking for the presence of three-dimensional (3D) dots or islands on the surface. The vertical resolution of the atomic force microscope (AFM) is on the order of angstroms, while the lateral resolution depends on the type and condition of the probe tip.

The instrument used for AFM measurements is a Park Scientific Instruments Autoprobe CP. A schematic diagram of the apparatus is shown in Fig. 2.15. The cantilever and nanometre-scale tip are formed from crystalline silicon. The cantilever is thin enough that the interatomic forces between the tip and the sample surface cause a measurable deflection of the cantilever. The deflection is measured by a laser beam, which reflects from the top side of the cantilever. An array of two photodiodes detects the laser beam, with the difference in signal between diode A and diode B depending on the deflection angle. The AFM is operated in feedback mode, in which the sample is moved vertically to keep the cantilever deflection constant, as the tip scans across the surface. Thus, there is no need to calibrate the photodiode difference signal to the vertical deflection, as the topographic height is measured by the vertical component of the sample motion. Both the vertical movement and the lateral scanning motions are performed by the piezoelectric scanner, which is mounted under the sample stage.

The interatomic force, as a function of the distance between the sample and the probe tip, is illustrated schematically in Fig. 2.16. For larger distances, attractive Van der Waals forces are dominant, whereas at closer range the repulsive electrostatic force dominates. Note that the crossover from attractive to repulsive net force is used to define the zero point of the tip-sample distance, which would be difficult to define precisely otherwise. The AFM may be operated in either regime. Operation with a net repulsive force is referred to as contact-mode AFM, while operation with an attractive force is called non-contact mode AFM.

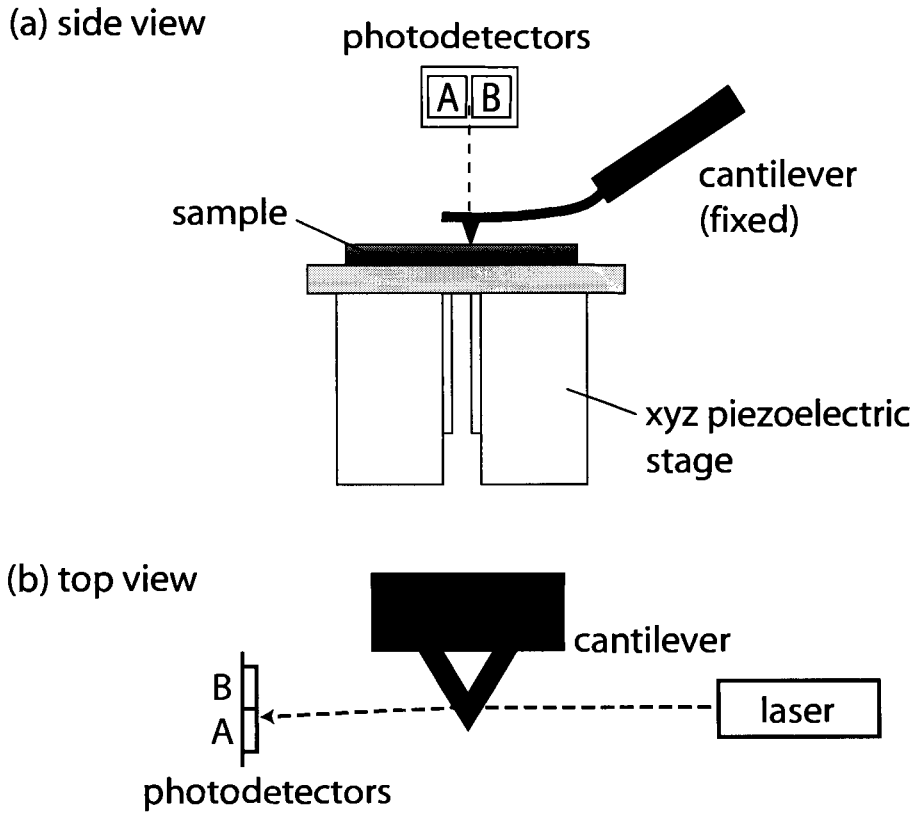

Figure 2.15: Schematic diagram of the atomic force microscope.

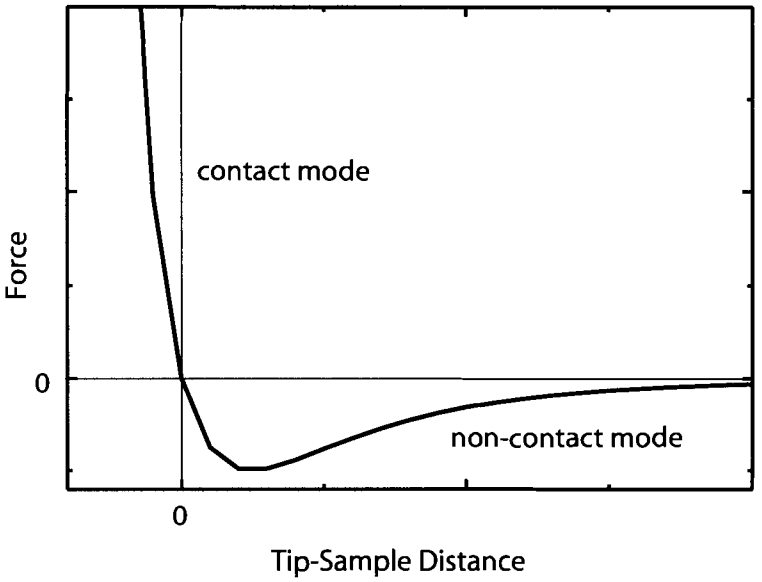

Figure 2.16: Schematic graph of the interatomic force as a function of the distance between the sample and the probe tip.

2.5 Photoluminescence spectroscopy

In order to study the electronic energy levels of ultrathin quantum well structures, the optical emission arising from transitions between energy levels is analyzed spectroscopically. The luminescence from a material excited by absorption of photons of a higher energy than the emitted photons is known as photoluminescence (PL). The process involves three steps: The material is excited by absorption of photons from an external source, creating electron-hole pairs. The excited electron-hole pairs then thermalize, i.e., they relax toward a quasi-thermal-equilibrium distribution. The electron-hole pairs recombine emitting photons, typically before reaching the quasi-equilibrium distribution. Since the distribution functions for electrons and holes are exponentially decaying, the PL emission is dominated by the lowest-energy available transitions [4]. In PL spectroscopy, the optical emission is analyzed spectroscopically, in order to determine the transition energies. The photoluminescence experiments to collect the data presented in Chap. 5 were performed at Simon Fraser University (SFU) by James Stotz and Thomas Meyer. A brief overview of the technique

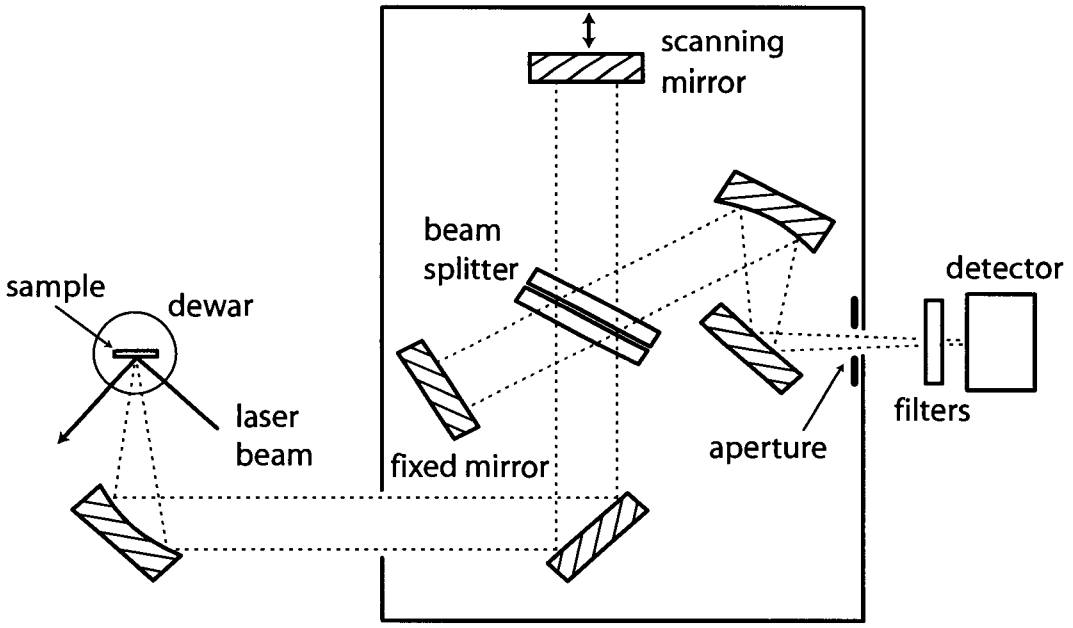

Figure 2.17: Schematic diagram of the Fourier transform photoluminescence spectroscopy setup, after Ref. [17].

is presented here. For a more detailed presentation of the apparatus and typical procedures, see Ref. [16].

The sample is contained in a Janis Varitemp dewar, and can be cooled to the temperature of superfluid liquid He. The dewar has optical windows to allow the optical excitation of the sample, and the collection of emitted light. The exciting beam is produced by a multiline continuous-wave argon ion laser. The excitation power density can be varied between 0.1 $mWcm^{-2}$ and 10 Wcm^{-2}. The emitted luminescence is analyzed by a Bomem DA8 Fourier transform spectrometer. The spectrometer, shown schematically in Fig. 2.17, consists of a Michelson interferometer. By scanning one arm of the interferometer, the Fourier transform of the emission spectrum is collected. The spectrum in the energy domain is obtained by computing the inverse Fourier transform of the data using a fast Fourier transform algorithm.

2.6 Transmission electron microscopy

A number of images obtained by transmission electron microscopy (TEM) of cross-sectioned MQW samples are presented in Chap. 4; the experimental work was performed by Victoria Fink at SFU. The TEM specimens were prepared by cleaving the wafer into 1–2 mm wide strips, which were then epoxy bonded to form a "sandwich" with the epitaxial layers in the centre. The sandwich was then mechanically thinned to 15 μm and further thinned by argon ion milling at an angle of 10° to the surface at liquid nitrogen temperature. This preparation procedure results in a wedge shape, which ensures that a part of the sample is thin enough for electrons to penetrate it. The electron microscope is a Hitachi 8000 with an accelerating voltage of 200 kV. The images were obtained in the bright-field mode with the specimen in the (004) diffracting condition. In bright-field imaging, electrons that are scattered by the sample are stopped by the objective aperture, and the image is formed by focusing the unscattered direct beam electrons onto a screen or a photographic film. The image contrast is determined by the amount of scattering; regions where few electrons are scattered appear bright, while those where more electrons are scattered appear darker. In crystalline specimens oriented so that the incident beam satisfies a diffraction condition, the contrast is primarily influenced by the local strain field. In interpreting the images, particularly where ultrathin layers are concerned, the thickness of the TEM specimen (which is considerably thicker than a single atomic layer) should be kept in mind. It is in general not possible to determine a detailed compositional profile from the image contrast.

Chapter 3

Surface studies

A crucial role in epitaxial growth is played by the surface reconstruction — it determines the kinetic factors for adsorption, desorption and surface diffusion, and provides the template for nucleation [18]. At a crystal surface, the translational symmetry of the perfect crystal is broken. In general, the lattice spacing at the surface, in either the perpendicular or lateral direction, need not be the same as that of the bulk. On semiconductor surfaces, the atoms typically rearrange to lower the surface energy. This can occur, for example, by the formation of dimers, which reduces the density of dangling bonds at the surface. The rearrangement of atoms at the surface is termed a surface reconstruction. Semiconductor surface reconstructions tend to exhibit lateral periodicities which are multiples of the bulk periodicity at the surface. A simple way of classifying surface reconstructions is to use Wood's notation [19]; the reconstruction is denoted by $(n \times m)$, where n and m are the factors by which the periodicity of the surface differs from that of the bulk structure in two crystallographic directions. If a centred mesh is chosen to represent the surface structure, the notation $c(n \times m)$ is used.

3.1 Surface reconstructions and optical anisotropy

Although the atomic positions in the bulk of cubic semiconductors are symmetric with respect to the 90° rotation between the [110] and [$\bar{1}$10] axes, this is not the case for the surface; the reconstructed surface may possess a lower symmetry in both the

atomic positions and the orientation of dimer bonds. This results in optical anisotropy, which is detected by RDS measurements. Spectroscopic features may arise either from transitions between electronic states involving only surface dimers and bonds, or from modification of bulk states by the surface.

The theory of the optical response to surface features is not presently well enough developed, to permit a determination of an unknown surface reconstruction from RDS data. However, a catalogue of RD spectra has been established, representing the various surface reconstructions observed for some common materials. The correspondence between the spectra and the surface periodicity was established by performing RDS simultaneously with elecron diffraction techniques in ultra high vacuum [20] and with grazing incidence x-ray scattering (GIXS) in the OMVPE environment [21, 22]. Fig. 3.1 shows the RD spectra observed for three reconstructions of GaAs (001). Under typical OMVPE conditions, the As-terminated reconstuctions, $c(4 \times 4)$ and (2×4), are commonly observed, whereas the (4×2) Ga-terminated reconstruction is rare. References occur in the literature to a disordered variant of the $c(4 \times 4)$ surface, which is given the name $d(4 \times 4)$. However, the work of Kamiya *et al.* [22] provided direct evidence of the long-range order occurring in the OMVPE environment; the RD spectra which had been previously given the $c(4 \times 4)$ and $d(4 \times 4)$ nomenclatures were shown to correspond to $c(4 \times 4)$ or tetragonally distorted $c(4 \times 4)$ long-range order, depending on the exact conditions. Also, there is more than one surface structure with (2×4) periodicity; two such structures that occur in OMVPE are termed the $\beta 2(2 \times 4)$ and $\alpha(2 \times 4)$ reconstructions. The RD spectrum of the latter, less As-rich structure is distinguished from the former mainly by a downward shift of the entire spectrum [23]. From here on in this thesis, the GaAs (001) RD spectra will be categorized simply as either $c(4 \times 4)$ or (2×4), since the distinctions of tetragonal distortion and degree of long-range order are difficult to make reliably based on RDS data alone. It is worth noting that RDS is in fact primarily sensitive to short-range rather than long-range order; spectroscopic features are also observed for surfaces on which the long-range order is disrupted, such as the growing GaAs surface [21].

The physical origins of the features in the RD spectra of GaAs(001) reconstructions have been discussed in a number of articles. In particular, the negative feature at 1.9 eV (at 500 °C; the spectral position has a temperature dependence which follows

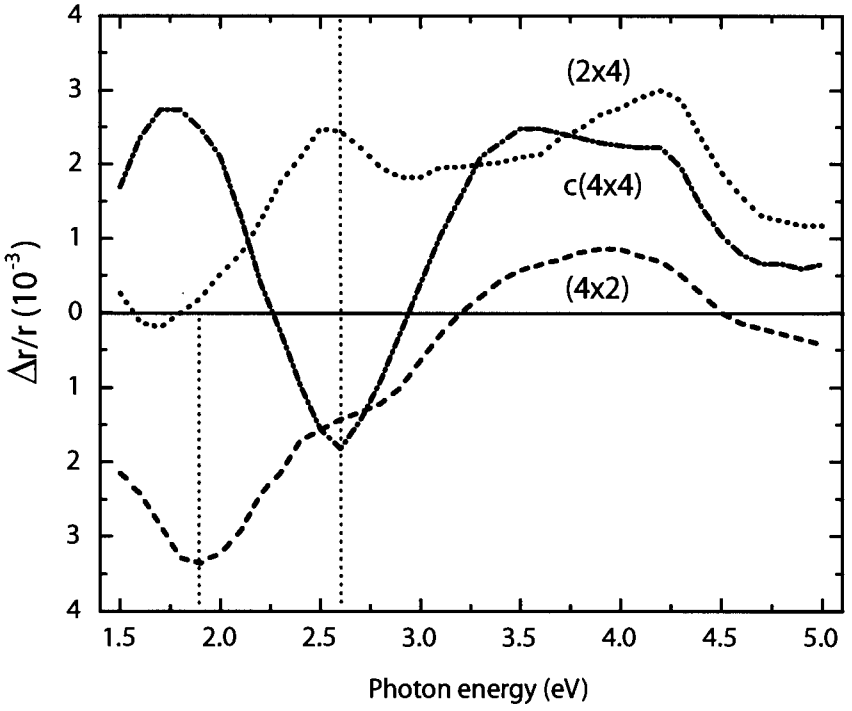

Figure 3.1: RD spectra of the (2×4) (585 °C), $c(4 \times 4)$ (473 °C), and (4×2) (592 °C) reconstructions, after Kamiya *et al.* [20]

that of the GaAs band gap) which appears in RD spectra of Ga-terminated (4×2) and (4×6) reconstructions is identified with optical transitions between occupied gallium dimer and unoccupied dangling-bond bands [20, 24]. The positive feature centered at 2.6 eV in the (2×4) RD spectrum was originally attributed to transitions between surface states involving As dimers oriented along $[\bar{1}10]$ [24]. However, this point has been controversial, with some authors claiming that the feature arises primarily due to the perturbation of bulk states by the surface termination [25, 26], while others found evidence for a dimer-related origin [27–29], or the coexistence of nearly degenerate bulk-related and pure surface transitions [30]. Recent measurements using electron energy loss spectroscopy, however, found direct experimental evidence for surface transitions at 2.6 eV, distinct from the E_1 bulk critical point at 2.9 eV [31]. The 2.6 eV feature is positive for the (2×4) reconstructions, which are characterized by As dimers oriented along $[\bar{1}10]$. The $c(4\times4)$ reconstruction, on the other hand, consists of $\frac{3}{4}$ ML of As dimers oriented along [110] above a full ML of As, and shows a negative RD feature at 2.6 eV [20].

Pristovsek *et al.* discuss the time dependence of the 2.65 eV RD signal during transitions between different GaAs (001) surface reconstructions [23]. Intermediate surfaces often consist of differently reconstructed domains, and the RD signal is the sum of the signals from each domain. In this case, the RD signal is proportional to a characteristic arsenic coverage Θ, which is a weighted average of the coverages of each domain. If the reaction rate follows a simple power law, the time dependence of the surface coverage is given by

$$-d\Theta/dt = k\Theta^n \tag{3.1}$$

where k is the rate constant and n is the reaction order. For arsenic desorption under OMVPE conditions, both zeroth order (linear time dependence) and first order (exponential) reaction rates have been observed, depending on the temperature. The zeroth order reaction rate was attributed to desorption via an intermediate state occurring at step edges, whereas a first-order rate is the expected form for As dimer desorption directly from surface terraces [23]. Six distinct processes were identified, corresponding to transitions between different surface reconstructions. From the temperature dependence of these reaction rates, activation energies for the different processes were

calculated, ranging from 2.36–2.8 eV.

Despite the usefulness of RDS as a surface characterization tool, it is important to keep in mind that the spectra may include bulk-related components. Optical anisotropy can arise in otherwise isotropic cubic semiconductors through the linear electro-optic (LEO) effect, which couples an electric field to the indices of refraction of the material. Also, during heteroepitaxial growth, oscillations resulting from Fabry-Perot interference can sometimes be observed. A growing epilayer will exhibit periodic oscillations in the intensity of reflected light at a given wavelength, λ, as the interference between the reflections from the top and bottom of the epilayer becomes alternately constructive and destructive — one period of oscillation corresponds to growth of a thickness λ/n, where n is the refractive index. The Fabry-Perot oscillations also appear in the RD signal, due to the interference between the anisotropic reflection at the surface and the reflection from the buried interface. The oscillations show a damped sinusoidal behaviour as a function of time, since the incident light is strongly absorbed by the epilayer. A model calculation based on the interference between reflections from thin anisotropic surface and interface layers was found to be in good agreement with experiments [32]. It is interesting to note that, while the Fabry-Perot effect results in intensity oscillations in the average reflectivity, it can cause the RD signal to oscillate from positive to negative. The oscillations have found a practical application in the *in situ* measurement of epilayer growth rates [33].

3.2 Surface studies of Sb-covered GaAs

The heteroepitaxial growth of antimonide layers involves exposure of the substrate to a source of Sb atoms. In order to better understand the bonding and atomic configuration at the GaSb/GaAs (001) interface, it is therefore of interest to study the interaction of Sb with the GaAs (001) surface. A number of previous experimental [34–43] and theoretical [44–46] studies have detailed the surface structures formed by depositing Sb onto clean (2×4) reconstructed GaAs (001) surfaces. Sb layers deposited at room temperature were annealed to successively higher temperatures and probed by reflection high-energy electron diffraction (RHEED) and x-ray photoelectron spectroscopy (XPS) [35], x-ray standing wave (XSW) experiments [36],

and scanning tunnelling microscopy (STM) [37]. In order of increasing annealing temperature, (1 × 4), (1 × 3), and (2 × 4) phases were observed. Core-level photoelectron spectra demonstrated that the GaAs surface remains As-terminated for the two lower-temperature phases, with bonds forming between the Sb and the terminating As atoms, but Sb replaces the top-level As atoms to form an Sb-terminated (2 × 4) reconstruction in the range 440 °C–560 °C [35]. Above 560 °C, the Sb desorbs leaving a Ga-terminated (4 × 2) surface [37]. The replacement of top-level As atoms by Sb is perhaps surprising in view of the large substitution energy for Sb into As sites in GaAs, 2.17 eV [47]. Maeda *et al.* suggested that the replacement occurs as a result of As evaporation, which leaves Ga dangling bonds to which the Sb atoms can attach [35]. A number of structural models for the Sb-terminated (2 × 4) reconstruction have been proposed, containing between one and three Sb dimers per unit cell [35, 37, 38, 44]. Pseudopotential calculations indicated that the three-dimer model should be energetically unfavourable [44]. STM measurements, on the other hand, showed that the (2 × 4) surface is terminated by three dimers, of which two-thirds are Sb dimers and one third As dimers, resulting in an Sb coverage of 0.5 ML [41].

Esser *et al.* annealed a room-temperature deposited Sb overlayer, and performed simultaneous low-energy electron diffraction (LEED) and RDS measurements [38]. In contrast to the studies mentioned previously [35–37], the LEED pattern showed a (1 × 1) symmetry at low temperatures, which changed to a (3 × 8) pattern upon annealing to 450 °C, and a (2 × 4) pattern once the temperature reached 500 °C. The RD spectrum of the Sb-stabilized (2 × 4) surface appeared similar to the clean GaAs (2 × 4) spectrum, with the exception of a strong negative feature at 2.2 eV, suggesting the presence of Ga dimers in the former surface [38]. The negative 2.2 eV feature was also observed in the RD spectrum of the (3 × 8) surface at 450 °C, along with positive features at 2.7 eV and 4.1 eV. When Sb is deposited at higher temperatures, the surface structure formed is different from those observed when annealing a room temperature-deposited Sb film. Exposure of the clean (2 × 4) GaAs surface to an Sb flux at 470 °C–490 °C was observed by RHEED, STM and XPS to result in a (2 × 8) superstructure, containing about 1 ML Sb coverage [41, 42]. Cooling and then re-heating this surface to 460 °C in vacuum returned the surface to the Sb-terminated (2 × 4) structure [41].

Exchange reactions can play a significant role in interface formation; they involve the interchange of an atom in the crystal with a different species from the vapour phase. For III–V compounds, which are typically grown with a group V overpressure, anion exchange reactions are of particular importance. Based on the relative bond stabilities of the group III elements to Sb, As and P, one might expect P to replace As preferentially, and As to replace Sb. However, the experiments by Maeda *et al.* [35] found that Sb can replace As in the top monolayer of GaAs, as was discussed above. On GaSb, on the other hand, exposure to an As_2 flux results in strong As-for-Sb exchange, forming 3D clusters [48]. Several experiments have confirmed that As rapidly displaces P, whereas P exchanges slowly for As under typical OMVPE conditions [49–51]. Wang *et al.* point out that the relative bond strengths cannot be used to determine whether a given exchange reaction will occur or not, but rather the change in the Gibbs free energy determines the extent to which exchange occurs [52]. Their thermodynamic model predicts that either weak-for-strong or strong-for-weak bond exchange can occur, with the equilibrium point depending strongly on the exposing flux, as well as on other factors such as misfit strain, surface structure, surface energy and surface segregation.

3.3 RDS of Sb on the GaAs (001) surface

In this section, the results of our experiments on the exposure of GaAs (001) to Sb in the OMVPE environment are reported. The organometallic precursor compound TMSb is used as the source of Sb atoms. RDS was used to characterize the surface under static conditions and during GaAs growth. This technique was used to obtain both spectroscopic and time-dependence data, allowing an evaluation of the kinetics of the surface under exposure to the two group V precursors, TMSb and TBAs.

3.3.1 Stabilized RD spectra

In order to obtain conventional RD spectra, it is necessary to prepare a stable surface, because of the time required for collecting the data and moving the spectrometer through the desired wavelength range. One way to ensure that the surface is stable

is to monitor the RD signal at a fixed wavelength. In most cases, we use 476 nm (2.6 eV), which corresponds to the negative peak in the GaAs $c(4 \times 4)$ spectrum, as the default monitoring wavelength for GaAs-based structures. Following a change in the precursor flows to the reaction chamber, the RD signal typically exhibits a transient response, which evolves to a stable level over a certain period of time. Fig. 3.2 shows RD transients obtained in this way, when the GaAs (001) surface is exposed to TMSb at different temperatures. At each temperature, a clean GaAs surface was first prepared by holding the sample under a constant TBAs supply until a stable signal was obtained. At $t = 0$, the TBAs flow was interrupted, and at $t = 2$ s, TMSb was introduced using a molar flow rate of 3×10^{-5} mol/min. The interruption (or "purge") between the two precursors is a commmon practice in OMVPE growth — the purge serves to minimize diffusive mixing of the two precursor compounds in the gas stream. The initial change in the RD signal during the two second purge is due to desorption of As from the surface.

Under TMSb flow, the RD signal changes and eventually stabilizes. The rate of stabilization is strongly temperature-dependent, with faster stabilization at higher temperatures. At 460 °C and 500 °C, the signal rises under TMSb exposure. At 540 °C and 580 °C, the signal rises initially, then decreases to a level which is higher than the TBAs-stabilized level. At 620 °C and 660 °C, there is a short initial rise, associated with the 2 s purge, but the signal decreases as soon as TMSb is introduced. The stable level under TMSb is the same as under TBAs at 620 °C, and slightly lower at 660 °C. The rise-and-fall behaviour of the signal suggests that two different processes with different rates are present. These are likely to be the desorption of As from the surface, and a rate related to either the adsorption of Sb, or Sb-for-As exchange in the top monolayer. The rate at which Sb can adsorb may also be limited by the cracking rate of TMSb, which is incompletely dissociated at 500 °C [10].

Once a stabilized surface was obtained under TMSb at each temperature, an RD spectrum was recorded. The TMSb exposure was followed by growth of a GaAs buffer layer, after which the temperature was raised by 40 °C. The surface was then held under TBAs until the signal stabilized to re-establish a clean GaAs surface, and an RD spectrum of the clean surface was collected. This procedure ensured that the starting surface at each temperature was essentially free of residual Sb. The TBAs-

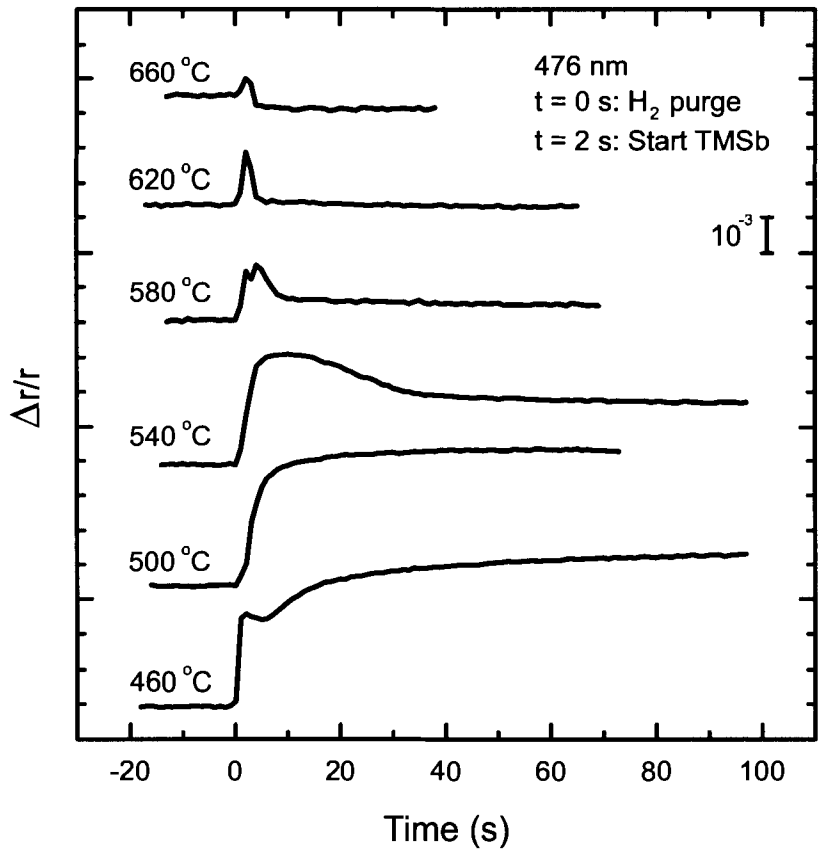

Figure 3.2: RD transients at 476 nm (2.6 eV) showing the different stabilization rates under TMSb at different temperatures.

stabilized and TMSb-stabilized spectra are shown in Fig. 3.3. The major features of the RD spectrum of the TMSb-exposed GaAs(001) surface are a negative peak at 1.7–1.9 eV, a positive peak at 3.7–3.9 eV, and a local maximum at 2.4–2.5 eV, with the exact positions depending on the temperature. The spectral positions of these features coincide approximately with the positions of features observed for the various reconstructions of Sb-free GaAs (001), which were discussed in section 3.1. However, the overall line shape of the RD spectrum of the TMSb-exposed surface is different from those of any of the Sb-free GaAs reconstructions. The TMSb-exposed RD spectrum at 460°C shows a strong resemblance to the previously reported RD spectrum obtained by annealing a room-temperature deposited Sb film to 450 °C [38] — the surface of that film was reported to have a (3×8) symmetry, as discussed in section 3.2.

The greatest change with temperature occurs in the local maximum at ~ 2.4 eV. This feature is positive at 460 °C and 500 °C, but it decreases in magnitude with increasing temperature and becomes negative overall at 540 °C and above. The 3.9 eV peak shows only a slight decrease in magnitude with increasing temperature over the range 460–660 °C. The difference between the spectra under TBAs and TMSb is roughly constant at this energy, since the magnitude of the 3.9 eV peak in the $c(4 \times 4)$ spectrum also decreases with rising temperature. The peak in the spectrum under TMSb, however, shows a slight shift from 3.9 to 3.7 eV with rising temperature, whereas this is not observed for the $c(4 \times 4)$ spectrum. The simultaneous occurrence of both a 1.7 eV negative feature and a 2.4 eV positive feature is unusual, considering that this does not occur for Sb-free Ga- or As-terminated GaAs (001). The negative peak at 1.9 eV becomes stronger with rising temperature between 460 °C and 540 °C, but stays roughly constant for higher temperatures. The assignment of this peak to transitions involving Ga dimers [24] suggests that the surface becomes richer in Ga dimers with increasing temperature in the range 460–540 °C, due to desorption of top-layer As from the surface. At higher temperatures, the RD spectra start to resemble the Ga-terminated (4×2) spectrum shown in Fig. 3.1, but with a strong positive anisotropy at 3.9 eV. No spectrum resembling the one reported for the (2×4) Sb-terminated surface [38] is observed in this experiment, even at the higher temperatures. This most likely reflects suppressed Sb desorption under a TMSb flux, compared to the

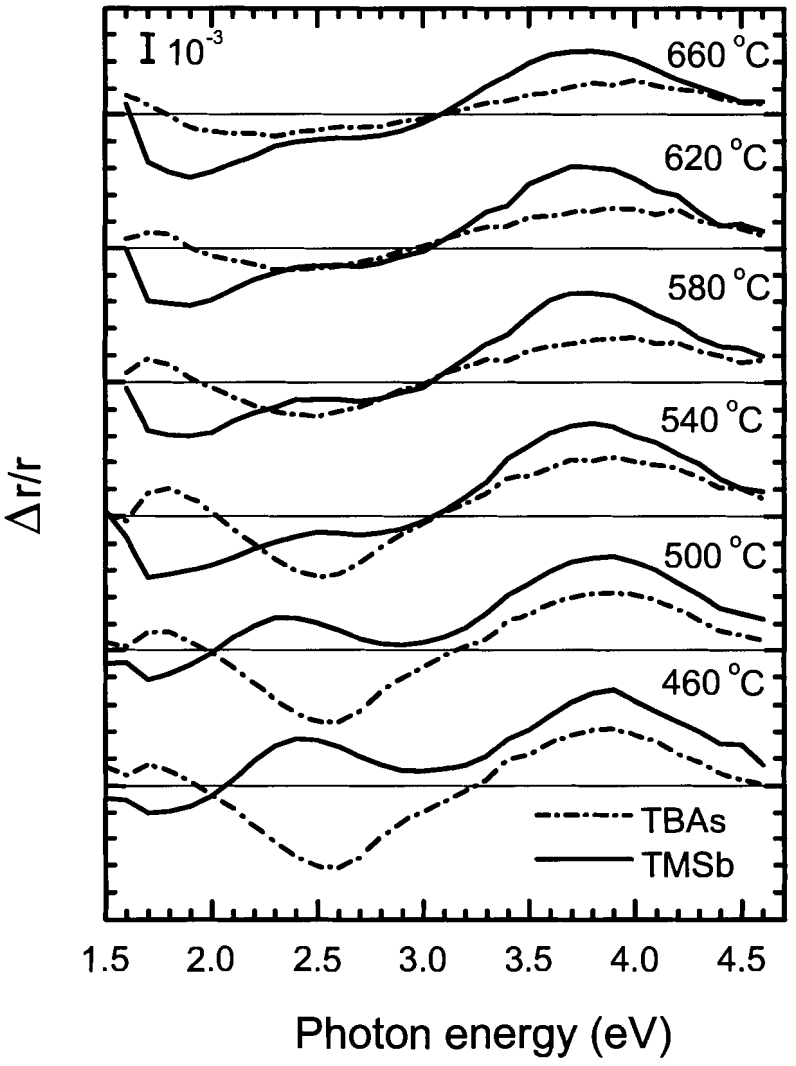

Figure 3.3: RD spectra of the GaAs(001) surface, stabilized under TMSb (solid lines) and TBAs (dash-dotted lines) at different temperatures.

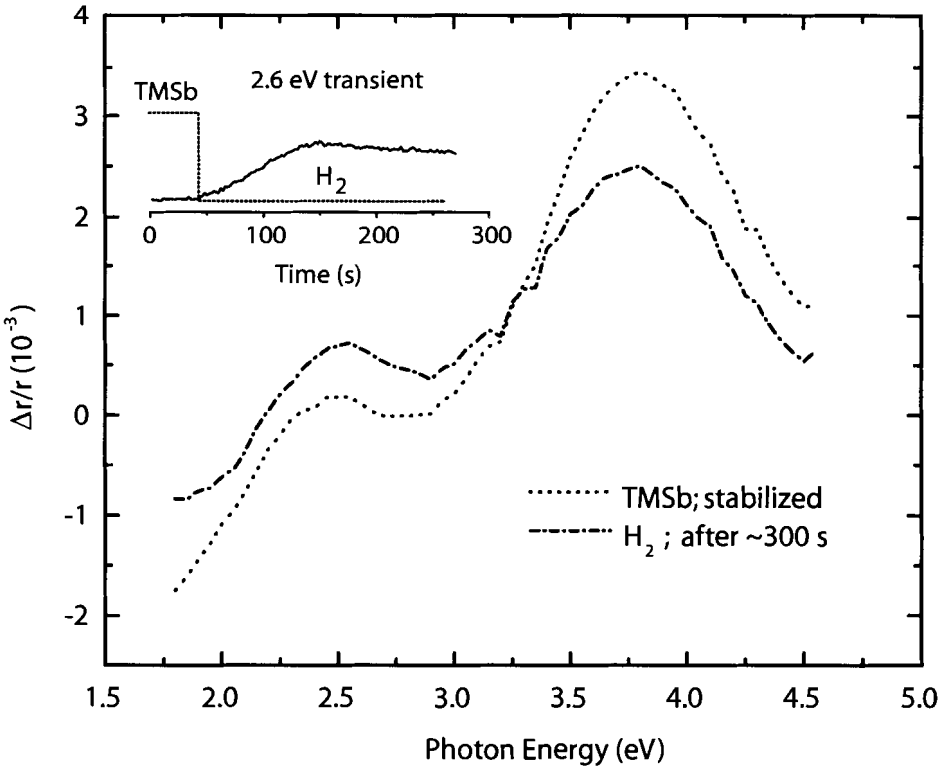

Figure 3.4: RD spectra of the stabilized TMSb-exposed surface, and the surface after approximately 300 s under hydrogen (carrier gas) only, at 500 °C. The inset shows the time dependence of the 2.6 eV signal.

ultra-high vacuum (UHV) environment employed in the former study.

Fig. 3.4 shows the change that occurs in the RD spectrum when the stable surface obtained under TMSb exposure is subsequently held under hydrogen (carrier gas) only, at 500 °C. The inset shows the evolution in time of the RD signal at 2.6 eV. The signal initially increases, then starts to decrease slowly after reaching a maximum. The signal did not reach a stable level even after 300 s, but the rate of change is slow enough that the RD spectrum may be considered representative of the surface, even though the surface continued to evolve as the spectrum was recorded. The slow rate of change of the Sb-exposed surface under hydrogen contrasts with the behaviour of the clean $c(4 \times 4)$ surface at the same temperature. As is evident from the time-resolved

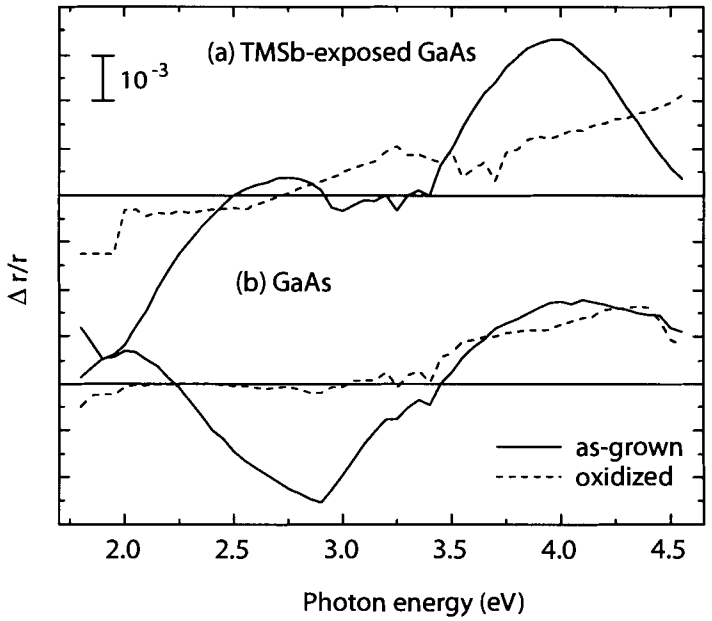

Figure 3.5: Room-temperature RD spectra of the GaAs and TMSb-exposed GaAs surfaces, in both the as-grown state and after oxidation by exposure to air for approximately one minute.

data discussed in detail in section 3.3.2 below, the $c(4 \times 4)$ reconstruction changes to a (2×4) reconstruction within 2 s when the TBAs supply is interrupted. The much slower evolution of the Sb-exposed surface is consistent with the lower vapour pressure of Sb, which leads to a slower desorption rate for Sb than for As.

Following the high temperature TMSb-exposure sequences, the samples were allowed to cool to room temperature. Fig. 3.5 shows a comparison of the room temperature RD spectra of TMSb-exposed and clean GaAs. RD spectra were also collected for these same samples, after oxidation of the surface by exposure to air for approximately 60 s. The as-grown RD spectra exhibit the same features as the high-temperature $c(4 \times 4)$ and TMSb-exposed spectra (with the spectral position of the features blue shifted by approximately 0.3 eV due to the change in the band gap energy with temperature). The RD spectra of the oxidized surfaces, on the other hand, show only a weak positive anisotropy in the upper half of the spectra. There is little difference

between the spectra of the Sb-free and TMSb-exposed samples after oxidation, which indicates that the remaining anisotropy in these spectra is of a bulk origin. On the other hand, the fact that the 1.9 eV and 2.6–2.8 eV peaks are present only in the as-grown spectra clearly supports the surface-related nature of these features. For the clean GaAs $c(4 \times 4)$ surface, the RD signal at 4 eV is only slightly higher than for the oxidized surface — indeed this feature, which is close to the E_0' bulk critical point, has been attributed to transitions between bulk states modified by the surface termination [28]. However, the positive feature centred at 3.9 eV in the spectrum of the TMSb-exposed surface is significantly stronger than the weak positive anisotropy of the oxidized spectra, pointing to a surface-related origin of this feature. It is interesting to note that a strong positive feature also appears near the same energy in the (001) RD spectra of bulk GaSb, and GaAsSb epilayers on InP [53].

3.3.2 Time-resolved RDS

The conventional RD spectra discussed in the previous section were limited to stable or very slowly evolving surfaces. On the other hand, time-resolved RDS data can be used to provide "snapshots" of rapidly changing surfaces. The basic method of collecting time-resolved RDS data was described in section 2.2. To obtain the results reported in this section, 30 period OMVPE sequences were employed, in order to obtain spectra from 1.6–4.5 eV with a resolution of 0.1 eV. The data points at 1.6 and 1.7 eV were, however, discarded due to a poor signal-to-noise ratio (a result of the low level of light transmission in this energy range, combined with the short integrating time used for time-resolved RDS). The RD signal was collected with a temporal resolution of 0.25 s. GaAs (001) surfaces were exposed to a sequence consisting of alternate exposure to TBAs and TMSb for 20 s each. Hydrogen interrupts lasting 2 s were employed to separate the TBAs and TMSb exposure. The sequence was repeated at 500 °C, 520 °C, 540 °C, and 560 °C. It should be noted that unlike the procedure described in section 3.3.1, the OMVPE sequence used for time-resolved RDS does not ensure a clean GaAs starting surface at the start of TMSb exposure. Therefore, the evolution in time of the surface will be somewhat different from that which was discussed previously.

Fig. 3.6 shows the RD spectra at 540°C, at various time points in the sequence. The reference time point, $t = 0$, is 2 s before the end of TBAs exposure. The GaAs $c(4 \times 4)$ spectrum observed during annealing under TBAs, before the start of the alternating TMSb/TBAs exposure sequence, is shown for comparison. The RD spectra are fairly similar at all four temperatures, so only one set of spectra is plotted here. The rates of change, however, show a dependence on the temperature, and this is shown in Fig. 3.7. In this figure, the RD transients at 2.4 eV are shown, i.e., the spectral position of the peak in the TMSb-exposed spectrum is used rather than the default monitoring position of 2.6 eV. For the 540°C transient, the time points corresponding to the spectra in Fig. 3.6 are indicated, as are the periods of TBAs and TMSb exposure. The interruptions under carrier hydrogen flow are indicated by shaded areas. The switching times have been shifted to correspond to the arrival of gases at the sample surface, which occurs $\sim$ 0.8 s after the valve operation. It is interesting to note the similarity of the time and temperature dependence of the curves in Fig. 3.7 with similar data obtained under alternate PH_3 and AsH_3 exposure [49].

Near the end of the TBAs exposure step in the TBAs/TMSb sequence, at $t = 0.5$ s (Fig. 3.6), the RD spectrum shows a strong positive feature centered at 3.9 eV, similar to the feature in the stabilized TMSb-exposed surface, and a broad, weakly negative feature around 2.5 eV, which is intermediate between the positive feature seen in the TMSb-stabilized surface and the strongly negative feature of the $c(4 \times 4)$ surface. This points to the presence of residual Sb on the surface, which is consistent with a slow desorption rate of Sb, as was observed in section 3.3.1. The residual Sb is present because of the relatively short length (20 s) of the TBAs exposure. During the interrupt under carrier H_2 flow, a weak positive peak appears around 2.5 eV (Fig. 3.6, $t = 4$ s), suggesting a change of the surface to a less As-rich, more (2×4)-like character. This change is also apparent in the RD transients (Fig. 3.7) as a 2 s long step-like feature. The positive feature associated with the interrupt disappears when TMSb reaches the surface at $t = 5$ s. This accounts for the notch at 5.5 s in the RD transients. From 5.5 s to 27 s, the positive feature associated with the TMSb-stabilized surface increases in magnitude. This increase occurs more rapidly at higher temperatures. No significant change in the 2.4 eV signal occurs during the

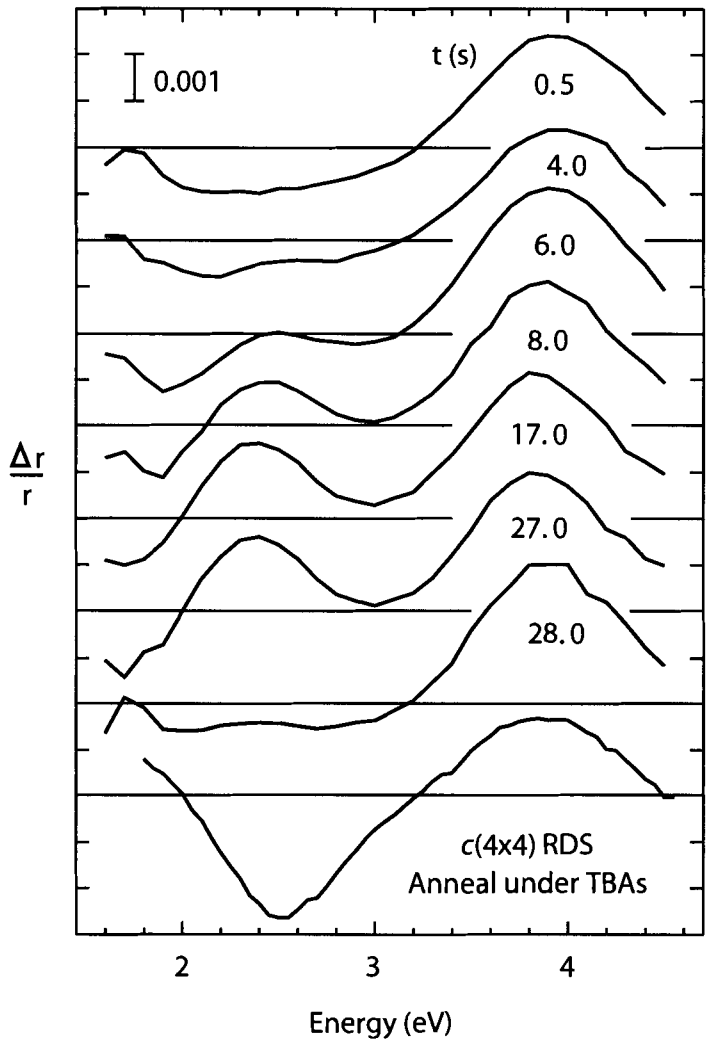

Figure 3.6: RD spectra of the GaAs(001) surface at different time points in the TBAs/TMSb exposure sequence, at 540°C. The last spectrum was obtained during the initial anneal under TBAs and corresponds to the clean, Sb-free GaAs surface.

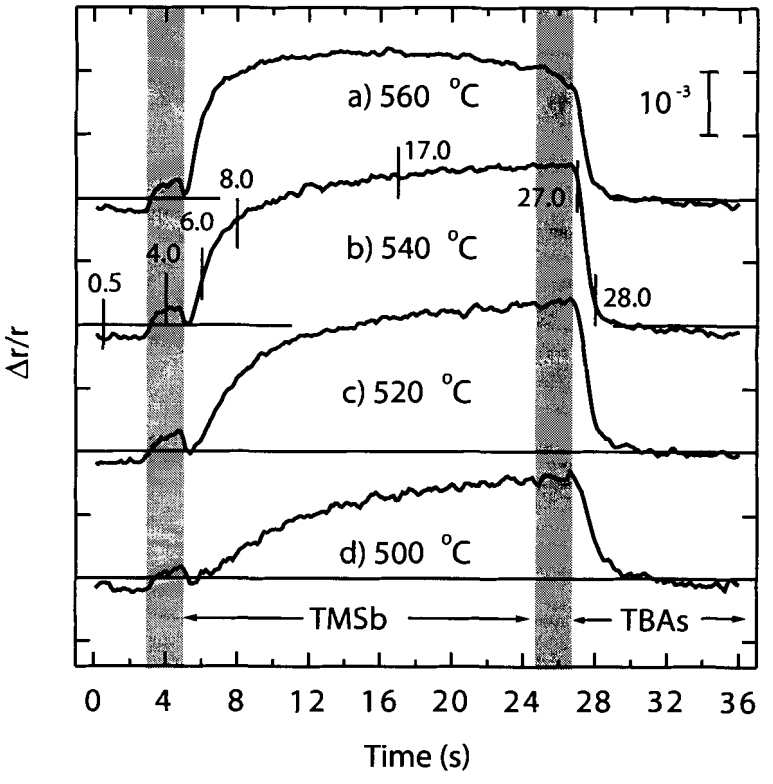

Figure 3.7: RD transients at 2.4 eV, during one period of the TBAs/TMSb exposure sequence. Shaded areas indicate H_2 interrupts. The times corresponding to the spectra shown in Fig. 3.6 are indicated on curve (b).

interrupt which follows the TMSb exposure. When TBAs reaches the surface, the RD spectrum changes rapidly (between $t = 27$ s and $t = 28$ s). The spectrum at $t = 28$ s is almost identical to the spectrum near the end of the 20 s TBAs exposure, with only a weak positive peak at 2.4 eV. The rate of change from the TBAs-exposed surface to the TMSb-exposed surface is clearly slower than the reverse process.

3.3.3 Temperature dependence of reaction rates

A semilog plot (not shown) confirmed that the rising portions of the curves in Fig. 3.7 are exponential in form. As discussed in section 3.1, an exponential time dependence of the RD signal is expected for a first-order reaction, and a rate constant can be calculated straightforwardly from a least-squares fit to the curve. In the present case, the RD signal may depend on both the Sb and As coverages, so the situation is more complicated than for As desorption from the clean GaAs surface. Nevertheless, the temperature dependence of the reaction rate offers some insight. An Arrhenius plot of the observed rate under TMSb exposure is shown in Fig. 3.8. The data show good agreement with the expected linear relationship. From the Arrhenius equation,

$$k = A \exp\{-E_A/k_B T\} \tag{3.2}$$

we obtain an activation energy E_A of 2.04 ± 0.3 eV for this reaction rate.

The GaAs (001) surface has been studied previously under PH_3 and AsH_3 exposure, using the time dependence of the RD signal. These experiments found that the activation energy for the exchange reaction under PH_3 exposure was 1.64 eV [49]. This is lower than the desorption energies of As from GaAs observed using RDS under various OMVPE conditions in the absence of a group V source, 2.36–2.8 eV [23], which indicates that the exposure to PH_3 results in an enhancement of the As desorption from the surface. The activation energy observed under TMSb exposure, 2.04 eV, is also somewhat lower than the As desorption energies, suggesting that a similar mechanism operates. The higher activation energy under TMSb, compared to phosphine, is consistent with the weaker tendency for Sb-for-As exchange than for P-for-As exchange, which was mentioned in section 3.2. The falling portions of the curves (during TBAs exposure) in Fig. 3.7 could not be assigned an activation

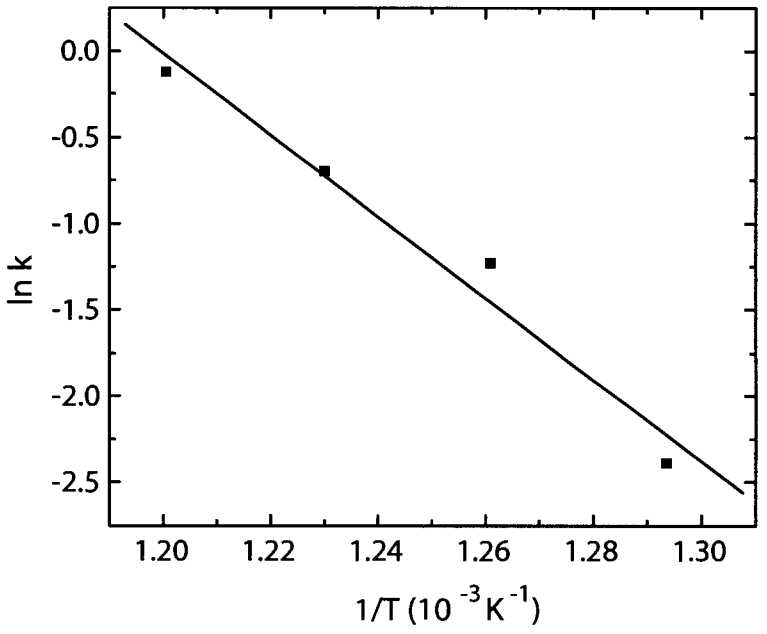

Figure 3.8: Arrhenius plot of the reaction rate observed during TMSb exposure

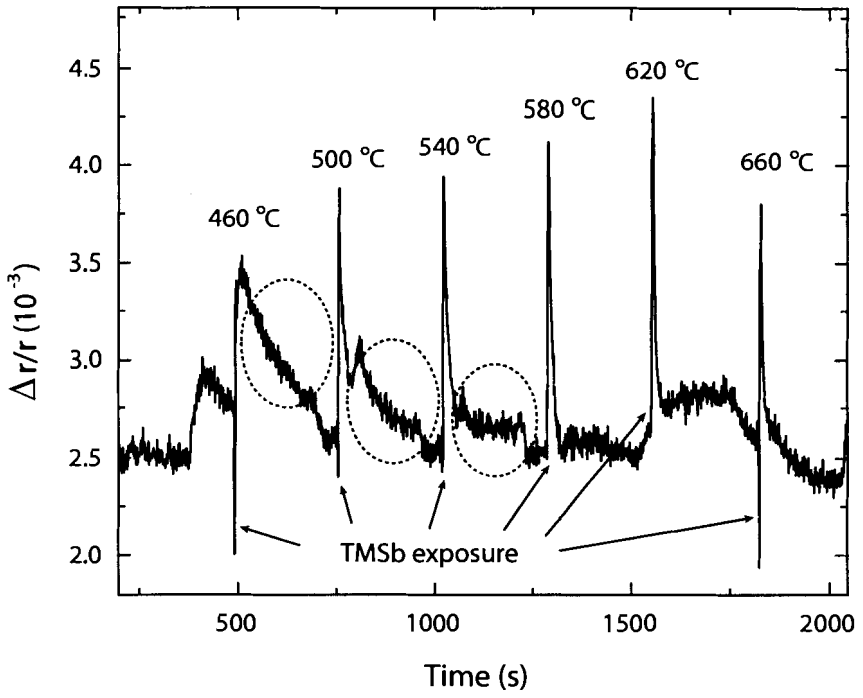

Figure 3.9: RD signal at 3.8 eV during the TMSb/TBAs exposure sequence. The "slow decay" process is circled.

energy, since the curves do not show a clear exponential or linear time dependence. The apparent rate of change in this case may be affected by the time resolution of the lock-in amplifier used to collect the data.

In order to calculate reaction rates for the TBAs exposure process, a new sequence was employed. During the run, the RD signal was collected at 3.8 eV, the position of the high-energy positive peak in the TMSb-exposed spectrum. The sequence involved exposing the GaAs surface to TMSb for 3 s at temperatures from 460 °C to 660 °C in steps of 40 °C. At each temperature, following TMSb exposure, the surface was held under TBAs until the RD signal stabilized, in order to desorb the Sb. Subsequently, the temperature was raised and a GaAs buffer layer was grown to ensure a consistent, clean starting surface, before repeating the cycle. The 3.8 eV RD transient from this sequence is shown in Fig. 3.9. At the five highest temperatures, the transient shows

an initial sharp increase immediately after the TMSb is introduced, followed by a fast decay as TBAs exposure is started. At 460 °C, on the other hand, the initial sharp increase is followed by a slower rise and decay. At 500 °C and 540 °C, a slower rise and decay follow the initial spike (the "slow decay" is indicated by dotted circles). It is not clear exactly what processes are responsible for this behaviour. One possibility is that the fast decay is related to an As-for-Sb exchange reaction, whereas the subsequent slow process is related to Sb desorption from the surface. The initial fast decay is probably due to the same process responsible for the fast decay observed in the 2.4 eV transients from the time-resolved RDS data set (Fig. 3.7). Plotting the 3.8 eV data for each temperature on a semilogarithmic scale (semilog plots are not shown) revealed that the fast decay portions of the transient are exponential, except at 460 °C, where the initial part of the transient does not show the rapidly falling behaviour. Rate constants were obtained for the temperatures from 500 °C to 660 °C by fitting exponential functions to the data. The values obtained for this process are shown as an Arrhenius plot in Fig. 3.10. An activation energy of 530 ± 60 meV is obtained from the slope of the linear fit. This agrees, within error bounds, with an activation energy reported for As-for-Sb exchange on GaSb (001) surfaces, 380 ± 80 meV, which was observed by real time line-of-sight mass spectrometry [48].

3.3.4 Sb on the growing GaAs(001) surface

So far, we have discussed the effect of TBAs and TMSb exposure on the static GaAs(001) surface. In this section, we shall present data obtained by similar methods on a growing GaAs surface. To investigate the effect of TMSb exposure on growing GaAs, 30 period OMVPE sequences were employed, in order to obtain time-resolved RDS data by the method described in section 2.2. For these growth runs, the precursor flows were 5.3×10^{-6} mol/min (TEGa) and 3.1×10^{-5} mol/min (TBAs, TMSb). The substrates were annealed under TBAs and a 100 nm GaAs buffer layer grown prior to the start of the MQW sequence — this is a typical procedure which is employed to remove surface oxide from the substrates and ensure a good quality crystal surface. For the MQW portion, the switching sequence employed was as follows: 2 s purge (H_2 carrier gas only), 3 s TMSb, 0.5 s purge, 40 s GaAs (with TEGa switched

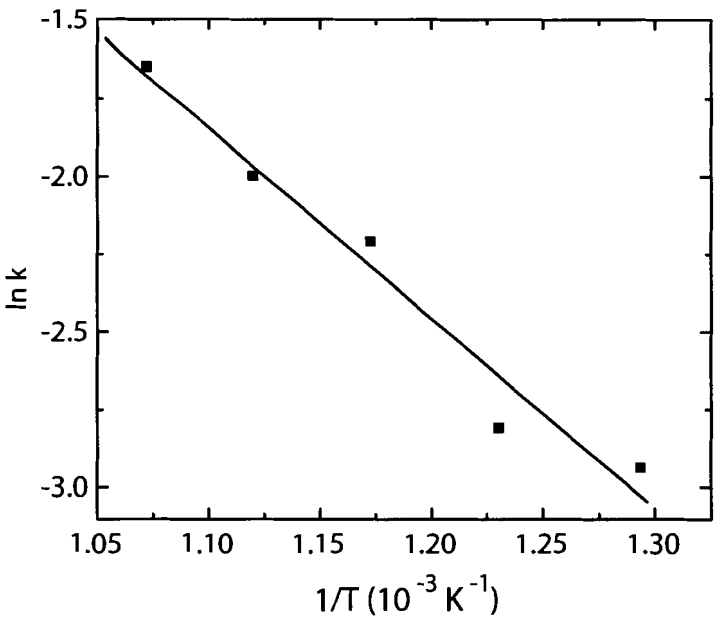

Figure 3.10: Arrhenius plot of the fast decay process under TBAs.

on 0.2 s before TBAs).

RD spectra obtained from the TMSb/GaAs growth sequence at 500°C are shown in Fig. 3.11 (a). The spectra are labelled with the time measured from the reference time point, 2 s before the end of the GaAs barrier layer growth. The "clean GaAs" spectrum observed during GaAs growth, with no Sb present, is shown for comparison. The RD transient at 2.4 eV, during the first part of the growth cycle, is shown in Fig. 3.11 (b). The time points corresponding to the spectra are indicated by dashed lines. The switching sequence is indicated above the transient (the times are shifted by 0.8 s, to indicate the arrival of precursors at the surface).

The RD spectrum observed near the end of the GaAs barrier growth is shown with the label $t = 2.0$ s. During the initial purge step, the RD spectrum evolves to a shape which is similar to the spectrum of the GaAs (2×4) reconstruction, with a positive feature at 2.6 eV. Under TMSb exposure, the 2.6 eV peak of the (2×4) spectrum first decreases ($t = 5.8$ s), then a broader positive feature centered at 2.4 eV appears, and increases in magnitude until the end of the TMSb exposure ($t = 8$ s). At this point,

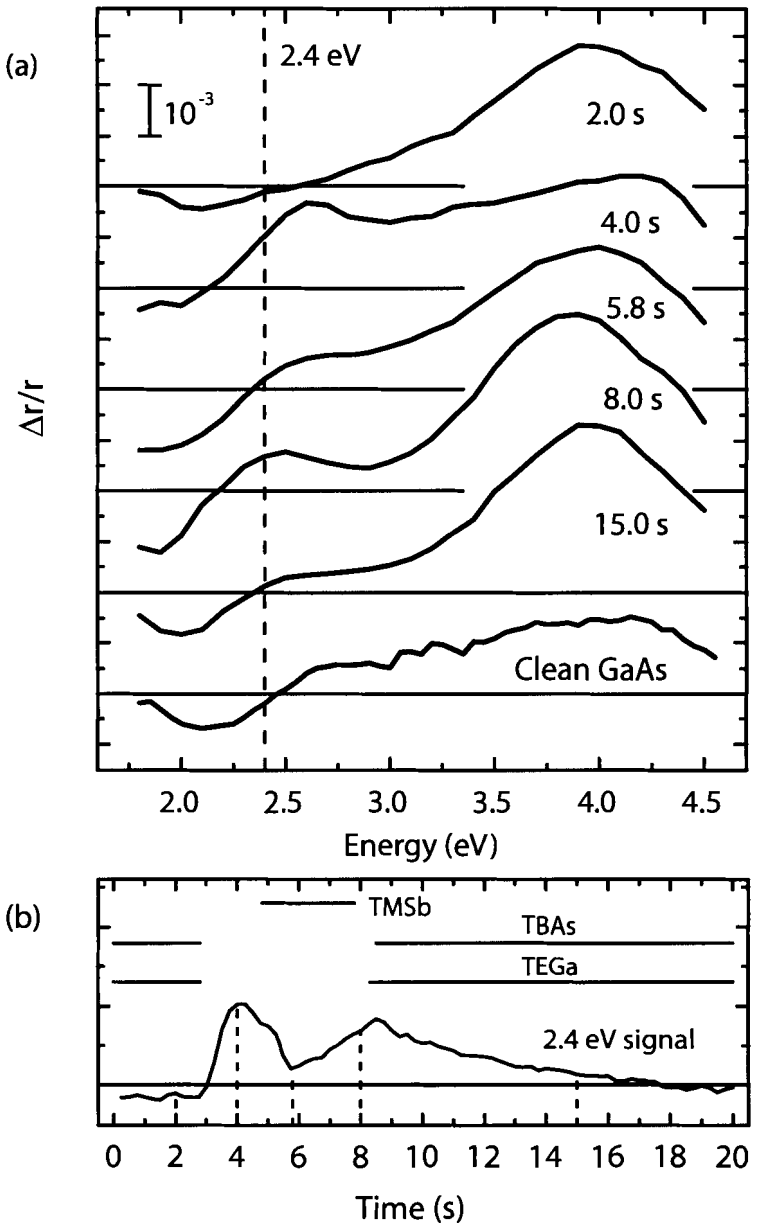

Figure 3.11: (a) RD spectra of the GaAs(001) surface at different time points in the MQW growth sequence. The "clean GaAs" spectrum is observed during GaAs growth with no Sb present. (b) 2.4 eV transient and gas switching sequence, with times corresponding to the spectra in (a) indicated by dashed lines.

the RD spectrum is similar to the TMSb-stabilized spectrum discussed in section 3.3. During growth of the GaAs barrier, following the TMSb exposure, the positive 2.4 eV feature disappears within 8 s, but the 3.9 eV feature decreases less rapidly. At the end of the barrier growth, the spectrum remains different from that which is observed for clean growing GaAs, which suggests that a floating surface layer of Sb is present on top of the growing barrier layer, modifying the surface configuration during the entire MQW growth sequence. This will be verified in Chap. 4.

In the 2.4 eV transient shown in Fig. 3.11 (b), a peak is observed during the initial purge. The signal initially drops after TMSb exposure begins, then begins to rise after 1 s. The signal continues to rise when TMSb is interrupted after 3 s exposure, then decreases gradually when TBAs is introduced. The initial peak is due to the appearance of the (2×4)-like spectrum, whereas the rise in the signal during TMSb exposure is due to the appearance of the (3×8)-like spectrum. The observation that the 2.6 eV feature first decreases, followed by the appearance of a broader 2.4 eV feature, suggests that these features are of a different origin. The transients at 2.4 eV for all four temperatures are compared in Fig. 3.12.

The incorporation of Sb into the finished MQW samples is strongly temperature dependent, as shown in Fig. 3.13. Although the Sb-related RD spectrum is observed at all four temperatures studied, the amount of Sb incorporated in the sample grown at 560°C is too low to produce detectable satellite peaks in the XRD pattern. The 540°C sample contains 0.3 ML Sb per period, whereas the 520°C and 500°C samples both contain 1.0 ML Sb per period (the method of determining the Sb incorporation from XRD data is discussed in more detail in Chap. 4. On the other hand, the RDS data indicate Sb on the surface at all four temperatures. The lack of Sb incorporation observed at 560 °C therefore indicates that virtually all of the deposited Sb remains on the surface during GaAs growth. In other words, the Sb approaches ideal surfactant behaviour as the temperature increases.

Following the completion of the final GaAs layer of the MQW growth sequences, the samples were held under TBAs at the growth temperature, in order to study the evolution of the surface. The RD signal was collected at 2.6 eV. Fig. 3.14 shows the RD transients obtained during the post-growth anneal. Following the interruption of growth, the transients show an immediate small drop, followed by a gradual linear

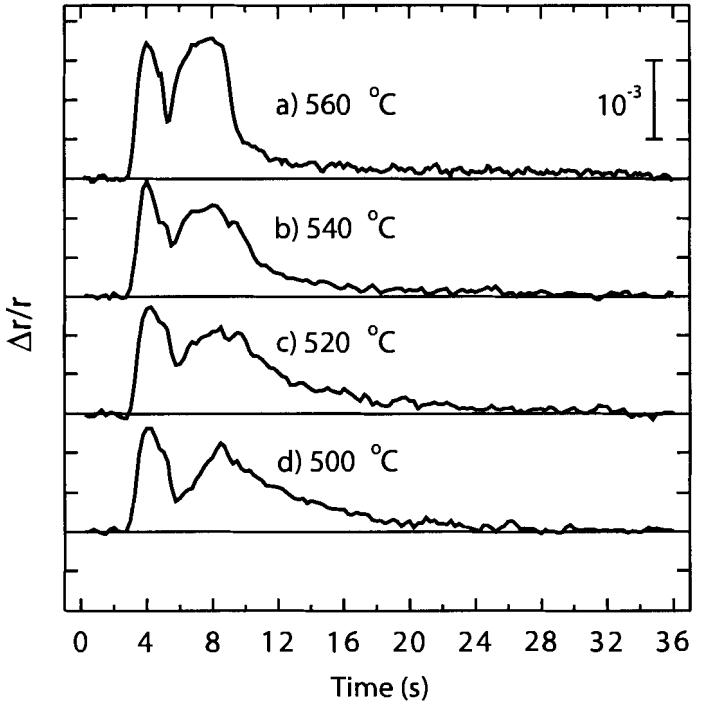

Figure 3.12: RD transients (2.4 eV) during one period of the 30× MQW growth sequence. Shaded areas indicate interrupts (carrier H_2 flow only). (a) 560°C (b) 540°C (c) 520°C (d) 500°C.

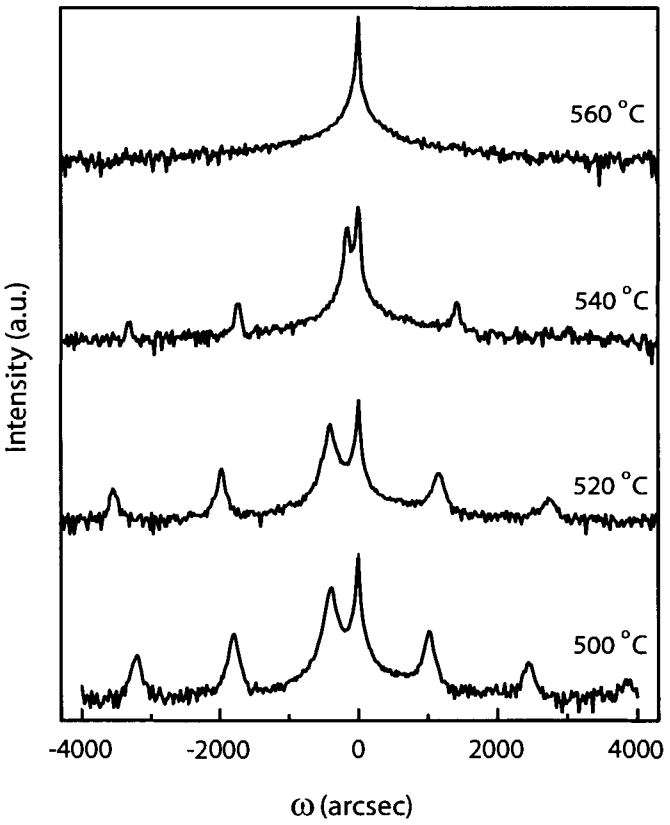

Figure 3.13: (004) XRD rocking curves for 30 period MQW samples grown at different temperatures.

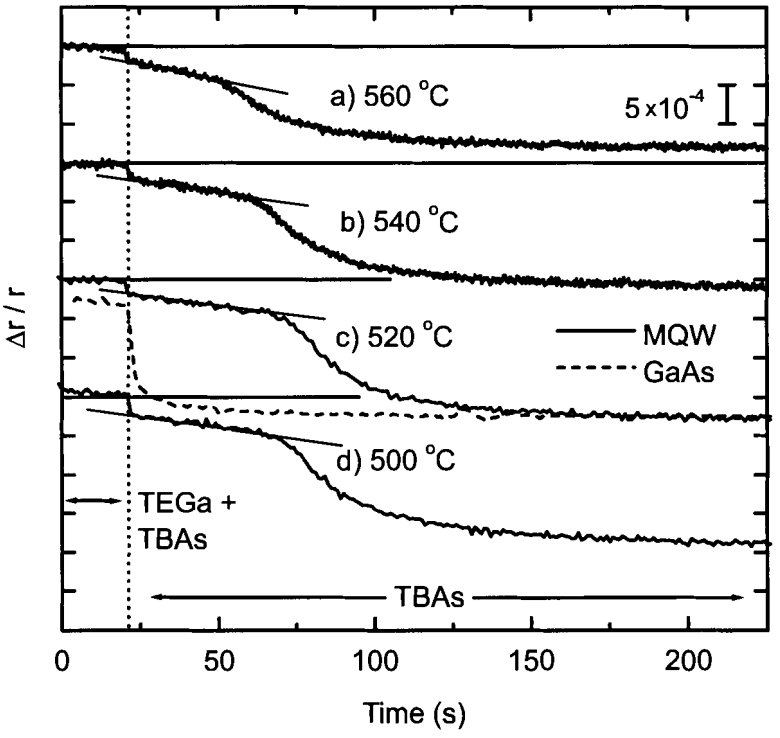

Figure 3.14: RD transients (2.6 eV) under TBAs exposure, at the end of MQW growth. Horizontal lines indicate the zero point of the RDS signal at each temperature.

decrease lasting 30–60 s, after which the signal recovers to the level associated with the clean $c(4 \times 4)$ surface. In contrast, the transient obtained for clean GaAs with no TMSb exposure recovers almost immediately to the $c(4 \times 4)$ level — the clean GaAs transient at 520 °C is shown as a dashed line next to the corresponding MQW transient in Fig. 3.14. The slower recovery observed for the MQW sample must be a consequence of the floating layer of Sb which is present on the surface. On the other hand, the fact that the signal eventually reaches the same level as for clean GaAs suggests that the Sb desorbs effectively under TBAs exposure. This differs from the behaviour observed under hydrogen carrier gas only, which was discussed in section 3.3.1. In that case, the adsorbed Sb is still present after 300 s.

The initially linear time dependence of the RD signal during Sb desorption under TBAs exposure indicates a zeroth-order reaction. Semilogarithmic plots (not shown) of the RD transients at each temperature confirmed that the signal subsequently behaves exponentially, indicating that a first-order reaction becomes dominant. The time constant for the exponential part of the curves was found to be approximately 24 s, and was not dependent on temperature, indicating a non-activated process, or one with a very small activation energy. This process may be the adsorption of As to form the second layer of As dimers of the $c(4 \times 4)$ reconstruction (which is associated with the strongly negative RD signal at 2.6 eV). The slope of the linear portions of the curves, on the other hand, is temperature dependent. An Arrhenius plot of the rate of change of the RD transient is shown in Fig. 3.15. For a zeroth order reaction, the rate of change of the RD transient is proportional to the reaction rate k, but the unknown constant of proportionality does not affect the determination of the activation energy from the slope of the Arrhenius plot [23]. The points do not lie on a straight line, perhaps indicating that more than one temperature dependence regime exists. A straight line (not shown) fitted to the three highest-temperature points gives an activation energy of approximately 650 meV, although such a fit is not particularly convincing. Activation energies observed in previous work for desorption of Sb under UHV conditions [43] are higher, 1.1 eV and 2.5 eV. The presence of a floating layer of Sb on the surface appears to inhibit the reconstruction of the surface into the $c(4 \times 4)$ structure. The mechanism by which this occurs is unclear at this point, but the results presented in the next chapter show that this effect persists until the surface

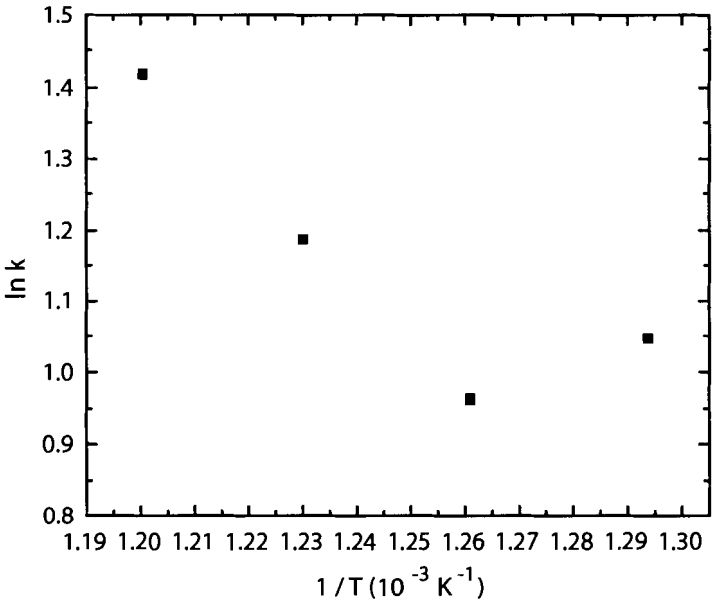

Figure 3.15: Arrhenius plot of the zeroth-order rate of change of RD transients during Sb desorption under TBAs.

Sb coverage is quite low, on the order of 0.01 ML.

Chapter 4

Structural quality of quantum wells

The issue of structural quality takes on a particular significance for quantum wells with thicknesses on the order of a monolayer. Even subtle structural imperfections can have a major effect on the electronic and optical properties of these structures. In this chapter, we will discuss the growth and characterization of MQW heterostructures containing strained, ultrathin GaSb and InAs quantum well layers, separated by GaAs barriers. There are two main issues to contend with: one is the abruptness of the quantum wells, and the other is the relief of built-up strain in the epilayer by a morphological transition from two-dimensional growth to three-dimensional island formation, which occurs when the layer exceeds a certain critical thickness.

The growth of a semiconductor quantum well requires the epitaxial deposition of the quantum well material on a dissimilar substrate, followed by epitaxial overgrowth of the quantum well layer by a capping layer of the barrier material. The growth of such embedded layers poses fundamental problems. An epitaxial film may grow via different growth modes: layer-by-layer (Frank-Van der Merwe), islanding (Volmer-Weber), or layer-by-layer growth followed by islanding (Stranski-Krastanov). The stable state of a deposited film is determined by the free energies of the surface and interface, and wetting of the underlying material can only be energetically favoured for one of the two materials [54, 55]. Thus, if the quantum well layer wets the surface (either Frank-Van der Merwe or Stranski-Krastanov growth), then immediate islanding of the capping layer is thermodynamically preferred. Kinetic factors can prevent the formation of such islands. In some material systems, islanding can be

prevented by using a sufficiently high growth rate for the capping layer [54]. Another strategy is to intentionally deposit a surfactant material on the quantum well surface before growing the barrier layer. The surfactant segregates to the surface during barrier layer growth, and lowers the surface free energy, inhibiting islanding of the film [55]. In some cases, a fraction of the atoms from the quantum well layer itself segregate to the surface, effectively acting as a surfactant. However, the partial incorporation of these atoms from the surface typically leads to a quantum well whose upper interface with the barrier material is diffuse, i.e., there is an undesirable intermediate layer with a graded composition [54, 56].

The interface abruptness in heterostructures can also be affected by exchange reactions (which were discussed in section 3.3), by the intermixing of reactants, and by bulk diffusion. In OMVPE, reactant intermixing is minimized by appropriate design of the reactor chamber and source switching system, as discussed in chapter 2. A typical procedure to avoid intermixing by diffusion in the vapour phase is to introduce a growth interruption to separate the source chemicals in the gas stream. For interfaces at which the group V element does not change, the growth interruption can be effected while continuing to stabilize the surface under a supply of the group V precursor. However, where the group V element changes at the interface, an interruption in the group V supply is required — thus, the need to separate the two group V precursors in the gas stream must be balanced against potential effects on the surface of the growth interruption, such as evaporation of the group V element. Booker *et al.* studied in detail the effects of various OMVPE switching sequences on the interface quality in InAs/GaSb heterostructures, using cross-sectional TEM and Raman spectroscopy [57]. They found that a switching sequence similar to atomic layer epitaxy (ALE), in which only one species is switched into the reactor at any one time during formation of the interface, produced the optimum results. Chaldyshev *et al.* studied the broadening by bulk diffusion of monolayer and submonolayer GaSb insertions in low-temperature-grown GaAs (LT-GaAs) [58]. They found that the diffusion of Sb in GaAs is strongly enhanced in LT-GaAs, compared with conventionally grown (stoichiometric) GaAs. For conventionally grown GaAs, however, the diffusion coefficient for interdiffusion of As and Sb is given approximately by [58, 59]

$$D_{\mathrm{As-Sb}} = 75 \exp(-4.4\mathrm{eV}/k_B T)\mathrm{cm}^2\mathrm{s}^{-1} \tag{4.1}$$

At the temperatures used for OMVPE growth in this thesis (500 °C–560 °C), the contribution of bulk diffusion to the interface broadening of GaSb/GaAs heterostructures should accordingly be negligible. Diffusive effects are not considered in the models employed in this chapter.

The accurate measurement of compositional profiles at broadened interfaces poses a difficult challenge, particularly when the broadening occurs over the scale of a few ML. A number of authors [54, 60] have reported the use of high resolution XRD rocking curves to measure interfacial broadening. These reports, however, relied on fitting the experimental rocking curves to theoretically computed simulations, making the interpretation dependent on the particular structural models employed. XRD has also been used to infer the presence of interfacial broadening indirectly, by detecting the presence of additional strain related to the intermixed layer [51]. Another indirect method to infer compositional profiles has been reported, using the PL transition energy of InAs monolayers embedded into GaAs/AlGaAs quantum wells [56, 61]. RDS measurements have been used to study InAs quantum wells in GaAs and GaAs quantum wells in InAs; the RD transients showed that In tends to segregate to the GaAs surface, but Ga does not segregate during InAs overgrowth [62, 63]. In the case of the GaSb/GaAs system, the results reported in section 3.3.4 suggested that strong segregation effects were present, but it was not possible to relate the RD signal directly to the concentration of Sb, so no compositional profile could be inferred.

XSW measurements have been used in combination with high-resolution XRD to determine the structural quality of GaAs/InAs/GaAs interfaces [64–66]; the XSW parameters are related to the atomic positions, but the uncertainty in the segregation coefficient determined from these experiments is quite large [66]. Cross-sectional STM provides a direct way to measure the composition on a monolayer-by-monolayer scale and thus construct a detailed compositional profile. It is a difficult technique, requiring cleaving of the sample in vacuum and a time-consuming search for the region of interest on the cleaved specimen—only a few research groups have the capability to perform these experiments. Using cross-sectional STM, Steinshnider *et al.* measured the graded compositional profiles in InGaSb/InAs superlattice samples grown by MBE [67]. They found that the profiles were well described by a simple one-dimensional segregation model, based on the partitioning of segregated atoms between the growing

crystal and a surface floating layer.

4.1 GaSb/GaAs quantum wells

There have been few previously published reports of GaSb quantum wells in GaAs. Chidley *et al.* [68] published a cross-sectional transmission electron microscope image, and PL spectra from layers grown by OMVPE. A more detailed study, which included characterization of MQW structures by high resolution XRD, was performed on MBE-grown layers by Ledentsov *et al.* [6, 69]. PL and calorimetric absorption spectroscopy (CAS) of the MBE-grown samples revealed a transition energy much closer to that of the bulk GaAs material than predicted by the envelope function approximation. GaSb quantum wells up to 11 Å thick were reported to be planar and coherent. Other reports on this material system include the diffusion study in LT-GaAs referred to above [58] and studies focusing on anion intermixing during MBE growth [60, 70]. A number of publications have focused on the properties of self-assembled quantum dots formed by depositing GaSb on GaAs in the Stranski-Krastanow growth mode. The critical thickness for the transition to three-dimensional (3D) growth was studied by in-situ stress measurements, and was reported to be in the range 0.7–1.0 ML for MBE growth [3], in contrast to earlier claims of much larger critical thicknesses. Published estimates of the critical thickness include 2.5 ML [71] for MBE-grown layers, and less than 2 ML [72], 2.5 ML [73], and between 3.5 and 4 ML [74], for OMVPE-grown layers.

In this work, the growth of GaSb/GaAs MQW structures was initially investigated using a "TMSb-GaAs" sequence. While the GaAs barrier layers are grown using conventional OMVPE, the quantum well step in this sequence is similar to the ALE method [62], although the temperatures employed are considerably higher than typical ALE temperatures. To form the quantum well, the GaAs surface is first exposed to the antimony precursor (TMSb), followed by a hydrogen purge and a short group III (TEGa) exposure. The advantage of this method is that the GaSb epilayer thickness is limited by the amount of Sb that can be adsorbed onto the surface, so 3D islanding does not occur. However, we found that more than half of the deposited Sb segregates to the surface and is incorporated as an impurity in the GaAs barrier layers, rather

than forming an abrupt GaSb layer. On the other hand, these structures allowed a detailed investigation of the process of Sb segregation in GaAs. These results are presented in section 4.1.2. Growth of MQW structures using a conventional OMVPE sequence, consisting of growth steps for both GaAs and GaSb, is discussed in section 4.1.3. With the conventional growth sequence, the GaSb growth time must be accurately controlled to avoid exceeding the critical thickness. A number of the samples produced using this method showed clear evidence of three-dimensional (3D) GaSb island growth. Whereas the TMSb-GaAs and conventional sequences both resulted in long-range interface grading, the abruptness of the GaAs-on-GaSb interface was significantly improved by employing a "flashoff" sequence in which the surface layer of Sb is removed prior to GaAs overgrowth. The GaSb layer is initially capped by a thin GaAs layer. The floating layer of Sb, which forms as a result of the segregation process, is then allowed to desorb under a flux of TBAs. This procedure is discussed in detail in section 4.1.4.

4.1.1 Antimony segregation

In order to quantify the effects of Sb segregation on the structural properties of MQW samples, we will make use of a simple one-dimensional segregation model [67]. The model assumes that of the initially deposited amount of Sb, a certain fraction remains in the initial position, while the remainder segregates to the surface when GaAs overgrowth starts. As growth of the GaAs barrier layer continues, the Sb is partitioned between the floating layer on the surface, and the solid GaAs layer. Each added monolayer of GaAs incorporates a fraction $1 - \sigma$ of the Sb floating layer, while the remainder, σ, is expelled to the surface. The quantity σ is known as the segregation coefficient. Clearly, the incorporation of Sb into the growing barrier layer gradually depletes the floating layer, as long as no additional Sb is added. This results in a graded impurity profile in the barrier layer. There is also the possibility of a vapour background that contributes to the impurity profile — this effect is taken into account by adding a constant source term. The amount of Sb, ξ_n, in the floating layer after the deposition of n ML of GaAs, is given by the recursion relation

$$\xi_n = \sigma[\xi_{n-1} + x_v] \tag{4.2}$$

where x_v is the constant source term representing the vapour background effect. The initial amount of Sb in the floating layer, or segregation seed, is $\xi_0 = x_{in} - x_0$. Here, x_{in} is the amount of Sb deposited initially, and x_0 is the amount incorporated in the first ML of each period, i.e. the nominal quantum well position. The mole fraction of Sb in the nth ML of the barrier layer is given by

$$x_n = (1 - \sigma)[\xi_{n-1} + x_v] \tag{4.3}$$

Substituting the expression for the floating layer (4.2) yields

$$x_n = (x_{in} - x_0)\sigma^{n-1}(1 - \sigma) + x_v(1 - \sigma^n) \tag{4.4}$$

It will be useful to calculated the total Sb incorporation in each period of the MQW structure. Clearly, both the nominal quantum well layer and the Sb incorporated in the overlying barrier layer must be taken into account to determine this amount. The total incorporated Sb per period, x_T, is therefore obtained by summing the values of x_n in the quantum well layer ($n = 0$) and the N ML making up the barrier layer:

$$x_T = x_0 + \sum_{1}^{N} x_n \tag{4.5}$$

with $x_n (n \geq 1)$ given by (4.4). Thus, one can express the total Sb incorporation per period as a function of the barrier thickness, N. This function can be fitted to the experimentally determined Sb incorporation for samples with different barrier thicknesses in order to determine x_{in}, x_0, and σ.

Fig. 4.1 shows four different Sb concentration profiles. For each profile, the total amount of Sb is equivalent to one ML of GaSb. Profile (a) is a single GaSb ML covered by pure GaAs. Profile (b) consists of a 4 ML thick layer of $GaAs_{0.75}Sb_{0.25}$, covered by pure GaAs. Profiles (c) and (d) were computed using the segregation model. In each case, 0.25 ML is assumed to remain in the nominal quantum well position, while 0.75 ML initially segregates to the surface. For curve (c), the Sb incorporation into the barrier layer is described by a segregation coefficient $\sigma = 0.75$, while for curve (d) it is given by $\sigma = 0.95$. To simplify the computation of simulated XRD rocking curves, the segregation profiles were approximated by averaging the Sb content so as to obtain seven layers with a constant Sb mole fraction.

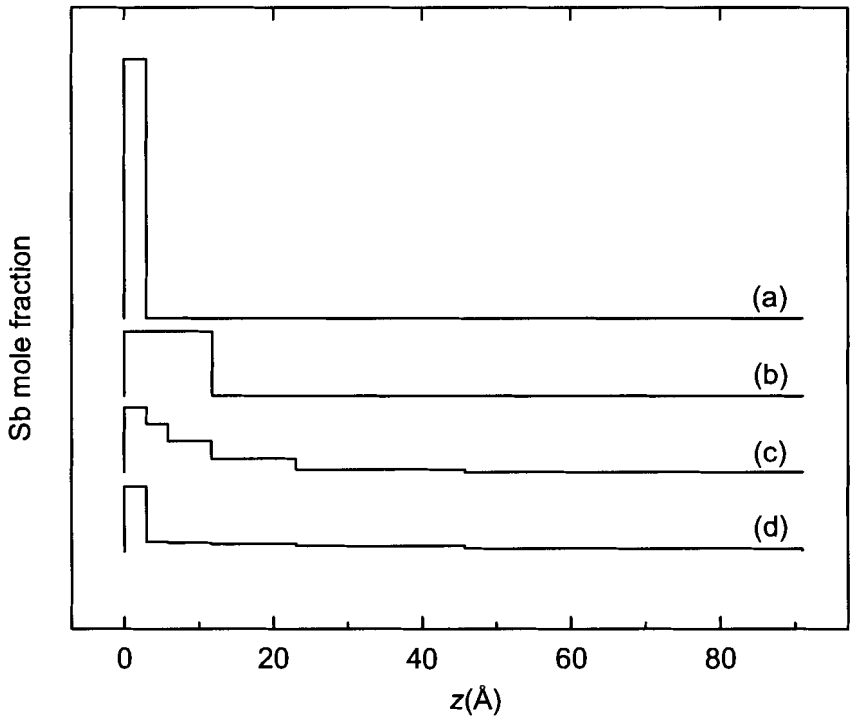

Figure 4.1: Models of the Sb concentration profile, each with a total content of 1 ML Sb per period. (a) 1 ML GaSb layer; pure GaAs barrier layer. (b) 4 ML thick $GaAs_{0.75}Sb_{0.25}$ layer; pure GaAs barrier layer. (c) Stepwise constant approximation of structure resulting from segregation with $\sigma = 0.75$ and $x_0 = 0.25$. (d) Stepwise constant approximation of structure resulting from segregation with $\sigma = 0.95$ and $x_0 = 0.25$.

The Sb concentration profiles from Fig. 4.1 were used to define four MQW layer structures with 12 periods each, and the predicted rocking curves of these structures were calculated using the RADS program. The results are shown in Fig. 4.2. The rocking curves predicted for profiles (a)–(c) are, for practical purposes, indistinguishable. For profile (d), on the other hand, the intensity of the satellite peaks decays more rapidly to either side of the substrate peak. Thus, we can expect that fitting of the experimental satellite peak intensities using dynamical diffraction simulations will only be useful in identifying very strong segregation. However, the satellite peak positions provide an accurate way to determine the total Sb incorporation per period, regardless of the detailed concentration profile.

4.1.2 The TMSb-GaAs growth sequence

The growth conditions used for the TMSb-GaAs sequence were similar to those used for the RDS study discussed in section 3.3.4. The substrate temperature was 500 °C and the precursor flows were 5.3×10^{-6} mol/min (TEGa) and 3.1×10^{-5} mol/min (TBAs, TMSb). The substrates were annealed under TBAs and a 100 nm GaAs buffer layer was grown prior to the start of the MQW sequence. The switching sequence employed for the MQW was as follows: 2 s purge (H_2 carrier gas only), 6 s TMSb, 0.5 s purge, GaAs growth for various times (with TEGa switched on 0.2 s before TBAs). This sequence was repeated twelve times in order to obtain 12× MQW samples. The RD signal was collected at 2.6 eV during growth, and the samples were characterized by cross-sectional TEM imaging and high-resolution XRD.

Fig. 4.3 shows a cross-sectional TEM image of a sample with 215 Å (76 ML) thick barrier layers. The interfaces are planar and the periodicity of the MQW is consistent throughout the structure, demonstrating the reproducibility of the growth cycle. The MQW period measured from the TEM image agrees with that calculated from the growth rate, and with XRD measurements. The upper interfaces of the quantum wells appear somewhat less abrupt than the lower interfaces; the TEM contrast, however, cannot be directly related to the Sb concentration, so no quantitative analysis of the interfacial grading was possible from the TEM image.

For each sample, the amount of incorporated Sb per period was obtained by fitting

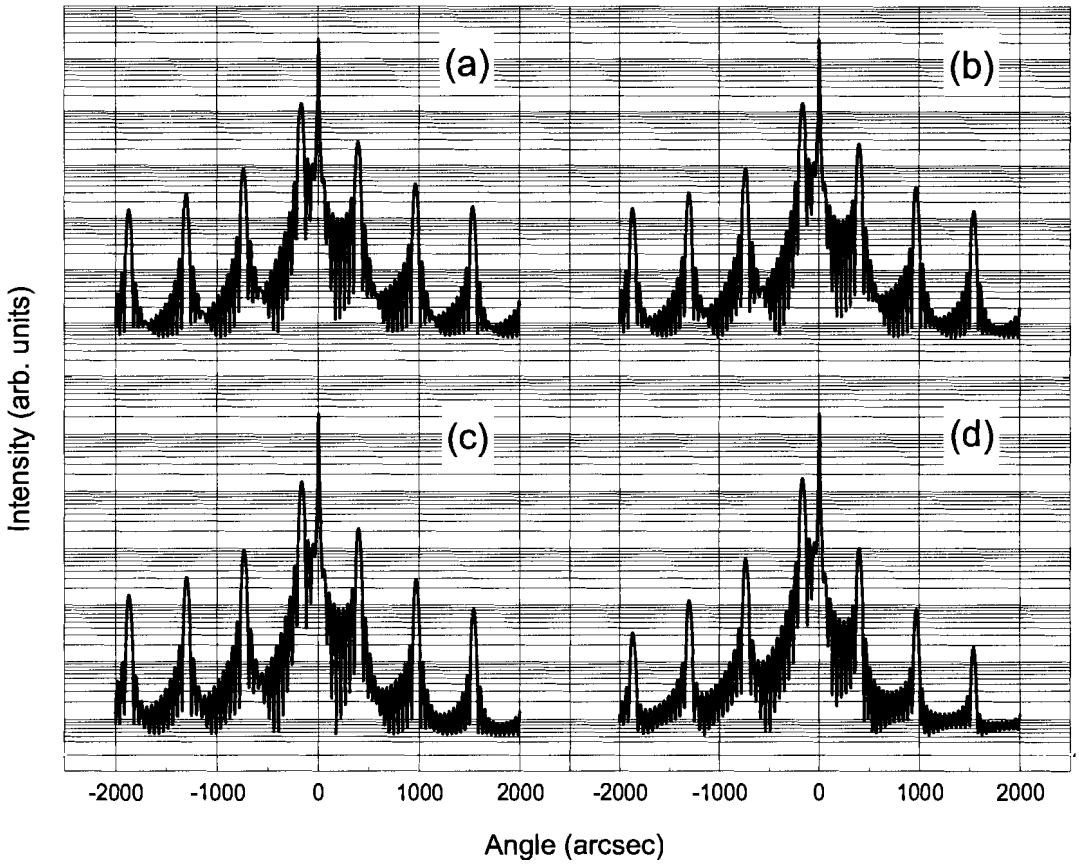

Figure 4.2: Calculated rocking curves of 12-period MQW structures, using the Sb concentration profiles shown in Fig. 4.1. Note the reduced satellite peak intensities for (d).

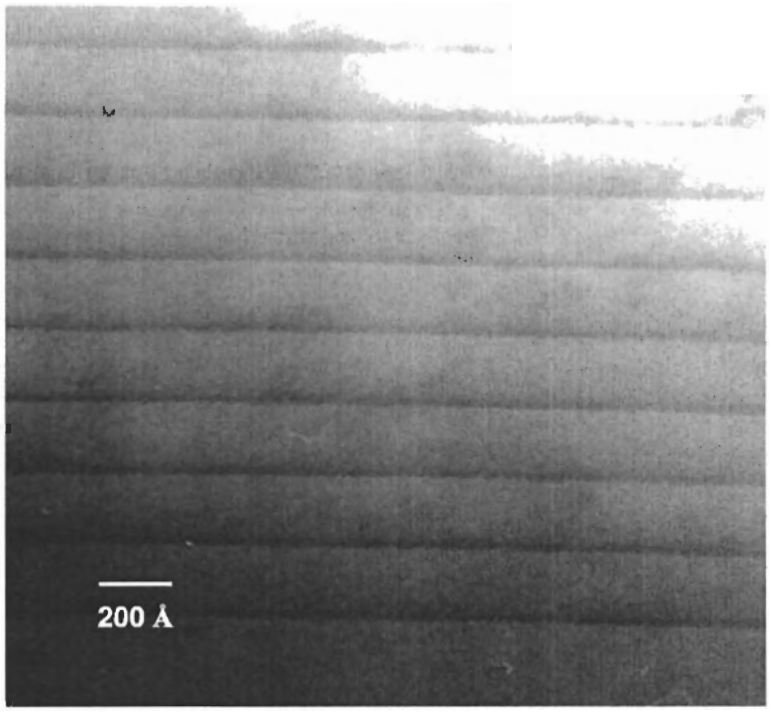

Figure 4.3: Cross section of a MQW sample, imaged by bright field TEM; $\boldsymbol{g} = (004)$

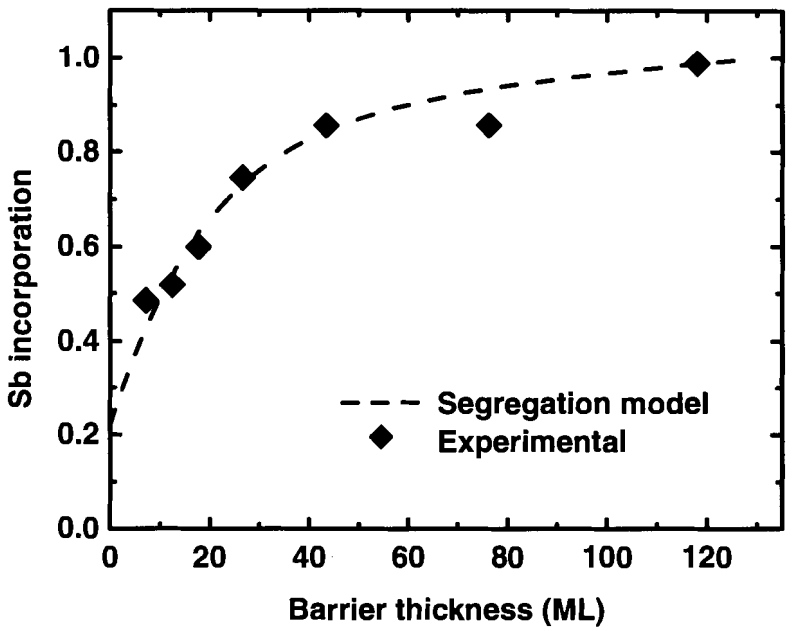

Figure 4.4: Plot of the amount of Sb incorporated per period as a function of the barrier layer thickness. The dashed lines are fits to (4.5). The unit of Sb incorporation is equivalent to one ML of GaSb per period.

the experimental XRD rocking curves using the RADS program. The resulting values are plotted as a function of the barrier layer thickness in Fig. 4.4. In order to compare the results conveniently with the curve predicted by equation 4.5, the barrier thickness is expressed as the number of GaAs MLs and the Sb incorporation is expressed as a fractional ML coverage. The calculated curve for the incorporated Sb is shown as a dashed line and is a good fit to the data, with the exception of the sample with 76 ML barriers. This discrepancy is most likely a result of imperfect reproducibility of the growth conditions from run to run. The fitting parameters used for the plotted curve are $\sigma = 0.95$, $x_v = 0.001$, $x_{in} = 0.89$, and $x_0 = 0.22$. Due to the small number of data points, there are some uncertainties in the values determined by this method. The segregation coefficient is within the range 0.93–0.97. x_0 is poorly constrained, because the XRD signal becomes weak for samples with thin barrier layers. An upper limit of 0.3 can be placed on x_0. x_v determines the asymptotic slope for large barrier

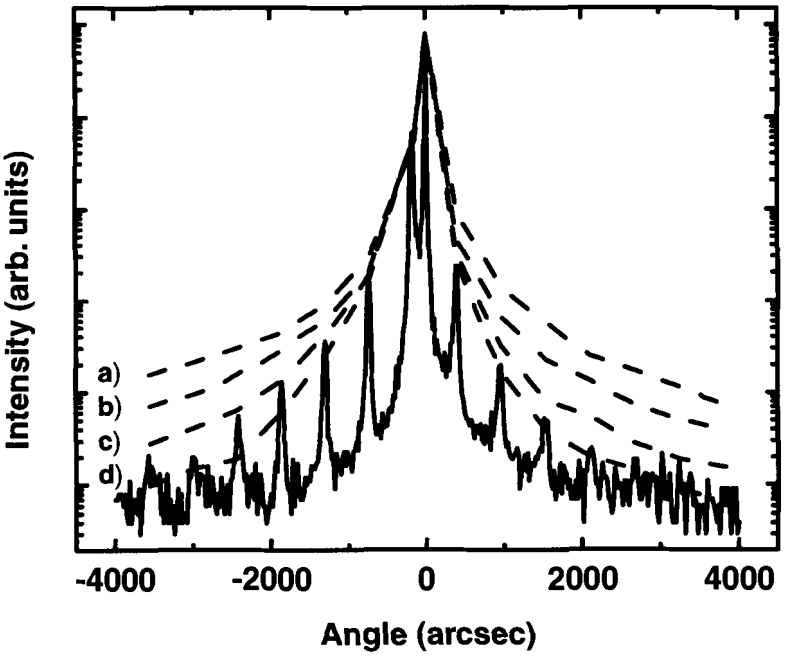

Figure 4.5: (004) XRD Rocking curve (solid line) and envelopes of the satellite peak intensities for simulated curves calculated with a graded interface model, using dynamical diffraction theory. The segregation seed $x_{in} - x_0$ is (a) 0.0, (b) 0.3, (c) 0.7, and (d) 0.95.

thicknesses, for which there are few data points, but an upper limit of 0.002 can be placed on this parameter based on the available data. The value determined for x_{in} depends to some extent on x_v, but it can be placed in the range 0.8–1.0.

The experimental rocking curve for the sample with 330 Å(117 ML) barriers is shown in Fig. 4.5 as a solid line. The dashed lines show the envelopes of the simulated satellite peak intensities for different values of the segregation seed $(x_{in} - x_0)$. The segregation coefficient σ was taken to be 0.95 for all four simulations. The zero segregation seed case (a) is equivalent to a GaSb/GaAs model with no grading. In this case, the simulated peak intensities are significantly higher than those in the experimental rocking curve. For a segregation seed of 0.3 (b), the peak intensities decrease, but they are still higher than the experimental peaks. The peak intensities

to the left of the substrate peak fit the experimental curve well for $x_{in} - x_0 = 0.7$ (c), but the satellite peaks to the right of the substrate peak are closer to curve (d), with a segregation seed equal to 0.95. The satellite peak intensities are thus consistent with long-range grading of the interfaces, with a high segregation coefficient, and only a small fraction of the total Sb (0.05–0.3) incorporated in the nominal quantum well positions. It is interesting to compare our results with those of a previous study of Sb segregation in GaInSb/InAs superlattices grown by MBE [67]. The segregation coefficients reported in that work were considerably lower, in the range 0.6–0.7. The segregation seeds ($x_{in} - x_0$ in our notation) were in the range 0.5–0.7, similar to our value. The different growth technique and conditions, as well as the different materials involved, are factors that may contribute to the difference in the segregation coefficient.

In order to study the desorption of residual Sb, the 12-period MQW samples were held under TBAs for 300 s following the completion of the final GaAs layer. Fig. 4.6 shows the RD transients at 2.6 eV during post-growth TBAs exposure, for three of the seven samples. The curves, which are similar to those discussed in section 3.3.4, show a linear region followed by a drop to the level observed for $c(4 \times 4)$ reconstructed GaAs. As the barrier thickness decreases, the linear region lasts for longer times. In order to quantify this relationship, the length of the linear region, or desorption time, is defined as the interval between the end of the MQW growth sequence and the break point where the curve first departs from the linear slope. This break point is indicated by the dashed lines in Fig. 4.6.

The increase in the desorption time with decreasing barrier thickness suggests that the Sb floating layer desorbs at a consistent rate under TBAs exposure. The samples with the thinnest barriers have the most Sb remaining as a floating layer at the end of MQW growth, since less of the initially deposited Sb is incorporated into the final barrier layer in these samples. Keeping in mind the uncertainties in the fitting parameters, the segregation model allows an estimate of the amount of Sb remaining in the floating layer as a function of the barrier thickness. This is given by

$$\xi_N = \sigma^N (x_{in} - x_0) + \frac{\sigma x_v (1 - \sigma^N)}{1 - \sigma} \tag{4.6}$$

where N is, again, the barrier thickness in ML. In Fig. 4.7, the desorption time is

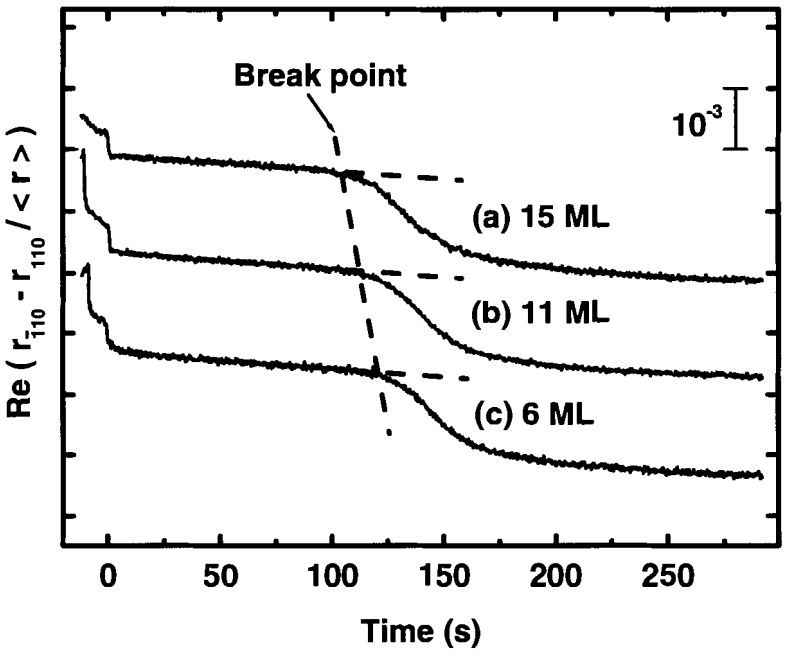

Figure 4.6: RD time dependence during TBAs exposure following growth of 12× MQW structures with (a) 15 ML barriers (b) 11 ML barriers (c) 6 ML barriers. The dashed lines show the break point used to define the length of the plateau region.

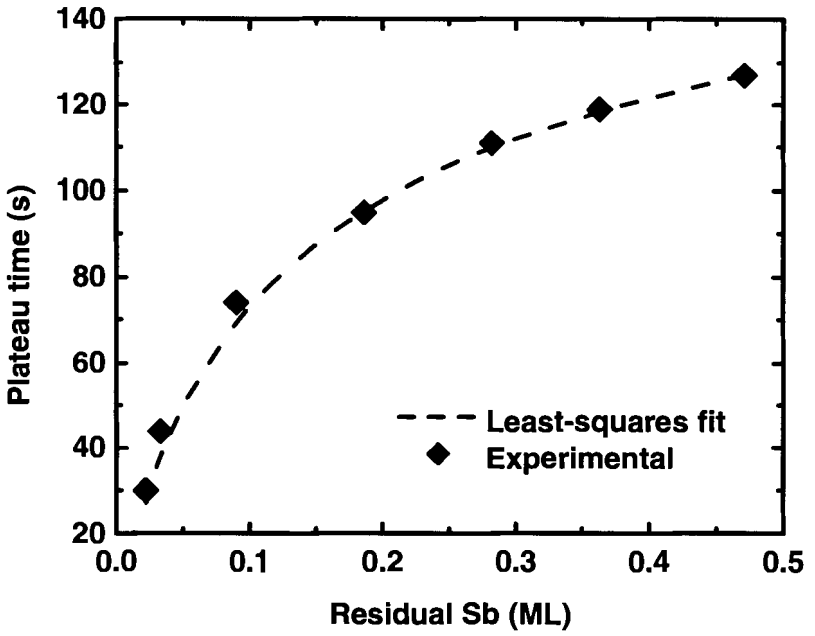

Figure 4.7: Plot of the desorption time, calculated using the segregation model, as a function of the amount of Sb in the floating layer at the end of barrier growth. The dashed line is a least-squares fit to a logarithmic function

plotted as a function of the estimated amount of Sb remaining in the floating layer at the end of barrier growth; this floating layer coverage is calculated from the barrier thickness using Eq. (4.6). The data are consistent with a floating layer which desorbs exponentially with time when exposed to a constant TBAs flow, if one assumes that the end of the plateau corresponds to a threshold Sb concentration at which the $c(4 \times 4)$ reconstruction starts to reappear. This can be expressed in the form

$$t_P = \tau \ln(\xi_N/\xi_{th}) \tag{4.7}$$

where t_P is the desorption time, ξ_N is the amount of Sb at the end of barrier growth, ξ_{th} is the threshold value and τ is a time constant. A least-squares fit to this logarithmic function (shown as a dashed line in Fig. 4.7) yields a time constant of 33 s and a threshold value $\xi_{th} = 0.01$, although it should be noted that the exact values are dependent on the parameters used to describe the segregation profile; these parameters

are, as discussed above, subject to some uncertainty. To obtain a good fit to the RDS desorption time data, it is necessary to include a nonzero background incorporation term x_v in Eq. (4.6). The best fit is obtained for $x_v = 0.001$.

4.1.3 The conventional growth sequence

Structures grown with a conventional OMVPE growth sequence were also analyzed, using the techniques introduced in the previous section. These samples were grown at 520 °C with precursor flows of 5.24×10^{-6} mol/min (TEGa), 3.08×10^{-5} mol/min (TMSb) and 6.15×10^{-5} mol/min (TBAs). The substrates were annealed under TBAs and a GaAs buffer layer grown prior to the start of the MQW sequence. The switching sequence employed was as follows: 2 s purge (H_2); 3 s TMSb; GaSb for various times up to 2 s; GaAs barrier layer of varying thickness, with TEGa flow started 0.5 s before TBAs. The sequence was repeated in order to obtain 12× MQW samples, which were characterized by cross-sectional TEM imaging and high-resolution XRD. A series of samples with different barrier thicknesses was grown with a GaSb deposition time of 2 s, to study the trend in the Sb incorporation; these samples were found to contain GaSb islands. Based on the measured GaAs growth rate and assuming that the growth rate in ML/s depends only on the TEGa flow rate, the nominal amount of GaSb deposited is ~ 2 ML. A few samples were also grown with a smaller amount of GaSb deposition, up to ~ 1 ML, and in these samples the critical thickness for island formation was not exceeded (see Sect. 5.5).

The cross-sectional bright-field TEM image in Fig. 4.8 was obtained in the (004) diffraction condition for a sample with 2 s GaSb deposition time and 173 Å(61 ML) barrier layers. The darker GaSb layers consist of continuous, planar wetting layers and thicker 3D islands. The islands are rather indistinct, which suggests that there is considerable intermixing of GaAs and GaSb within the islands. Fig. 4.9 shows an (004) rocking curve of the same sample. The simulated curve was calculated based on 0.86 ML of GaSb per period. This coverage corresponds to the amount of Sb in the wetting layers; it has been established in previous work that the wetting layers are responsible for the strain which results in the rocking curve pattern [75, 76]. No signal attributable to the 3D islands is observed, because the volume of the islands is small compared with

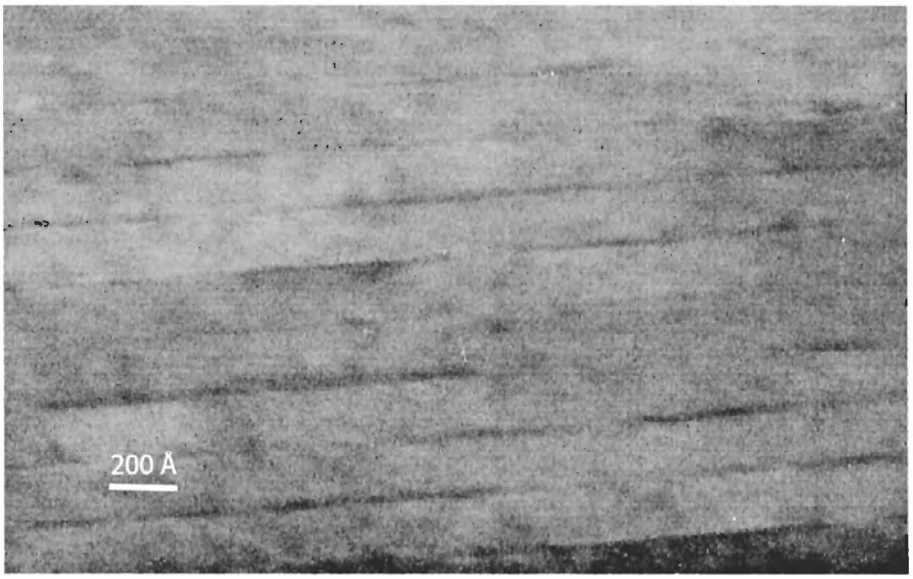

Figure 4.8: Cross-sectional TEM image of a MQW structure grown with the conventional growth sequence, showing 3D islands (thicker dark areas).

the GaAs matrix (note: this is also true of the planar wetting layers; the scattering of x-rays takes place primarily within the GaAs layers. The relative displacement of the lattice of the GaAs layers separated by strained wetting layers is what gives rise to the interference that produces the observed x-ray diffraction pattern). The experimental satellite peak intensities are closer to the ideal GaSb/GaAs simulation than in the case of the samples grown with the TMSb-GaAs sequence (see Fig. 4.5). This suggests that the samples grown with the conventional OMVPE sequence have a more abrupt GaAs-on-GaSb interface.

The interfacial grading was quantified using the series of samples with 2 s GaSb deposition and different barrier thicknesses. Fig. 4.10 shows the experimental values of the Sb incorporation, obtained by fitting the XRD rocking curves for four different values of the barrier thickness. The curve is calculated using (4.5), with $\sigma = 0.95$, $x_v = 0.001$, $x_{in} = 0.82$ and $x_0 = 0.52$. Due to the small number of data points, the first two parameters were assumed to be the same as in the case of the TMSb-GaAs sequence, rather than fitting them independently. A reasonable fit to the data is obtained in this way. The initially deposited amount, x_{in}, is close to the

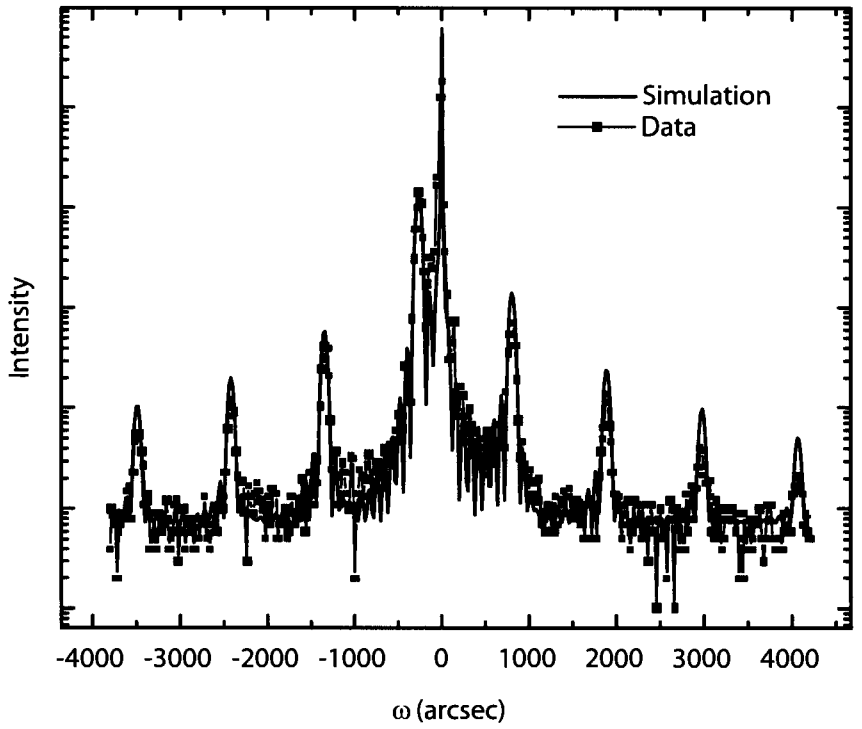

Figure 4.9: Measured and simulated (004) rocking curves of a MQW grown with the conventional growth sequence.

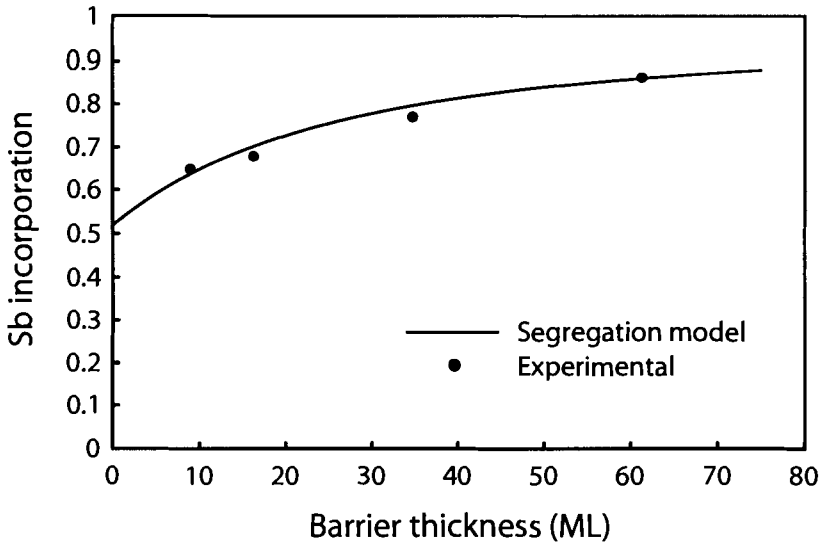

Figure 4.10: Sb incorporation as a function of barrier thickness, for MQW structures grown with the conventional growth sequence.

value observed for the TMSb-GaAs samples (0.89). In the samples grown with the conventional sequence, the total amount of GaSb deposited is higher, but x_{in} does not account for the portion which is incorporated as islands, since this parameter is calculated based on the strain measured by the XRD rocking curves; this strain arises primarily from the planar wetting layers [75, 76]. The amount incorporated in the nominal quantum well position, x_0, appears to be higher for the conventional growth samples than for the TMSb-GaAs samples (0.52 as opposed to 0.22), although the uncertainty in this parameter is considerable. It is worth noting that even though the critical thickness was exceeded, only about half a monolayer is incorporated in the nominal quantum well position. It appears, therefore, that obtaining a full monolayer coverage is not possible by the conventional growth method, at least under the growth conditions used. Samples grown at four temperatures between 500 °C and 560 °C, with GaSb deposition below the critical thickness, showed only small changes in the Sb incorporation as a function of temperature.

4.1.4 The flashoff growth sequence

The study of Sb desorption (described in section 3.3.4) led to a proposal to grow GaSb quantum well structures with a Sb desorption step after each quantum well, in order to improve the interface abruptness. The concept is similar to the flashoff procedure described by Brandt *et al.* [54] for InAs/GaAs heterointerfaces grown by MBE. In their work, the InAs was deposited at 420 °C and covered by a thin (3 ML) GaAs cap at the same temperature. The samples were then heated to 540 °C to allow the surface layer of In to desorb before continuing GaAs growth; the procedure was shown to result in very abrupt interfaces. Kaspi and Evans [77] proposed a chemical flashoff, in which Sb desorbs under an As_2 flux, to improve the abruptness of the GaAs-on-GaAsSb interface. In this thesis, the flashoff concept is adapted to OMVPE using a sequence in which the surface Sb layer desorbs under a TBAs flux.

For samples grown using the flashoff sequence, a buffer layer of 1000 Å GaAs was first grown at 560 °C. The temperature was then reduced to 500 °C, and an additional buffer layer of 200 Å GaAs was grown; the MQW portion of the growth sequence followed, at a constant temperature of 500 °C. After a 2 s purge under hydrogen, the GaSb quantum well step consisted of 6 s TMSb exposure followed by GaSb growth (for various times). The GaSb layer deposition was immediately followed by growth of a 4 ML GaAs capping layer. The sample was then held under TBAs for 200 s to desorb the Sb floating layer. After the desorption step, GaAs was grown to complete the barrier layer. The sequence was repeated six times to obtain 6× MQW samples; the smaller number of periods compared to samples discussed in previous sections was chosen because of the long time required to complete each cycle with the flashoff step. The precursor flows were 5.24×10^{-6} mol/min for TEGa and 3.08×10^{-5} mol/min for TMSb. For TBAs, a flow of 4.59×10^{-5} mol/min was used for the desorption step and barrier layer growth and a lower flow of 3.06×10^{-5} mol/min was used for the 4 ML capping layer in an attempt to minimize As-for-Sb exchange at the GaSb surface.

The RD signal was monitored during the growth sequences to verify that the Sb is completely desorbed; the 2.6 eV transient is shown in Fig. 4.11. The strong upward spikes correspond to the GaSb quantum well growth steps, beginning with the 6 s TMSb exposure. During the 200 s TBAs exposures, the RD transient shows the

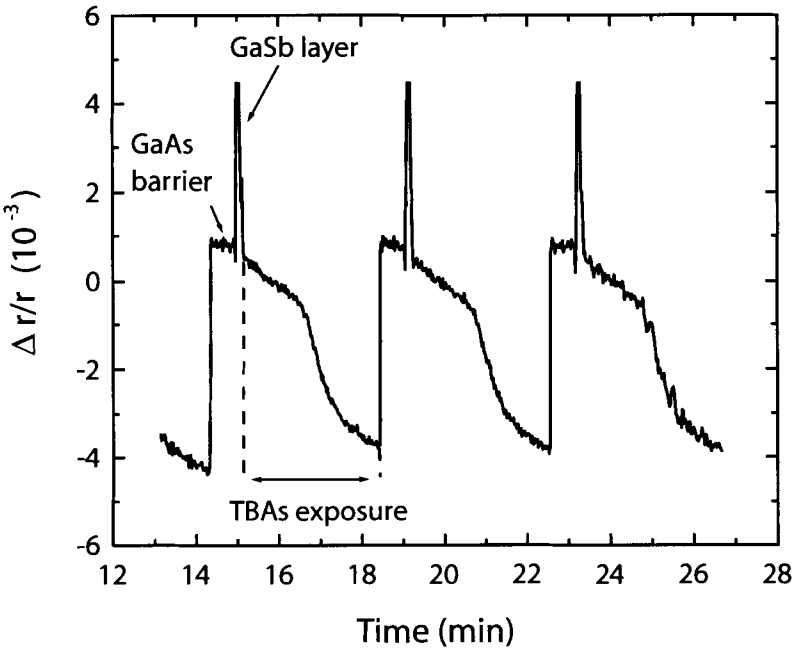

Figure 4.11: RD transients at 2.6 eV, showing the flashoff step under TBAs.

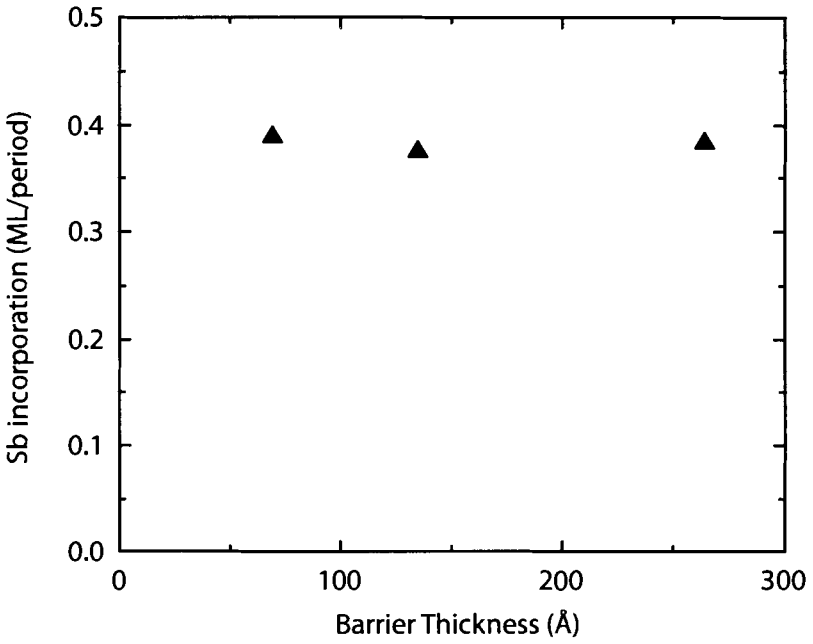

Figure 4.12: Sb incorporation for three samples with different barrier thicknesses

expected behaviour (see section 3.3.4); a linear region is followed by the recovery to the $c(4 \times 4)$ surface reconstruction. The barrier growth steps are characterized by a flat RD time response at the level corresponding to growth of Sb-free GaAs at the same temperature and V:III ratio.

To further verify that the Sb desorption procedure is successful in reducing incorporation of Sb into the barrier layers, three samples with different barrier thicknesses were grown. Fig. 4.12 shows the net Sb incorporation per period determined from the XRD rocking curves for these three samples. The Sb incorporation does not show any increasing trend as the barrier thickness is increased, in contrast to the trend observed in section 4.1.1. This implies that at least beyond the lowest thickness investigated, 70 Å, Sb incorporation in the barrier layers is negligible. Furthermore, based on the observation that a TBAs exposure creates a GaAs layer at the surface of GaAsSb [53], it is reasonable to expect that some of the Sb originally present in the capping layer is removed during the purge step as well. This would result in the region of

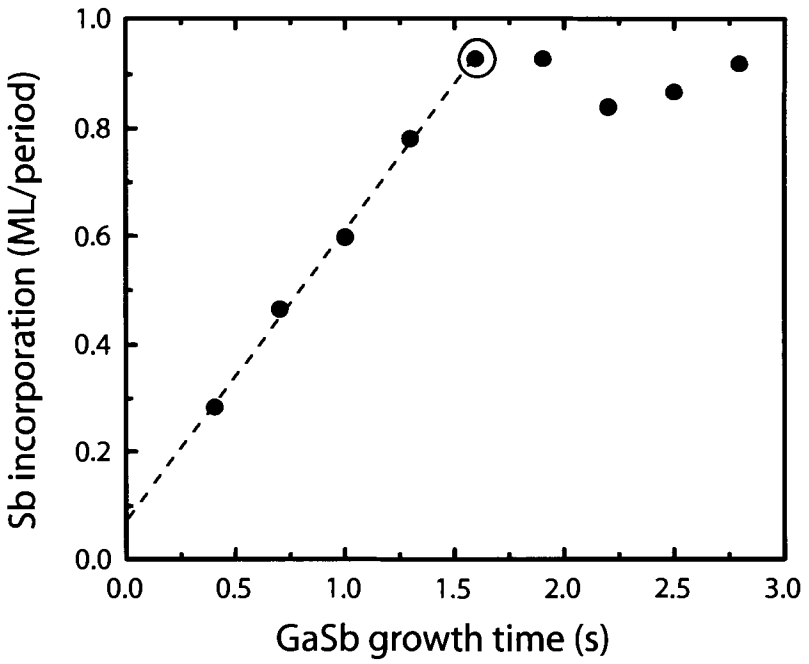

Figure 4.13: Sb incorporation as a function of growth time.

impure GaAs being even thinner than the cap layer thickness. If the segregation seed is assumed to be comparable to those observed in section 4.1.1, the segregation model predicts that the amount of Sb incorporated in the 4 ML GaAs capping layer should be less than 0.1 ML. However, it was not possible to confirm this experimentally.

Fig. 4.13 shows the apparent Sb incorporation (i.e., not including any Sb which might be incorporated as 3D islands) as a function of the GaSb growth time. The Sb incorporation was calculated by fitting the XRD rocking curves using dynamical diffraction theory; Fig. 4.14 shows the measured and simulated rocking curves for the sample which is circled in Fig. 4.13. The simulated curve (dashed line) was calculated assuming a MQW structure consisting of GaSb quantum wells and pure GaAs barrier layers. The experimental satellite peak intensities match those of the simulated curves for all samples in the study. This is further evidence of the improved abruptness of the GaSb quantum well layers in these samples. The Sb incorporation shows a nearly linear increase with growth time up to 1.6 s, which is consistent with the formation

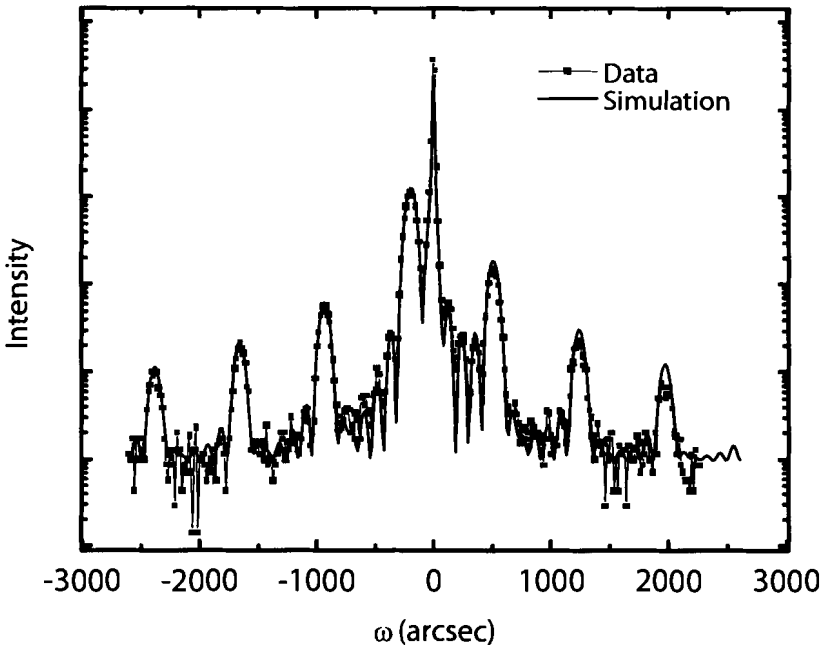

Figure 4.14: Measured and simulated (004) rocking curves of a GaSb/GaAs MQW grown with the flashoff sequence.

of a coherently strained, planar layer. The slope of the linear increase corresponds to a growth rate of 0.54 ML/s.

For growth times greater than 1.6 s, no further increase occurs in the average MQW strain measured by XRD, and in fact the samples with 2.2 s and 2.5 s GaSb growth time show a slightly lower strain. The most likely explanation is that the end of the linear increase marks the transition to 3D growth; in that case, the additional GaSb would be incorporated within 3D islands, which do not contribute to the measured strain. Previous reports on multilayer quantum dot stacks [75, 76] indicate that the strain measured by XRD rocking curves arises primarily from the planar wetting layers. The slightly lower values of the apparent Sb incorporation for 2.2 s and 2.5 s growth time may be a result of mass transfer from the wetting layers to the 3D islands during growth. From our results, the critical thickness for the transition from two-dimensional (2D) to 3D growth is approximately one monolayer. A number of

authors have previously reported considerably larger values of the critical thickness for GaSb layers on GaAs. Although the critical thickness may vary depending on growth conditions, the higher estimates of its value were based on either the nominal amount of deposited GaSb [71, 73, 74, 78–82], or the total Sb incorporation measured by XRD in multilayer samples [6]. The results reported in section 4.1.2 indicated that a considerable amount, around 0.75 ML, of the deposited Sb segregates to the surface when a GaAs capping layer is grown. It is likely that that much of this excess Sb is present as a physisorbed adsorbate layer, rather than being chemically bonded to form a GaSb epilayer. In situ stress measurements [3], which are sensitive to the actual epilayer thickness, found critical thicknesses in the range 0.7–1.0 ML for both GaSb and InAs on GaAs, which agrees with our observation.

A number of samples with a single GaSb surface layer were grown using the same GaSb growth conditions as the samples grown with the flashoff sequence. Fig. 4.15 (a) shows the surface topography of the samples with a single GaSb layer grown for 0.4 s, 0.7 s, and 1.9 s. No 3D features are observed for the 0.4 s sample, whereas for 0.7 s and 1.9 s, GaSb dots are formed. This apparent inconsistency with the critical thickness observed for the MQW samples can be explained by assuming that for samples with small GaSb coverages, the dot nucleation and growth occurs as the sample cools down. Quantum dot growth by dewetting, during cooldown, has been observed recently for InAs dots on GaAs [83]. A cross sectional TEM image (not shown) of the sample with GaSb grown for 1.3 s showed no evidence of 3D growth, whereas the planar wetting layers were clearly visible. It is worth considering the possibility that the GaSb dots are altered during the TBAs exposure. An As-for-Sb exchange process could result in dots with a more As-rich composition and redistribution of the material on the surface (see Sect. 4.1.5). If nucleation of the GaAs capping layer is inhibited on top of the GaSb dots, such an exchange might alter the dots significantly while preserving the buried wetting layer. The presence or absence of 3D dots in these samples is discussed further in Sect. 5.5 where photoluminescence results are reported. The effects of growing capping layers on GaSb dots need further investigation before definitive conclusions can be drawn.

From the dot volume measured by AFM, a rough estimate of the amount of GaSb contained within the dots is obtained. It is equivalent to an average thickness of

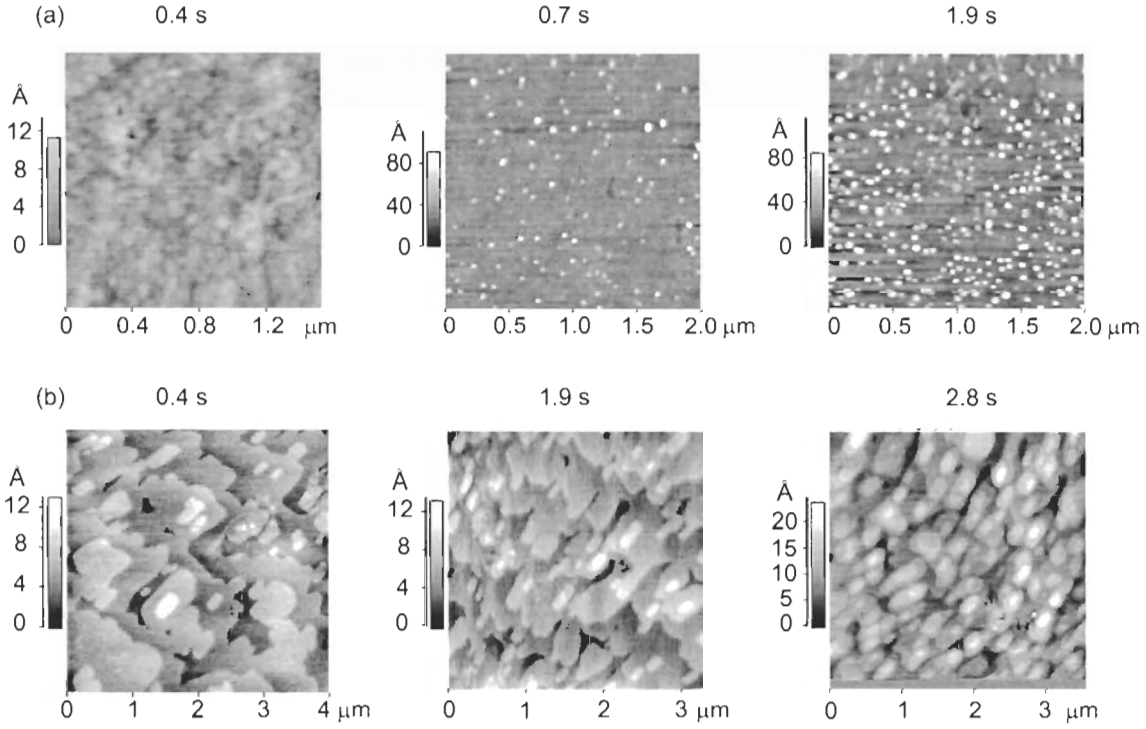

Figure 4.15: (a) AFM images of single uncapped GaSb layer samples; (b) AFM images of the surface of MQW samples. The GaSb growth time is indicated above each image.

0.3 ML for the sample with 0.7 s GaSb growth, and 1.1 ML for the 1.9 s sample. The inferred growth rate of 0.6–0.7 ML/s agrees to a first approximation with the growth rate of 0.54 ML/s which was obtained for the wetting layers, as discussed above. A slightly higher growth rate for the dots is consistent with some mass transfer from the wetting layers into the dots.

In Fig. 4.15 (b), AFM images of the MQW samples are shown. The topmost GaSb layer in these samples is covered by 200 Å GaAs. On the GaAs surface monolayer-high steps are evident. The RMS roughness is constant, with a value of 1.6 Å, for samples with GaSb growth times ranging from 0.4 s to 1.9 s. For longer GaSb growth times, the monolayer steps become more closely spaced, with the RMS roughness increasing to 3.4 Å for 2.8 s GaSb growth. The XRD rocking curves do not appear to be affected by the roughening, which is unsurprising considering that the surface has relatively large flat terraces for even the longest growth time studied, 2.8 s. The roughening of the GaAs surface is expected for structures containing 3D islands. This would be consistent with the proposal that dots are formed on samples with GaSb growth times longer than 1.6 s, and that these dots are altered into a more As-rich composition during the purge under TBAs.

4.1.5 Effect of TBAs on GaSb islands

In the previous section, it was proposed that exposure to TBAs during the flashoff sequence could result in significant alteration of the GaSb 3D islands, but the data from the flashoff samples presented only limited evidence in support of this proposed mechanism. An experiment was performed involving two samples with GaSb islands on the surface, and the results of this experiment show that significant morphological change of the islands can occur under TBAs exposure. The samples were grown at 520 °C. For the GaSb growth step lasting 8 s, a (TEGa) flow of 2.79×10^{-6} mol/min and a (TMSb) flow of 1.23×10^{-5} mol/min were used. The first sample was cooled to room temperature under hydrogen immediately following GaSb growth, whereas the second sample was held under a flow of TBAs for 300 s after the GaSb growth step, then cooled to room temperature. AFM images of the two samples are shown in Fig. 4.16. The islands on the sample cooled immediately to room temperature have an average

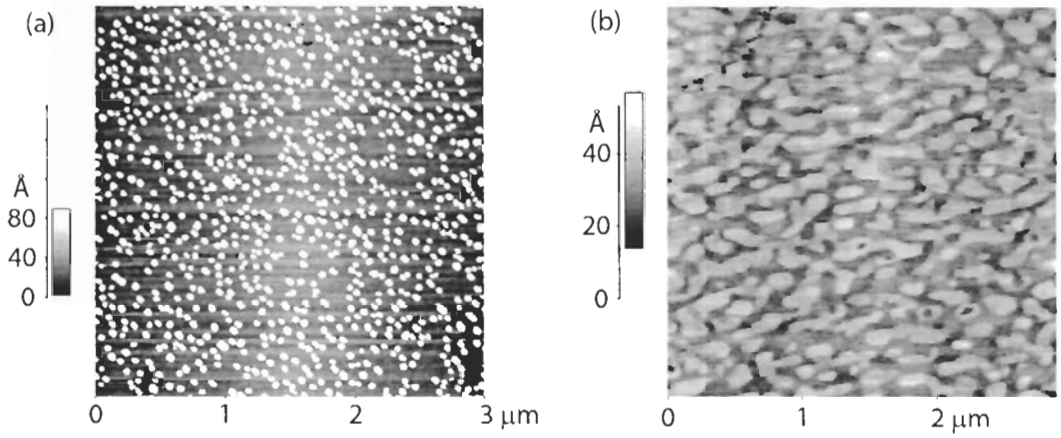

Figure 4.16: (a) AFM image of GaSb islands cooled to room temperature immediately after growth; (b) AFM image of GaSb islands grown under identical conditions and held under TBAs for 300 s before cooling.

height of approximately 100 Å, whereas the sample exposed to a long TBAs purge has a morphology consisting of irregularly shaped, flat-topped mesas with a nearly uniform height of around 10 Å. The composition of the surface layer in the TBAs-exposed sample could not be verified, but the observed morphology would probably not be stable if the mesas consisted of pure GaSb, due to the large lattice mismatch of GaSb on GaAs. This suggests that significant As-for-Sb exchange occurred during the TBAs exposure, resulting in mesas with a more As-rich composition.

4.2 InAs/GaAs quantum wells

Quantum well structures consisting of ultrathin layers of InAs in a GaAs matrix have been fabricated by OMVPE [63, 66, 84] and the related techniques of ALE [62, 65, 85] and flow rate modulation epitaxy (FME) [86]. This type of structure has also been fabricated by MBE [54, 87] and its variant, migration enhanced epitaxy (MEE) [88, 89]. These techniques are capable, in principle, of producing heterostructures with atomically abrupt interfaces. The abruptness of the structures can, however, be affected by the particular growth conditions used and the sequence in which source

materials are introduced. Indium has a tendency to segregate upward when GaAs is grown over the InAs layer [62, 90]. This has been shown to result in a graded interface above the InAs layer [56]. The structural quality of OMVPE-grown ultrathin InAs monolayers has been studied in detail in previous works [63, 66]; the purpose of including the InAs/GaAs system in this thesis is to provide a direct comparison with the GaSb/GaAs system, using the same experimental techniques.

A series of InAs/GaAs MQW samples with different barrier thicknesses was produced using a conventional OMVPE sequence. The samples were grown at 550 °C with precursor flows of 7.86×10^{-6} mol/min (TEGa), 1.98×10^{-6} mol/min (TMIn), and 1.98×10^{-4} mol/min (TBAs). The substrates were annealed under TBAs and a GaAs buffer layer grown prior to the start of the MQW sequence. The switching sequence employed was as follows: 20 s interrupt under TBAs; 3 s InAs growth; 20 s interrupt under TBAs; GaAs barrier layer of varying thickness. The sequence was repeated in order to obtain 12× MQW samples. The samples were characterized by high-resolution XRD; Fig. 4.17 shows an (004) rocking curve of the sample with the thickest barriers. The simulated curve was calculated based on a pure InAs/GaAs model with 0.7 ML InAs coverage per period and 32 ML GaAs barrier layers. The experimental satellite peak intensities are close to the ideal values on the left side of the substrate peak, although they are slightly lower on the right side. As was discussed for the case of Sb segregation in section 4.1.1, long range segregation of In can be excluded based on the strength of the satellite peaks. To obtain a more detailed picture of the compositional profile, the incorporation of In as a function of the barrier thickness was investigated.

Fig. 4.18 shows the experimental values of the In incorporation obtained by fitting the XRD rocking curves for different values of the barrier thickness between 4 ML and 32 ML; no increasing trend is evident in the In incorporation. This implies that essentially all of the In floating layer arising from surface segregation is incorporated within the first four ML of GaAs overgrowth. The curves were calculated using the segregation model introduced in section 4.1.1. They correspond to two possible sets of segregation parameters that could give rise to the observed data: curve (a) was computed using $\sigma = 0.2, x_0 = 0.21$, while curve (b) was computed using $\sigma = 0.4, x_0 = 0.41$. For both curves, the initial InAs coverage x_{in} is 0.72 and the background

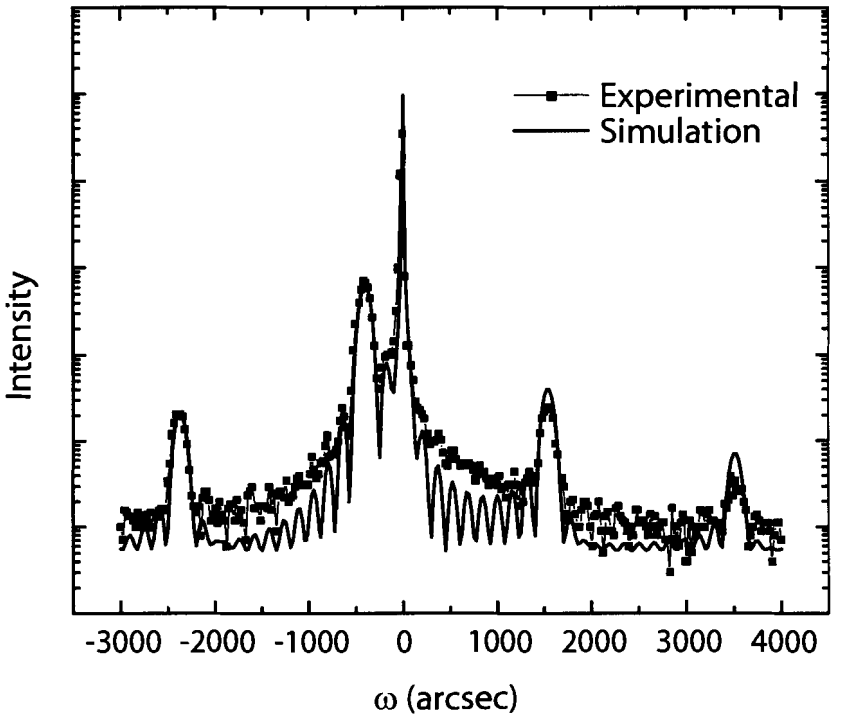

Figure 4.17: (004) XRD Rocking curve of a 12× InAs/GaAs MQW structure. The simulated curve is calculated assuming a pure InAs/GaAs model with 0.7 ML InAs coverage per period.

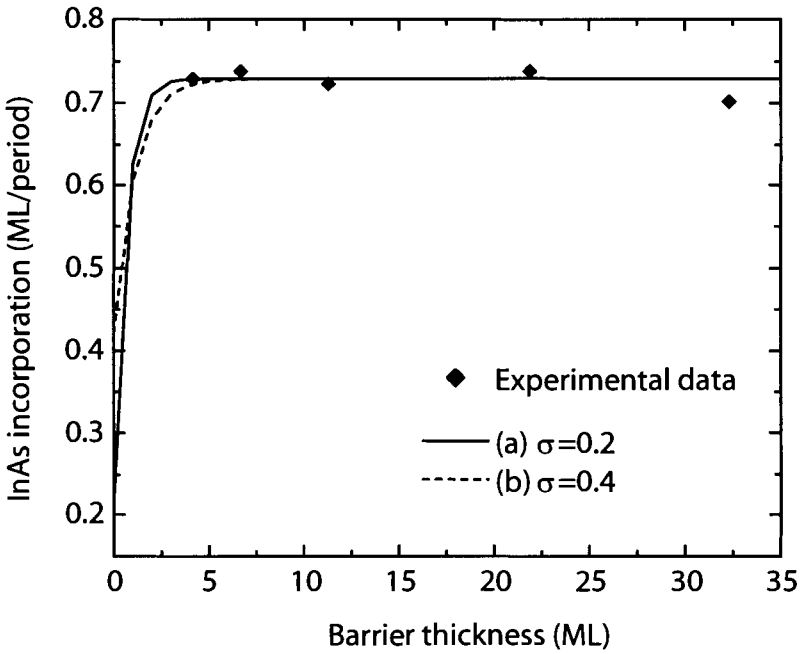

Figure 4.18: Indium incorporation as a function of barrier thickness. The curves are calculated using the one-dimensional segregation model, with 0.72 ML initial InAs deposition and (a) $\sigma = 0.2, x_0 = 0.21$; (b) $\sigma = 0.4, x_0 = 0.41$.

incorporation x_v is assumed to be zero. Evidently, it is not possible to determine the segregation parameters by fitting the available data. The nearly constant In incorporation in the range 4–32 ML is, however, indicative of much shorter range In segregation than that observed for Sb in GaAs. Previously reported measurements using the XSW technique [64, 66] determined that the In segregation coefficient in GaAs is in the range 0.2–0.3, which is consistent with the data reported in this work.

Chapter 5

Electronic states and optical properties

Ultrathin quantum wells in highly strained material systems have been predicted to exhibit novel properties, most notably a strong enhancement of the oscillator strength [91]. This has led to considerable interest in characterizing the electronic and optical properties of these structures. For type-I InAs monolayers in GaAs, several authors have reported efficient excitonic luminescence [92–94], and extremely narrow luminescence line widths have been observed from submonolayer wells in the same material system [87, 95, 96]. InAs monolayers were also reported to support stimulated emission [97], and efficient lasing was demonstrated from both single monolayers [98] and short period InAs/GaAs superlattices [99]. Relatively little has been reported on ultrathin type-II quantum wells. Ledentsov *et al.* reported PL and CAS experiments on GaSb/GaAs ultrathin quantum wells. Their results showed that a strong radiative transition occurs in these structures. The transition was attributed to the partial spatial overlap of the hole and electron wave functions, these being separately localized in the quantum well and barrier layers, respectively [6].

The electronic and optical properties of quantum wells can be strongly influenced by the degree of abruptness of the interfaces. There have been numerous reports of intermixing-induced interfacial layers resulting in a shift of the PL peak energy [100–103]. PL has also proved useful in studying transitions at type-II interfaces, which are particularly strongly dependent on the abruptness of the interface, since

these transitions occur between electrons and holes localized on opposite sides of the interface [104]. The effects of intermixing can be expected to be especially noticeable for ultrathin quantum wells, since such quantum wells can be considerably broadened by the intermixing process, as detailed in the previous two chapters.

The envelope function approximation (EFA) has become a widely used method to describe the band structure of semiconductor heterostructures, including quantum wells, due to the relative simplicity of the calculations involved [105]. The applicability of calculations based on the EFA to monolayer-scale films has been questioned on the grounds that it is a macroscopic model which averages the electron potential over the unit cell [91, 106]. However, for InAs monolayers in GaAs, the heavy and light hole excitonic transition energies predicted by EFA calculations are in good agreement both with experiments [96, 107–111] and with the energies predicted by tight binding calculations [106, 108]. Similarly, for both the type-I InAs/InP system [112, 113] and the type-II GaAs/InP system [114, 115], in which planar quantum wells up to a few monolayers thick can be grown, the dependence of transition energies on quantum well thickness has been found to agree with EFA predictions. Theoretical work by Burt [116–118] provides some insight into why the EFA succeeds in producing accurate predictions for heterostructures with abrupt boundaries, including those with layer thicknesses as thin as a monolayer. Thus, it is interesting to compare the PL transition energies observed for the samples in the present study to a simple EFA model.

The chapter is organized as follows: Sect. 5.1 introduces the EFA which allows the band structure approach to be extended to a crystalline solid in the presence of a perturbing potential. The calculation of band offsets including the effects of strain is presented in Sect. 5.2. The envelope function approximation is applied to quantum well heterostructures to obtain the quantized energy levels and the corresponding wave functions, in Sect. 5.3; the optical transitions between these energy levels are discussed in Sect. 5.4. Finally, the results of low-temperature PL measurements are presented and compared to the EFA predictions in Sect. 5.5.

5.1 The envelope function approximation

The EFA starts from the one-electron picture, in which the electronic states of the crystal are approximated by single particle states. In the presence of a perturbing potential $V_p(\mathbf{r})$, we can write the Schrödinger equation for an electron in the solid:

$$\{H_0 + V_p(\mathbf{r})\}\,\Psi(\mathbf{r}) = E\Psi(\mathbf{r}) \tag{5.1}$$

where H_0 is the hamiltonian of the unperturbed crystal

$$H_0 = \frac{-\hbar^2\nabla^2}{2m_0} + V_c(\mathbf{r}) \tag{5.2}$$

with $V_c(\mathbf{r})$ being the periodic crystal potential and m_0 the electron mass. The solutions of (5.1) may be expanded in terms of Bloch functions $\psi_{n\mathbf{k}}(\mathbf{r}) = u_{n\mathbf{k}}(\mathbf{r})e^{i\mathbf{k}\cdot\mathbf{r}}$, which are the eigenfunctions of the unperturbed crystal hamiltonian H_0:

$$\Psi(\mathbf{r}) = \sum_{n,\mathbf{k}} a_{n\mathbf{k}} u_{n\mathbf{k}}(\mathbf{r}) e^{i\mathbf{k}\cdot\mathbf{r}} \tag{5.3}$$

The Bloch functions are represented in the reduced-zone scheme, in which $\mathbf{k}$ is restricted to the first Brillouin zone and n is an index indicating the band. In the EFA, the lattice-periodic functions $u_{n\mathbf{k}}(\mathbf{r})$ are approximated by the zone-centre functions $u_{n\mathbf{0}}(\mathbf{r})$. The wave function expansion can then be written as

$$\Psi(\mathbf{r}) \approx \sum_{n,\mathbf{k}} a_{n\mathbf{k}} \phi_{n\mathbf{k}}(\mathbf{r}) \tag{5.4}$$

where $\phi_{n\mathbf{k}}(\mathbf{r}) = u_{n\mathbf{0}}(\mathbf{r})e^{i\mathbf{k}\cdot\mathbf{r}}$. The functions $u_{n\mathbf{0}}(\mathbf{r})$ are normalized so as to ensure that the following orthonormality relation is satisfied:

$$\langle \phi_{n\mathbf{k}} | \phi_{n'\mathbf{k}'} \rangle = \delta_{nn'}\delta_{\mathbf{k}\mathbf{k}'} \tag{5.5}$$

By rewriting the Schrödinger equation (5.1), using the wavefunction expansion (5.4), and applying the orthonormality condition (5.5), one obtains the following equation:

$$\sum_{n'\mathbf{k}'} a_{n'\mathbf{k}'} \left\{ \langle \phi_{n\mathbf{k}} | H_0 | \phi_{n'\mathbf{k}'} \rangle + \langle \phi_{n\mathbf{k}} | V_p | \phi_{n'\mathbf{k}'} \rangle \right\} = E a_{n\mathbf{k}} \tag{5.6}$$

The matrix element $\langle \phi_{n\mathbf{k}} | H_0 | \phi_{n'\mathbf{k}'} \rangle$ is evaluated using the $\mathbf{k} \cdot \mathbf{p}$ theory [105], which is an approximate description of the bulk band structure using the expansion (5.4). One obtains the expression

$$\langle \phi_{n\mathbf{k}} | H_0 | \phi_{n'\mathbf{k}'} \rangle = H^{\mathbf{k}\cdot\mathbf{p}}_{nn'}(\mathbf{k}) \delta_{\mathbf{k}\mathbf{k}'} \tag{5.7}$$

where $H^{\mathbf{k}\cdot\mathbf{p}}_{nn'}(\mathbf{k})$ is the so-called $\mathbf{k}\cdot\mathbf{p}$ matrix element between bands n and n'. The second matrix element, $\langle \phi_{n\mathbf{k}} | V_p | \phi_{n'\mathbf{k}'} \rangle$ can be expanded as a Fourier series in the reciprocal lattice vectors $\mathbf{q}$ [105]:

$$\langle \phi_{n\mathbf{k}} | V_p | \phi_{n'\mathbf{k}'} \rangle = \sum_{\mathbf{q}} \tilde{V}_p(\mathbf{k} - \mathbf{k}' - \mathbf{q}) \int_{cell} d\mathbf{r} u^*_{n\mathbf{0}}(\mathbf{r}) u_{n'\mathbf{0}}(\mathbf{r}) \tag{5.8}$$

where $\tilde{V}_p(\mathbf{k} - \mathbf{k}' - \mathbf{q})$ is the Fourier transform of $V_p(\mathbf{r})$. The perturbing potential is assumed to be slowly-varying, which means that the Fourier transform is dominated by wave vectors near 0. Since $\mathbf{k}$ and $\mathbf{k}'$ are restricted to the first Brillouin zone, this means that only the $\mathbf{q} = 0$ term contributes significantly to (5.8), and the matrix element can be written as

$$\langle \phi_{n\mathbf{k}} | V_p | \phi_{n'\mathbf{k}'} \rangle = \tilde{V}_p(\mathbf{k} - \mathbf{k}') \delta_{nn'} \tag{5.9}$$

Using (5.9) and (5.7), the result (5.6) can be rewritten as follows:

$$\sum_{n'\mathbf{k}'} a_{n'\mathbf{k}'} \left\{ H^{\mathbf{k}\cdot\mathbf{p}}_{nn'}(\mathbf{k}) \delta_{\mathbf{k}\mathbf{k}'} + \tilde{V}_p(\mathbf{k} - \mathbf{k}') \delta_{nn'} \right\} = E a_{n\mathbf{k}} \tag{5.10}$$

This is the multiband envelope function equation in $\mathbf{k}$-space. To convert it into a real space equation, its Fourier transform is taken, making the substitution $\mathbf{k} \rightarrow (-i\hbar\boldsymbol{\nabla})$ in the $\mathbf{k} \cdot \mathbf{p}$ matrix element and introducing the *envelope functions* defined by

$$F_n(\mathbf{r}) = \sum_{\mathbf{k}} a_{n\mathbf{k}} e^{i\mathbf{k}\cdot\mathbf{r}} \tag{5.11}$$

The real space envelope function equation thus obtained is

$$\sum_{n'} \left\{ H^{\mathbf{k}\cdot\mathbf{p}}_{nn'}(-i\hbar\boldsymbol{\nabla}) + V_p(\mathbf{r}) \delta_{nn'} \right\} F_{n'}(\mathbf{r}) = E F_n(\mathbf{r}) \tag{5.12}$$

The advantage of the envelope function formulation is that the periodic crystal potential and the periodic parts of the Bloch functions have been eliminated, and the

electronic states are now described in terms of the slowly-varying envelope functions $F_n(\mathbf{r})$ and external potential $V_p(\mathbf{r})$. The effects of the crystal structure are represented by the $\mathbf{k}\cdot\mathbf{p}$ hamiltonian $H^{\mathbf{k}\cdot\mathbf{p}}_{nn'}(-i\hbar\nabla)$.

Depending on the degree of accuracy required, the number of bands included in calculations using (5.12) is restricted. In many cases, it is sufficient to consider only the conduction and valence bands. For energies sufficiently close to the conduction band edge, the coupling between the conduction band and the valence bands can also be neglected, and (5.12) reduces to the single-band equation

$$\left\{\frac{-\hbar^2\nabla^2}{2m_c^*} + E_c + V_p(\mathbf{r})\right\} F_c(\mathbf{r}) = EF_c(\mathbf{r}) \tag{5.13}$$

where m_c^* is the conduction band *effective mass*, and E_c is the energy of the conduction band edge. This equation has the same form as the single-electron Schrödinger equation, with the free electron mass replaced by the effective mass, and the envelope function $F_c(\mathbf{r})$ taking the place of the wave function. The E_c term shifts the energy reference level to the conduction band edge.

Two of the valence bands, the light hole and heavy hole bands, are strongly coupled near $\mathbf{k} = 0$, so a single-band effective mass equation like (5.13) cannot be used. Instead, the multiband effective mass equation can be simplified to a 2×2 matrix equation, with the $\mathbf{k}\cdot\mathbf{p}$ hamiltonian given by [105]

$$H^{\mathbf{k}\cdot\mathbf{p}}(\mathbf{k}) = \begin{pmatrix} P+Q & L \\ L^* & P-Q \end{pmatrix} \tag{5.14}$$

where

$$\begin{aligned} P &= E_v^0 + p(\epsilon) - \frac{\hbar^2}{2m_0}\gamma_1 k^2 \\ Q &= q(\epsilon) - \frac{\hbar^2}{2m_0}\gamma_2(k_t^2 - 2k_z^2) \\ L &= \sqrt{3}\frac{\hbar^2}{2m_0}\left[k_t^2\sqrt{\gamma_2^2\cos^2(2\phi) + \gamma_3^2\sin^2(2\phi)} - 2i\gamma_3 k_t k_z\right] \end{aligned} \tag{5.15}$$

with $k_t = \sqrt{k_x^2 + k_y^2}$, $\phi = \arctan(k_y/k_x)$, and L^* denoting the complex conjugate of L. The light and heavy hole band curvature is characterized by three *Luttinger parameters* γ_1, γ_2, and γ_3. E_v^0 is the energy of the valence band edge with zero strain,

and the parameters $p(\epsilon)$ and $q(\epsilon)$ are strain dependent shifts of the band edge energy, which will be calculated in the section 5.2. Note that for $k_t = 0$, $L = L^* = 0$. In this case, the envelope function equations for the light and heavy hole bands are decoupled. The split-off hole band is not strongly coupled to the other valence bands at $\mathbf{k} = 0$, and can be treated in the same way as the conduction band, with its own effective mass. The effective masses and Luttinger parameters can be calculated within the envelope function approximation, but to obtain accurate values it is necessary to include the effects of higher energy bands, using perturbation theory [105]. A simpler approach is to use experimental values, which have been measured for the common bulk semiconductor materials, using cyclotron resonance, magnetophonon resonance [119], and other techniques [2].

The equations describing the dynamics within the EFA are formally derived under the assumption that the external potential varies slowly on the scale of the lattice. One should note that the potential is assumed to be external, i.e. arising from an applied field. The description of heterostructures by an envelope function theory requires the additional assumption that the EFA formalism can be applied, even when the *material properties* change, often abruptly, as a function of position. The validity of this additional assumption cannot be addressed within the formal derivation of the EFA equations [105], and it has been the subject of debate. However, for many quantum well structures, predictions using the EFA have been found to be in excellent agreement with experiment. Theoretical considerations [116] have shown that the EFA can be expected to yield accurate results, provided that the envelope functions are sufficiently slowly varying on the scale of the lattice. The calculated envelope functions for InAs and GaSb quantum wells in GaAs are evaluated in section 5.3.

5.2 Strains and band offsets

In order to apply the EFA to quantum well heterostructures, the relative positions of the band edges in the constituent materials must be specified. The numerical values of the band offsets are not, in fact, easy to determine, and in some cases controversies have even surfaced about the type of alignment (e.g. for GaAsSb/GaAs interfaces [120–124]). The earliest attempts to determine band offsets relied on simple empirical

rules. The electron affinity rule assigns a conduction band offset $\Delta E_c = \chi_1 - \chi_2$, where χ_1, χ_2 are the electron affinities of the respective materials. The common anion rule, on the other hand, assumes a valence band offset of zero for compounds with the same anion, while the offsets for compounds with different anions are obtained from Schottky barrier values. These rules are not strictly applicable and provide only a rough estimate of the band offsets [125]. A number of theoretical methods have been proposed to calculate the band offsets; the model-solid theory [126] has been found to agree well with experiments [125] and will be used in this section to calculate band offsets for InAs and GaSb on GaAs. Experimentally, band offsets can be determined by fitting the quantum well transition energies observed by absorption, photoluminescence or excitation spectroscopies. The accuracy of these methods is affected by the well width determination, and possible inadequacies of the envelope function calculations employed, particularly with regard to nonparabolic bands and thin well layers [125]. Band offset measurements of quantum wells have also been reported using capacitance-voltage [127, 128], and deep level transient spectroscopy measurements [128].

Using the model-solid theory [126], the band offsets can be calculated taking into account the layer strains. The strains are evaluated within the macroscopic elasticity theory (MET). The applicability of the MET to films of single monolayer thickness was questioned based on analysis of high-resolution lattice images [54], but subsequent work using XSW and x-ray absorption fine structure (XAFS) measurements [129] showed that the bond lengths in single monolayer InAs insertions in GaAs are consistent with the predictions of MET. Since the substrates are considerably thicker than the total thickness of the epilayers, the strain introduced into the substrate is negligible, and its lattice constant is just that of the bulk material. The in-plane lattice constant of the epilayers, $a_{\parallel}^{epi}$ conforms to that of the substrate, and the lattice constant $a_{\perp}^{epi}$ in the direction normal to the surface is given by

$$a_{\perp}^{epi} = a_0^{epi}[1 - D_{hkl}(a^{sub}/a_0^{epi} - 1)] \tag{5.16}$$

where a_0^{epi} is the bulk (unstrained) lattice constant of the epilayer material and a^{sub} is the lattice constant of the substrate. The constant D_{hkl} depends on the elastic constants c_{11}, c_{12}, and c_{44} of the epilayer material, and the interface orientation. For

the (001) orientation, it is given by

$$D_{001} = 2\frac{c_{12}}{c_{11}} \tag{5.17}$$

The fractional volume change of the stained layer, $\Delta\Omega/\Omega$, is given by

$$\frac{\Delta\Omega}{\Omega} = \mathrm{Tr}(\overleftrightarrow{\epsilon}) = (\epsilon_{xx} + \epsilon_{yy} + \epsilon_{zz}) \tag{5.18}$$

where, for strain along (001), the strain components are given by

$$\begin{aligned} \epsilon_{xx} = \epsilon_{yy} &= \left(\frac{a_{\parallel}^{epi}}{a_0^{epi}} - 1\right) \\ \epsilon_{zz} &= \left(\frac{a_{\perp}^{epi}}{a_0^{epi}} - 1\right) \end{aligned} \tag{5.19}$$

The approach of the model-solid theory is to relate the band edges of different materials to a fixed energy level. The method combines a calculation of the band structures of the individual bulk semiconductors using density-functional theory, with a model of the solid as a superposition of neutral atoms. Since the density-functional calculations do not reproduce the correct energy gap, and do not take into account spin-orbit effects, the average valence band level is calculated, and the experimentally measured band gap and spin-orbit splitting are added *a posteriori*. The details of the density-functional calculations will not be discussed here; we shall simply use the results for the average energy level $E_{v,av}$, as tabulated by Van de Walle [126].

For unstrained material, the valence band and conduction band edge energies, E_v^0 and E_c^0, are given by

$$\begin{aligned} E_v^0 &= E_{v,av} + \frac{\Delta_0}{3} \\ E_c^0 &= E_v^0 + E_g \end{aligned} \tag{5.20}$$

where E_g is the band gap energy and the usual convention of assigning 1/3 of the spin-orbit splitting Δ_0 to the heavy and light hole bands is employed. For strained material, the shifting of the bands due to the volume change must be taken into account. This is expressed by

$$\Delta E_{(v,c)} = a_{(v,c)}\frac{\Delta\Omega}{\Omega} \tag{5.21}$$

where a_v and a_c are the hydrostatic deformation potentials for the valence and conduction bands, respectively. Additionally, the strain induces a splitting of the light and heavy hole bands, so that these are no longer degenerate at $\mathbf{k} = 0$. It is convenient to define a parameter

$$\delta E_{001} = 2b(\epsilon_{zz} - \epsilon_{xx}) \tag{5.22}$$

where b is the shear deformation potential for strain with tetragonal symmetry. For material strained along the [001] direction, the heavy hole, light hole and conduction band edges, E_{hh},E_{lh} and E_c are given by [105]

$$\begin{aligned} E_{hh} &= E_{v,av} + \frac{\Delta_0}{3} + a_v\frac{\Delta\Omega}{\Omega} - \frac{1}{2}\delta E_{001} \\ E_{lh} &= E_{v,av} - \frac{\Delta_0}{6} + \frac{1}{4}\delta E_{001} + \frac{1}{2}\left[\Delta_0^2 + \Delta_0\delta E_{001} + \frac{9}{4}(\delta E_{001})^2\right]^{1/2} \\ E_c &= E_c^0 + a_c\frac{\Delta\Omega}{\Omega} \end{aligned} \tag{5.23}$$

where E_c^0 is the conduction band edge for unstrained material, given by(5.20).

The absolute band edge energy levels in (5.23) do not carry any physical meaning, taken by themselves [126]. However, the relative levels of these quantities in different semiconductors determine the band offsets. These are illustrated for the case of unstrained and coherently strained InAs and GaSb quantum wells in GaAs in Fig. 5.1. All experimental parameters for bulk GaAs, InAs and GaSb are summarized in Table 5.1. The model-solid theory predicts a strongly type-II band lineup for coherently strained GaSb layers in GaAs, whereas the band lineup for InAs/GaAs is type-I.

5.3 Electronic states in quantum wells

The envelope function theory is extended to the description of heterostructures by letting the band edge energies and the effective masses (or Luttinger parameters) become functions of the position vector $\mathbf{r}$. For structures with planar interfaces, such as the quantum well structures we will consider, these quantities are functions of the z coordinate only. For simplicity, we shall consider cases in which the external potential $V_p(\mathbf{r})$ is zero.

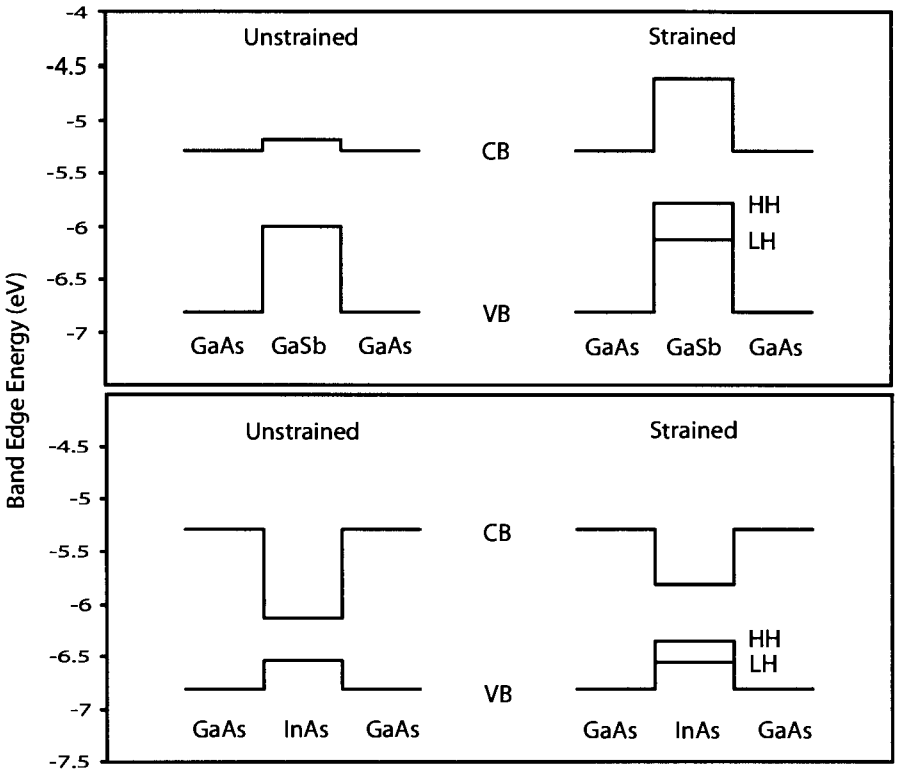

Figure 5.1: Band edge energies in unstrained and coherently strained GaSb and InAs quantum wells in GaAs, according to the model solid theory

5.3.1 Conduction band states

The single-band effective mass equation for the conduction band, with a z-dependent band edge energy and effective mass, is

$$\left\{\frac{-\hbar^2\nabla^2}{2m_c^*(z)} + E_c(z)\right\} F_c(\mathbf{r}) = EF_c(\mathbf{r}) \tag{5.24}$$

However, the z-dependence of the effective mass gives rise to an ambiguity in the kinetic energy operator, since $1/m_c^*(z)$ and ∇^2 do not commute. It is not possible to define a unique "correct" form of this operator, but the ordering $-\hbar^2\boldsymbol{\nabla}\cdot(1/m_c^*(z)\boldsymbol{\nabla})$ is hermitian [105], which satisfies a requirement of conventional quantum mechanics. Using separation of variables, (5.24) can be simplified to an ordinary differential

Table 5.1: Bulk material parameters used in the model solid theory and EFA calculations. Values are taken from [2] with the exception of $E_{v,av}$ which is given by [126]. (Note: The sign of a_v has been reversed to agree with the notation of [126], which is adopted in this work.)

Parameter	GaAs	InAs	GaSb
a (Å)	5.6533	6.0583	6.0959
E_g (eV)	1.519	0.417	0.812
c_{11} (GPa)	1221	832.9	884.2
c_{12} (GPa)	566	452.6	402.6
Δ_0 (eV)	0.341	0.39	0.76
a_c (eV)	-7.17	-5.08	-7.5
a_v (eV)	1.16	1	0.8
b (eV)	-2	-1.8	-2
$E_{v,av}$ (eV)	-6.92	-6.67	-6.25
m_e^*	0.067	0.026	0.039
γ_1	6.98	20	13.4
γ_2	2.06	8.5	4.7
γ_3	2.93	9.2	6

equation in z. The envelope function may be written as a product

$$F_c(\mathbf{r}) = G_c(x,y)H_c(z) \tag{5.25}$$

where the factor $G_c(x,y)$ is proportional to $\exp(i(k_x x + k_y y)$. The z-dependent function $H_c(z)$ then satisfies

$$\left[\frac{-\hbar^2}{2}\frac{d}{dz}\frac{1}{m_c^*(z)}\frac{d}{dz} + E_c(z) + \frac{\hbar^2\sqrt{k_x^2+k_y^2}}{2m_c^*(z)}\right] H_c(z) = EH_c(z) \tag{5.26}$$

which can then solved for any specified values of k_x and k_y. Here, we will be interested in the solutions at $k_x = k_y = 0$.

For a simple quantum well structure, consisting of a layer of thickness L, of well material W, bounded by thick layers of barrier material B, the band edge energy

$E_c(z)$ can be expressed as

$$E_c(z) = \begin{cases} E_c^B & z < -L/2 \\ E_c^W & |z| < L/2 \\ E_c^B & z > L/2 \end{cases} \tag{5.27}$$

The z-dependent band edge energy thus forms an effective potential well. Note that this confinement potential does not arise from an electric field, and therefore does not satisfy Poisson's equation, as an external electrostatic potential would. Relations similar to (5.27) apply to the effective mass m_c^*.

Since E_c and m_c^* are constant in the well and in the barriers, (5.26) reduces to a Helmholtz equation within each region, and we can immediately write down the form of the solutions. For bound states, the energy eigenvalue will be lower than $E_c(z)$, leading to an exponentially decaying solutions in the barriers, whereas the solution in the well is oscillatory:

$$H_c(z) = \begin{cases} Ae^{\kappa z} & z < -L/2 \\ B\sin kz + C\cos kz & |z| < L/2 \\ De^{-\kappa z} & z > L/2 \end{cases} \tag{5.28}$$

where $\kappa \equiv \sqrt{2m_c^{*(B)}(E_c^B - E)/\hbar^2}$ and $k \equiv \sqrt{2m_c^{*(W)}(E - E_c^W)/\hbar^2}$.

To complete the solution, boundary conditions must be imposed at the interfaces, $z = \pm L/2$ (we have already implicitly imposed boundary conditions at $z = \pm\infty$ in retaining only the exponentially decaying functions in the barrier). At both interfaces, the envelope function $H_c(z)$ must be continuous from one side to the other. Boundary conditions for $H_c'(z)$ are obtained by integrating (5.26) across the interfaces. At $z = L/2$, one obtains

$$\frac{1}{m_c^*(z)}\frac{dH_c(z)}{dz}\bigg|_{L/2-\epsilon}^{L/2+\epsilon} = \int_{L/2-\epsilon}^{L/2+\epsilon} dz\,[E_c(z) - E]\,H_c(z) \tag{5.29}$$

with a similar condition holding at $z = -L/2$. As $\epsilon \to 0$, the right-hand side of (5.29) becomes zero, so the boundary condition is

$$\frac{1}{m_c^*(z)}\frac{dH_c(z)}{dz}\bigg|_{L/2+} = \frac{1}{m_c^*(z)}\frac{dH_c(z)}{dz}\bigg|_{L/2-} \tag{5.30}$$

Since the effective mass is different on either side of the interface, this boundary condition differs from the one employed in the standard quantum mechanics problem, in which the first derivative of the wave function is continuous across the boundary. The application of the boundary conditions is simplified by noting that $H_c(z)$ must be either even or odd (because $E_c(z)$ is even). For even solutions, then, $A = D$ and $B = 0$. Applying the two boundary conditions at $z = L/2$, one obtains

$$\frac{m_c^{*(W)}}{m_c^{*(B)}}\frac{\kappa}{k} = \tan\frac{kL}{2} \tag{5.31}$$

Similarly, for odd solutions $A = -D$ and $C = 0$, and one obtains

$$\frac{m_c^{*(W)}}{m_c^{*(B)}}\frac{\kappa}{k} = -\cot\frac{kL}{2} \tag{5.32}$$

Equations (5.31) and (5.32) have no analytic solution, so the energy eigenvalues E are calculated by solving these equations numerically. There is always at least one bound state solution, for any values of L, E_c^B and E_c^W [105]. The lowest-energy bound state is an even solution.

5.3.2 Valence band states

For the light and heavy hole bands, the envelope function equation (5.12), with the $\mathbf{k}\cdot\mathbf{p}$ hamiltonian given by (5.14), can be solved using boundary conditions similar to those applied to the conduction band. To obtain the energy eigenvalues for arbitrary k_x and k_y, a system of eight equations must be solved. However, for the purpose of predicting the transition energy observed in PL measurements, we only need to find the energy eigenvalues for $k_x = k_y = 0$. In this case, the light and heavy hole equations are decoupled, and we can proceed with separation of variables, exactly as in the case of the conduction band. From the definitions of P and Q (5.15), effective masses along the k_z direction can be defined for the two bands,

$$\begin{aligned} m_{HH}^{(z)} &= \frac{1}{(\gamma_1 - 2\gamma_2)}m_0 \\ m_{LH}^{(z)} &= \frac{1}{(\gamma_1 + 2\gamma_2)}m_0 \end{aligned} \tag{5.33}$$

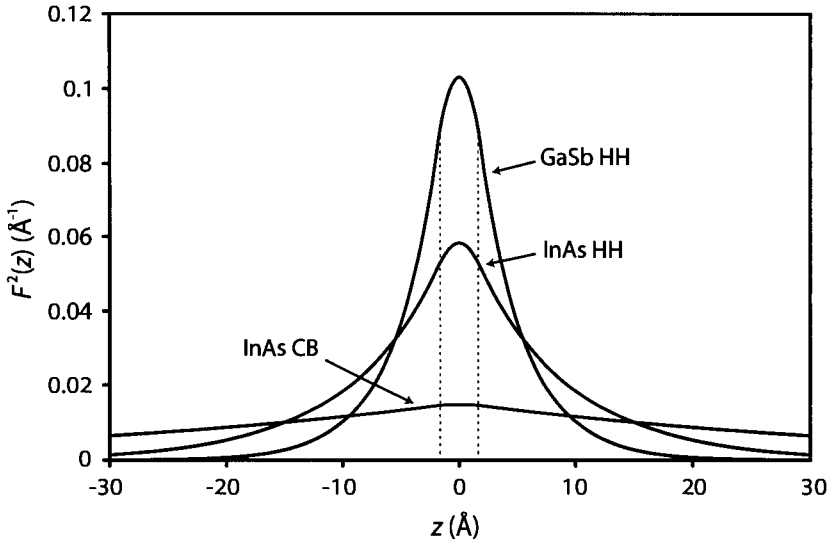

Figure 5.2: Probability density (squared envelope function) for the lowest energy bound states in the heavy hole (HH) and conduction band (CB) of 1ML thick InAs and GaSb quantum wells in GaAs. Dotted lines show the quantum well boundaries.

and the eigenvalues for each band can be obtained by solving equations analogous to (5.31) and (5.32).

The squared absolute values of the envelope functions (i.e., the probability densities for the electrons and holes, respectively) were computed for the lowest ($n = 1$) bound states in 1 ML thick quantum wells of InAs and GaSb in GaAs. These functions are shown in Fig. 5.2. The heavy holes are clearly much more strongly confined, due to their heavier effective mass. The stronger confinement of the heavy hole in GaSb quantum wells, compared to InAs quantum wells, is due to the larger valence band offset. Since the GaSb layer forms a barrier in the conduction band, there is no bound state for electrons in the GaSb quantum well. In all cases there is considerable penetration of the envelope function into the barrier layers. The uncertainty in the position, defined by

$$\Delta x = \sqrt{\langle x^2 \rangle - \langle x \rangle^2} \tag{5.34}$$

is 42 Å for the conduction band, and 10 Å for the heavy hole band in InAs quantum

wells, and 5.5 Å for the heavy hole band in GaSb quantum wells. The width of the corresponding k-space function can be estimated using $\Delta x \Delta k \approx 1$; for InAs quantum wells, this width is approximately 5% of the first Brillouin zone for electrons and 20% for heavy holes. For heavy holes in GaSb quantum wells, Δk extends over roughly 30% of the first Brillouin zone. For the heavy hole solutions, then, one can expect that the $k = 0$ approximations, which are used in the envelope function approximation in calculating the cell-periodic functions $u_{n\mathbf{k}}(\mathbf{r})$ and the effective masses, may be somewhat inaccurate. However, the envelope functions are slowly-varying in the sense that Δk does not exceed the width of the first Brillouin zone.

5.3.3 Multiple quantum wells

For multiple quantum well and superlattice structures, the boundary conditions discussed in section 5.3.1 are applied at each interface. Using numerical techniques, the energy eigenvalues can be calculated for structures with an arbitrary number of wells. However, a simpler method is to estimate the effects of multiple wells by applying periodic boundary conditions. This is the same approach that is employed in the well-known Kronig-Penney model [130], but the solution is modified by taking into account the different effective masses in each material. The discrete energy levels of the single quantum well become broadened into *minibands* in a superlattice, with dispersion relations $E_j(k_z)$. The conduction band dispersion relation in a superlattice with periodic boundary conditions is given by [125]

$$\cos(k_z L) = \cos(k_w L_w)\cos(k_b L_b) - \frac{1}{2}\left(r + \frac{1}{r}\right)\sin(k_w L_w)\sin(k_b L_b) \tag{5.35}$$

where $r = k_b m_w^* / k_w m_b^*$. L_b and L_w are the thicknesses of the barrier and well layers, respectively, $L = L_b + L_w$ is the superlattice period, and k_b and k_w are given by $\sqrt{2m^*(E - E_c)/\hbar^2}$, using the barrier and well parameters, respectively. For energies lower than the barrier band edge, the dispersion relation is expressed in real quantities by defining $\kappa_b = \sqrt{2m^*(E_c - E)/\hbar^2}$, to obtain

$$\cos(k_z L) = \cos(k_w L_w)\cosh(\kappa_b L_b) + \frac{1}{2}\left(r - \frac{1}{r}\right)\sin(k_w L_w)\sinh(\kappa_b L_b) \tag{5.36}$$

with $r = \kappa_b m_w^* / k_w m_b^*$. The energy levels of the top and bottom of the miniband are obtained by setting $\cos(k_z L) = \mp 1$, respectively. As the barrier layer thickness

becomes large, the top and bottom of a miniband converge to the single quantum well bound state solution, if the energy is lower than the barrier band edge.

5.4 Optical transitions in quantum wells

The experimental technique used in this thesis to study transitions between the quantum well states is PL spectroscopy. As was noted in Chap. 2, the PL emission is dominated by the lowest-energy available transitions. For the type-I InAs/GaAs quantum well, the lowest-energy emission occurs from recombination of heavy holes and electrons in the lowest bound levels in the quantum well (for a 1 ML thick InAs layer there is, in fact, only a single bound level for each type of carrier). For type-II quantum wells, only one type of carrier is localized in the well layer; in GaSb/GaAs quantum wells the holes are confined by the GaSb layer, whereas the electrons are located in the GaAs barriers. A radiative transition is made possible by the spatial overlap of the electron and hole wave functions. This type of transition is sometimes referred to as "spatially indirect", although the transition rate is proportional to the integral over all space of the product of the electron and hole wavefunctions (i.e., the joint probability for the electron and hole to be at the same position) as is the case for all radiative transitions. For type-I quantum wells, the overlap of the conduction and valence band envelope functions is larger than in the bulk case, resulting in an enhanced transition rate and strong optical emission. Due to the spatial separation of the hole and electron envelope functions in a type-II quantum well, the overlap integral is reduced in comparison to a type-I quantum well, and the optical emission is weaker.

The discussion of the envelope function theory started from the one-electron picture. The optical spectra of semiconductors, however, exhibit features that can only be explained by considering the interactions between electrons. A simplification of the complex many-body problem is to consider only the Coulomb attraction between an electron and a hole, which causes their motions to be correlated. The bound states of the electron-hole pair are known as excitons. The exciton motion can be treated in a manner analogous to that of the hydrogen atom; the well-known quantum mechanical results can therefore be used, replacing the proton and electron masses by the effective

masses of the hole and electron and including the zero-frequency dielectric constant, ε, of the the semiconductor where appropriate. In a bulk semiconductor, the exciton energy levels E_n are given by [4]

$$E_n = E_g - \frac{R^*}{n^2} \tag{5.37}$$

where E_g is the band gap, R^* is the Rydberg constant defined by

$$R^* = \frac{\mu e^4}{2\hbar^2 \varepsilon^2} \tag{5.38}$$

where μ is the reduced mass. The energy levels of a two-particle system can also be calculated easily in two dimensions; in this case the exciton binding energy is $4R^*$, i.e., four times greater than in the three dimensional case [5].

For quantum wells of finite thickness, the Schrödinger equation including both the confinement potentials and the Coulomb interaction must be solved. For a strained quantum well, the valence band is non-degenerate at $\mathbf{k} = 0$, so heavy-hole and light-hole exciton systems are formed; their reduced masses are given by [131]

$$\frac{1}{\mu_\pm} = \frac{1}{m_e^*} + \frac{1}{m_0}(\gamma_1 \pm \gamma_2) \tag{5.39}$$

where $+$ and $-$ represent heavy and light holes, respectively, m_e^* is the electron effective mass, and m_0 is the free electron mass. The exciton binding energy has been found to be intermediate between the 2D and 3D limits for type-I quantum wells; a maximum binding energy occurs for a certain quantum well thickness, where the envelope functions are most strongly localized [131]. For type-II quantum wells, a variational calculation [132] found exciton binding energies to be reduced, compared with the bulk case. The variational method was applied to ultrathin GaSb/GaAs quantum wells [6] and indicated that in these structures the s-type exciton should be unstable. However, a numerical solution of the Schrödinger equation taking into account the Coulomb correlation, finite barrier heights, and image charge effects indicated that the variational method is unsatisfactory; the more detailed calculation showed that in type-II quantum wells the excitonic binding energy may be larger than the bulk value, although less so than in type-I systems [133].

At a type-II interface, a blue shift of the transition energy with the excitation power density (EPD) is expected due to the effect of charge separation, which increases as the

carrier population increases. This effect has been modelled by a triangular potential well, resulting in a shift which is proportional to $D^{1/3}$, where D is the EPD [6, 134]. However, there are other effects of similar magnitude that can contribute to the shift of the type-II transition energy, including band distortion and many-body Coulomb effects (which both produce a red shift) and state filling (which produces a blue shift); the energy shift therefore shows a more complicated dependence on the EPD than a simple 1/3 power law [135–137]. The energy shift may be additionally affected by imperfections (e.g. grading) of the interface; experimentally, nearly logarithmic shifts have been observed in some cases for type-II quantum wells [134, 138].

5.5 Photoluminescence results

Low temperature (2 K) PL measurements were performed on the GaSb/GaAs MQW samples grown by the flashoff sequence, discussed in Sect. 4.1.4, as well as a small number of samples grown without using any flashoff steps. For the flashoff samples, the power density of the exciting laser beam was varied between 0.05 mW/cm^2 and 10 W/cm^2; values of the EPD were estimated from the laser output power and the laser spot diameter. The samples grown without flashoff steps, for which PL spectra are available, were grown using a variety of different growth conditions, and the Sb concentration profile was not studied for all of these conditions. Based on the results presented in Chap. 4, however, it is reasonable to assume that the quantum wells in the non-flashoff samples are considerably less abrupt than in the flashoff samples. PL spectroscopy was also performed on InAs/GaAs MQW and single quantum well (SQW) samples, grown using a conventional OMVPE growth sequence at 550 °C and 600 °C. The PL measurements were performed using a Si avalanche photodiode (APD) as the detector, except where otherwise noted.

5.5.1 GaSb/GaAs quantum wells

The PL spectra shown in Fig. 5.3 were obtained from MQW samples grown using OMVPE sequences without any flashoff steps. The nominal amount of GaSb deposition for these samples was approximately 1 ML or lower, based on the known GaAs

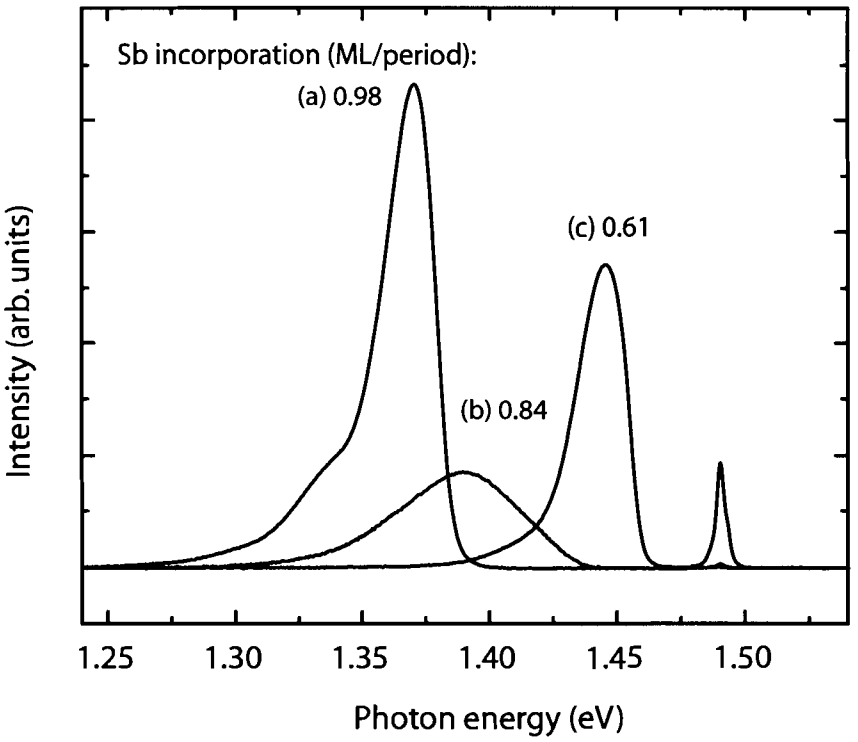

Figure 5.3: PL spectra of GaSb/GaAs MQW samples grown using OMVPE sequences without any flashoff steps.

growth rate. The spectra show a strong quantum well-related luminescence line well below the GaAs band gap energy, with no evidence of luminescence related to 3D islands (only the spectral region of the quantum well lines is shown in the figure). The spectra were obtained using the Si APD detector which has a weak response in the spectral range where 3D islands emit, but the 3D luminescence line should be detectable if islands were present, as will be explained in more detail below. Spectra (a) and (c) were obtained with an EPD of 20 mW/cm^2, while spectrum (b) was obtained with an EPD of 500 mW/cm^2. The samples corresponding to spectra (a) and (c) were grown in a horizontal quartz reactor, which was in use in the OMVPE system until September, 2000. These samples were grown at 500 °C with precursor flows of 9.9×10^6 mol/min (TEGa) and 2.9×10^5 mol/min (TMSb and TBAs). The quantum wells in the sample corresponding to spectrum (c) were formed by 10 s exposure to TMSb followed by 0.2 s TEGa, while those in the sample corresponding to spectrum (a) were formed with an additional 1 s of GaSb growth after the TMSb exposure. Spectrum (b) was obtained from a sample grown in the vertical OMVPE reactor, described in Chap. 2, which was also used to grow all other samples described in this thesis. This sample was grown at 520 °C using a lower GaSb growth rate; the TEGa flows were 2.8×10^6 mol/min for the GaSb layers and 5.2×10^6 for the GaAs barriers. The TBAs flow was 2.5×10^5 mol/min and the TMSb flow was 1.2×10^5 mol/min. The GaSb growth time was 2 s, with no TMSb exposure preceding the growth step. This sample showed a considerably broader PL line width, with a full width at half-maximum (FWHM) of $\sim$ 55 meV, compared to $\sim$ 25 meV for spectra (a) and (c). The amount of Sb incorporated per period was determined from XRD data as described in Chap. 4, and is noted above each spectrum in Fig. 5.3. The quantum well-related transition energy decreases with increasing Sb content, as expected. In addition to the main quantum well-related feature, the sample with the lowest Sb incorporation — spectrum (c) — exhibits a sharp line at 1.49 eV, which arises from the carbon donor-acceptor pair band in bulk GaAs. This feature is also present in the other two spectra, but much weaker. Spectrum (a) has a shoulder $\sim$ 30 meV below the main quantum well peak. The shoulder may be attributable to a carbon impurity related transition whose energy is shifted by the confinement due to the quantum well, as has been suggested previously for InAs/GaAs quantum wells [107]. The energy difference

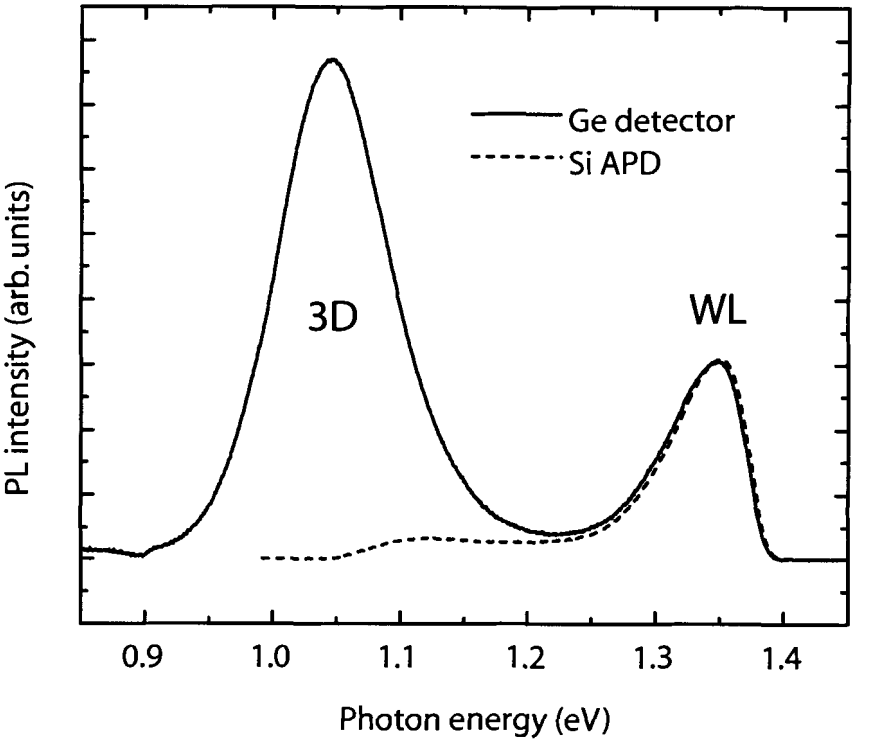

Figure 5.4: PL spectra of a GaSb/GaAs MQW sample with 3D islands, grown using the conventional growth sequence.

between the shoulder and the main peak is, however, also close to the energy of the longitudinal optical (LO) phonon at the Γ point in GaAs, 35.3 meV [139].

With a nominal GaSb deposition of ~ 2 ML, 3D islands were observed, as shown in the TEM image in Fig. 4.8 in the previous chapter. PL spectra from this sample are shown in Fig. 5.4. The spectrum shown as a solid curve was obtained with a Ge detector in order to collect luminescence at wavelengths longer than the cutoff wavelength of the Si APD; the spectrum collected with the Si APD is shown as a dashed curve. The spectrum shows two PL lines — the lower energy line, labelled "3D", is at an energy comparable to luminescence from GaSb 3D islands (quantum dots) reported previously by a number of authors [71, 73, 140, 141], which was attributed to transitions between heavy holes confined in the GaSb quantum dots and electrons

in the GaAs barrier layers [140]. The higher energy line, labelled "WL" is due to the planar wetting layers. The 3D line has a large FWHM of 110 meV, similar to that observed previously and attributed to the distribution of dot sizes [140]. With a FWHM of 60 meV, the WL line is also broader than the lines observed for the samples without 3D islands in Fig. 5.3. The 3D luminescence is detected (although weakly) even with the Si APD, which means that those samples which do not show this luminescence line probably contain only planar wetting layers.

Fig. 5.5 shows PL spectra of GaSb/GaAs MQW samples grown with the flashoff sequence, with GaSb growth times up to the critical deposition time of 1.6 s (see section 4.1.4), at three different values of the EPD. The spectra in the lowest panel are labelled with the GaSb incorporation per period determined from XRD data. At the lowest EPD, the FWHM for the sample with 0.93 ML of GaSb per period is 75 meV, while the four other samples have sharper peaks, with a FWHM of around 50 meV. The peaks are asymmetric, with wider tails on the low-energy side. At the highest EPD, there is a greater spread in the line width; the FWHM increases from 15 meV for the sample with 0.28 ML of GaSb per period, to 68 meV for the sample with 0.93 ML of GaSb per period. The three samples with the lowest GaSb incorporation show a shoulder approximately 30 meV below the energy of the main peak, as was also noted for one of the spectra shown in Fig. 5.3.

Fig. 5.6 shows the blue shift in the energy of the main PL peak with increasing EPD. For convenient comparison the samples with various amounts of Sb incorporation are plotted together by subtracting the transition energy at the lowest EPD for each sample. The samples show a similar magnitude of the blue shift of the transition energy, except for the sample with the lowest Sb incorporation (0.28 ML/period), which shows a considerably weaker shift than the other samples. The energy shift appears closer to a logarithmic dependence than a $D^{1/3}$ power law, as shown by the calculated curves. This is in contrast to the results reported by Ledentsov *et al.* for GaSb/GaAs quantum wells [6] and the wetting layer PL from GaSb/GaAs quantum dot samples [140], both of which showed a $D^{1/3}$ dependence. Those reports used EPDs up to 250 W/cm^2, considerably higher than the strongest EPD used in this work. The determination of the transition energy at the lowest EPD in the present work is also subject to uncertainty because of the large PL linewidth and the poor

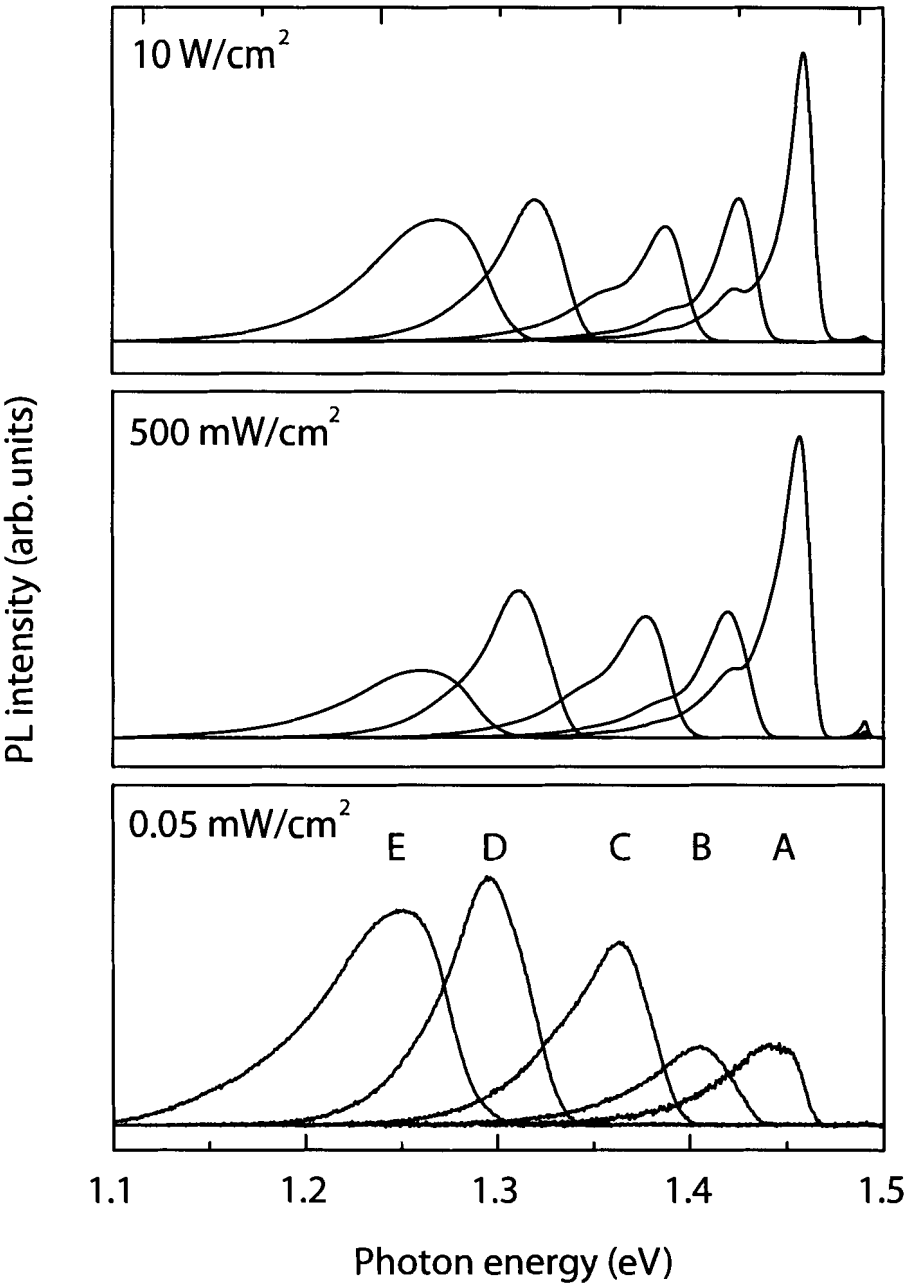

Figure 5.5: PL spectra at three different excitation power densities of GaSb/GaAs MQW samples with: 0.28 (A), 0.46 (B), 0.60 (C), 0.78 (D), 0.93 (E) ML/period Sb incorporation.

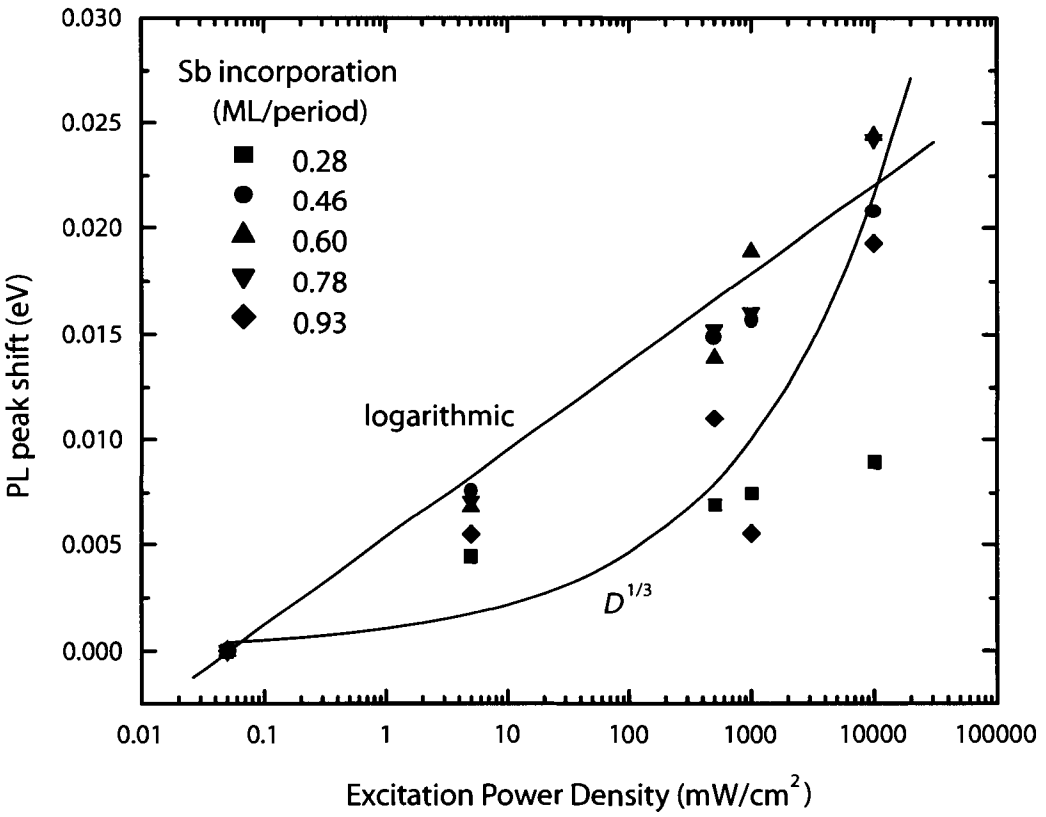

Figure 5.6: PL peak energy shift with excitation power density for various GaSb/GaAs MQW samples.

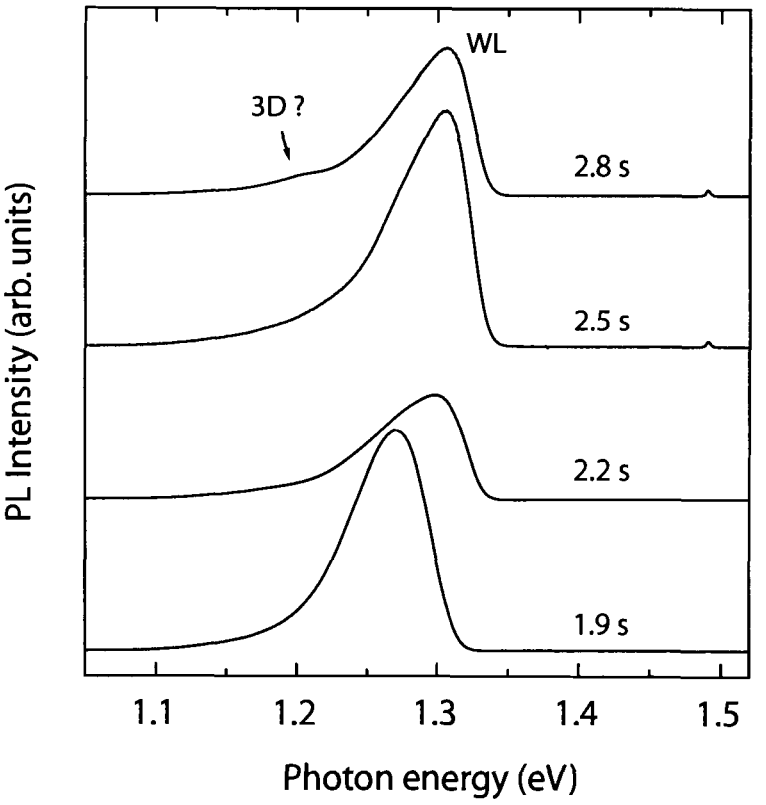

Figure 5.7: PL spectra of GaSb/GaAs MQW samples grown using the flashoff sequence, with GaSb deposition times greater than 1.6 s; 500 mW/cm^2 excitation power density. Spectra are labelled with the GaSb deposition time. WL: wetting layer related line; 3D?: shoulder possibly related to 3D GaSb islands.

signal-to-noise ratio.

The PL spectra of the GaSb/GaAs MQW samples grown using the flashoff sequence, with GaSb growth times exceeding the critical deposition time of 1.6 s, are shown in Fig. 5.7. These spectra were obtained with an EPD of 500 W/cm^2. The spectra do not show the expected luminescence line associated with 3D islands (the spectra were obtained with a Si APD used as the detector, but the 3D line should still be detectable, as was discussed above). The sample with the longest GaSb growth time (2.8 s) shows a weak shoulder (labelled "3D") approximately 100 meV below the wetting layer peak (labelled "WL"); the shoulder may be attributable to 3D islands.

If that is the case, the islands are either considerably thinner or more strongly intermixed with the surrounding GaAs than those observed in the sample grown without flashoff steps, since the 3D transition energy is closer to the wetting layer transition energy. The PL spectra thus suggest that the 3D islands are altered during the 200 s growth interruptions under TBAs employed in the flashoff sequence, possibly as a result of an As-for-Sb exchange process. Non-radiative recombination at dislocations within the dots might also explain the lack of a dot-related luminescence line, but this would be difficult to reconcile with the strong dot-related line observed for samples grown using a conventional OMVPE sequence.

Fig. 5.8 shows the PL transition energies as a function of Sb coverage for MQW samples grown with both the flashoff sequence and a conventional OMVPE sequence (ΔE represents the difference of the PL transition energy and the GaAs band gap). For samples with 3D islands, the energy of the wetting layer line is plotted. The plotted transition energies are obtained from the peak energy at an EPD of 500 mW/cm^2, since this was the only value for which a spectrum was available for a number of the samples. The two exceptions are the spectra from Fig. 5.3, obtained at 20 mW/cm^2 (i.e. the outer two of the points labelled "B"). The plotted experimental transition energies are therefore somewhat higher — roughly 15 meV, from Fig. 5.6 — than the zero-carrier value because of the blue shift of the luminescence line with increasing EPD. The curves are calculated using the EFA; since the thickness of the barrier layers is large enough (200 Å) that inter-well coupling effects are negligible, the single quantum well energy levels are plotted. For curve (a), the band offsets for the GaSb/GaAs interface are obtained from the model-solid theory (see Sect. 5.2) with the width of the quantum well scaled according to the Sb coverage (3.25 Å corresponds to 1 ML GaSb). Curve (b) is calculated in the same way, using a different set of band offsets obtained from previously published experimental work. In that work, the band lineup was determined by fitting the observed PL transitions in $GaAs_{1-x}Sb_x/GaAs$ quantum wells [123]. In both cases, the predicted band lineup is type-II, with the conduction band lying higher in GaSb than in GaAs. The transition is accordingly assumed to take place between electrons at the conduction band edge in the GaAs barrier layers and the confined heavy hole state in the GaSb quantum well; excitonic effects are not included in the calculation. The transition energies observed for the samples grown

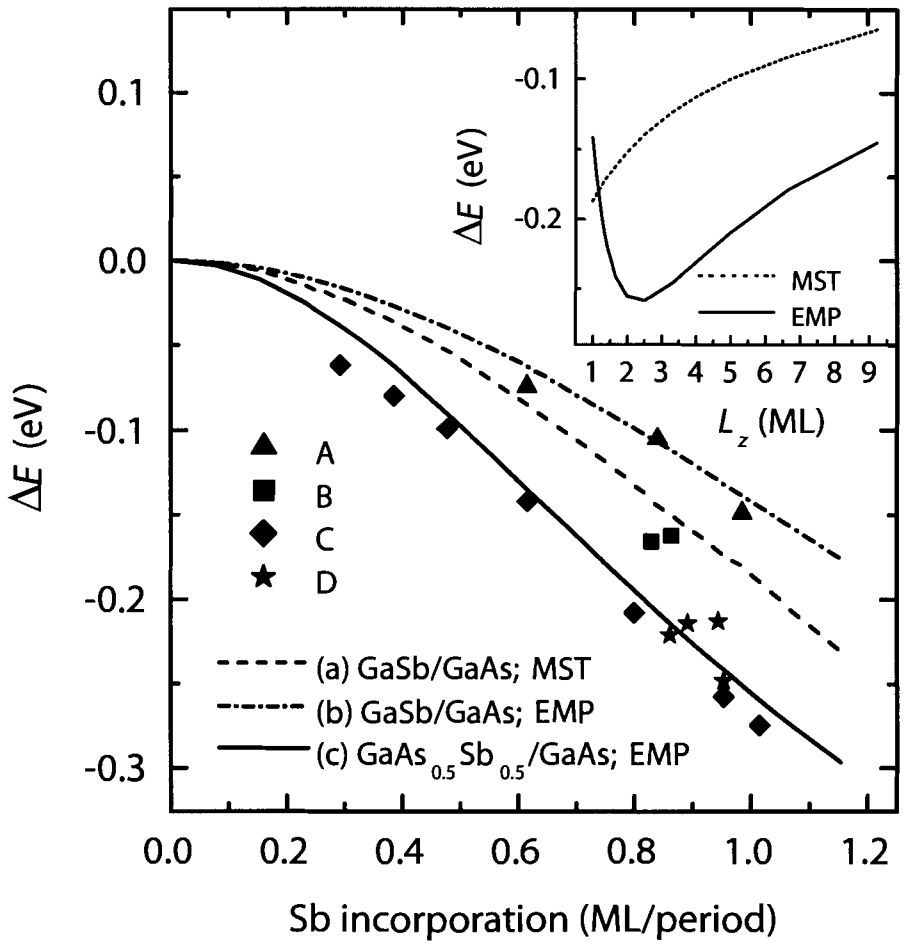

Figure 5.8: PL transition energy (measured from the GaAs band gap) as a function of Sb coverage. The curves are calculated using band offsets from model solid theory (MST) [126] or an empirical fitting scheme (EMP) [123]. Symbols represent (A) Conventional growth samples without 3D islands — see Fig. 5.3; (B) Wetting layer PL from conventional growth samples with 3D islands — see Fig. 5.4; (C) Flashoff samples with GaSb growth times up to 1.6 s — see Fig. 5.5; (D) Wetting layer PL from flashoff samples with GaSb growth times above 1.6 s — see Fig. 5.7. Inset: Calculated dependence of the transition energy on well width for broadened wells with Sb content equivalent to 1 ML GaSb.

with the flashoff sequence are considerably lower than either curve (a) and curve (b). Transitions observed for the samples grown without any flashoff steps are at a higher energy than those observed for the flashoff samples.

In order to examine the possible influence of As-Sb intermixing on the transition energies, a simple model consisting of an intermixed quantum well layer of uniform composition with GaAs barriers was considered. The inset to Fig. 5.8 shows the dependence of the transition energy on the width L_z of a $GaAs_{1-x}Sb_x$ quantum well whose composition x depends inversely on L_z so that the total Sb content is kept equal to that of 1 ML of GaSb. The dashed curve is calculated using the band offsets from the model solid theory, in which the large bowing parameter of $GaAs_{1-x}Sb_x$, 1.2 eV, is assigned entirely to the conduction band [126]; with these band offsets, the transition energy is predicted to increase as the width increases. The solid curve, on the other hand, uses band offsets obtained from the previously mentioned empirical fitting study [123]; in that work, 90% of the bowing was attributed to the valence band. Using the empirical band offsets, a minimum occurs in the transition energy where the well is broadened by a factor of approximately 2.5. If the empirically determined band offsets are correct, a relatively small amount of As-Sb intermixing could explain the data for the samples grown by the flashoff technique. Curve (c) in Fig. 5.8 shows the calculated dependence of the transition energy on Sb incorporation assuming a $GaAs_{0.5}Sb_{0.5}$ well, with the band offsets taken from Ref. [123]. The higher-lying transition energies observed for the samples grown with the conventional growth sequence can be explained within the effective mass approximation, if a greater degree of broadening is assumed — using the empirical band offsets, the transition energy for a quantum well broadened by a factor of ~ 9 equals the transition energy for 1 ML GaSb, as shown in the inset. Evidently, the predictions of the effective mass approximation are strongly dependent on the compositional profile of Sb within the structure and on the proportion of the $GaAs_{1-x}Sb_x$ band gap bowing assigned to the valence band; neither of these is known with sufficient accuracy to attempt a more detailed comparison of theory and experiment.

The experimental dependence of the transition energies on quantum well thickness reported by Ledentsov *et al.* [6] was even closer to the GaAs band gap than that obtained for the conventional growth samples in the present work. The authors also

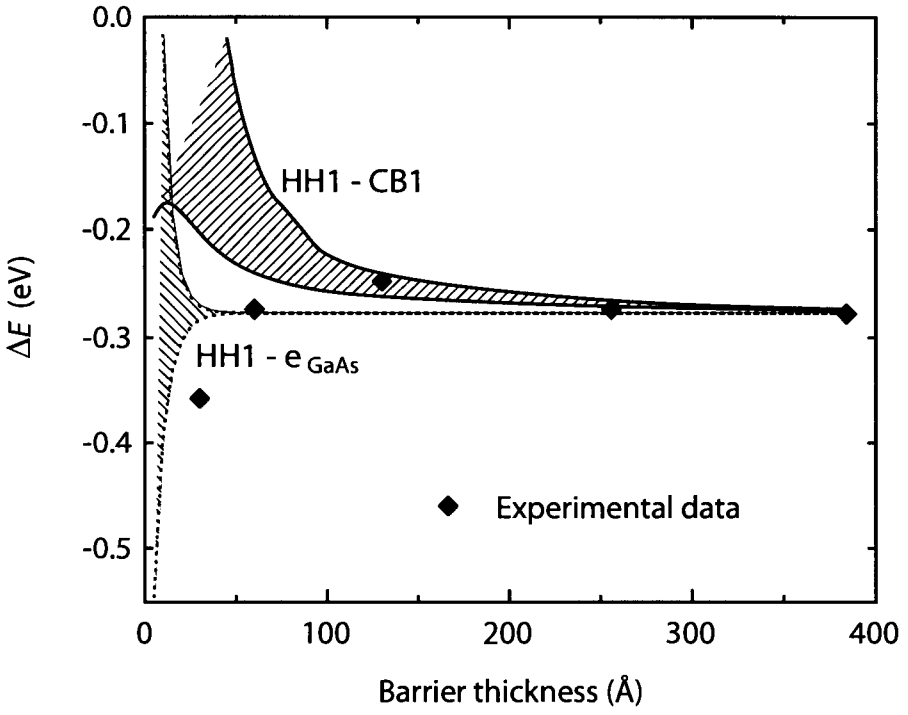

Figure 5.9: PL transition energy for $\sim$ 1 ML GaSb quantum wells as a function of barrier thickness. The shaded areas represent transitions between bands as calculated using the Kronig-Penney model (see text).

report coherent GaSb quantum well layers up to 11 Å thick, in contrast to the critical thickness of approximately 1 ML (3.25 Å) reported in this work (see section 4.1.4), suggesting that their thickness measurements from high-resolution XRD data reflect the total Sb incorporation in structures with strongly graded layers.

In order to study the effect of interwell coupling on the transition energy, the flashoff growth sequence was used to grow MQW samples with $\sim$ 1 ML GaSb layers and varying barrier thickness. These samples were grown with a 2000 Å GaAs cap layer above the MQW structure. The experimental PL peak energies are shown in Fig. 5.9. The shaded areas represent the range of possible transitions involving the lowest-energy minibands calculated using the modified Kronig-Penney (KP) model, with the differing effective masses taken into account as discussed in Sect. 5.3.3.

For simplicity, 1 ML wide quantum wells were assumed and the valence band offset was adjusted to match the experimental transition energy for the sample with the thickest barrier layers. For the band labelled "HH1 – e_{GaAs}", only the heavy hole confinement is included in the calculation, and the electrons are assumed to be at the GaAs conduction band edge. Due to the strong hole confinement the miniband converges to the single quantum well (SQW) level by about 50 Å. As the barrier thickness becomes small, however, the conduction band should also form a miniband with energy levels above the GaAs conduction band edge, due to the potential barriers associated with the GaSb layers. This effect is taken into account in the band labelled "HH1 – CB1". In a 6× MQW, the SQW energy level is split into 6 discrete energy levels rather than a continuous band, but the KP model should provide a reasonable estimate of the spread of the discrete levels. The calculation including the electron miniband predicts that the lowest allowed transition energy should increase as the barrier thickness decreases, down to about 10 Å where the hole confinement begins to dominate. The experimental data are not in agreement with this prediction; the trend appears closer to the curve taking into account only the heavy hole confinement. The sample with 130 Å barrier layers was found from XRD measurements to have a slightly lower Sb incorporation than the samples with thicker barriers, which can account for the higher observed transition energy (the reason for the lower Sb incorporation was not determined). The data may be explained by transitions between the heavy hole miniband and electrons at the conduction band edge in the GaAs capping layer, since this is the lowest accessible energy level for the electrons.

5.5.2 InAs/GaAs quantum wells

Fig. 5.10 shows the photoluminescence spectra of three 12× InAs/GaAs MQW samples grown at 550° C, with an EPD of 100 mW/cm^2. The PL line widths are considerably smaller than those of the samples with GaSb quantum wells, ranging from 6 meV for the sample with 1.29 ML InAs per period to 10 meV for the sample with 0.55 ML InAs per period. The line width decreases with the amount of InAs incorporation, in contrast to the GaSb/GaAs case. This trend also contradicts that observed previously for submonolayer InAs quantum wells in GaAs; an increase of the FWHM

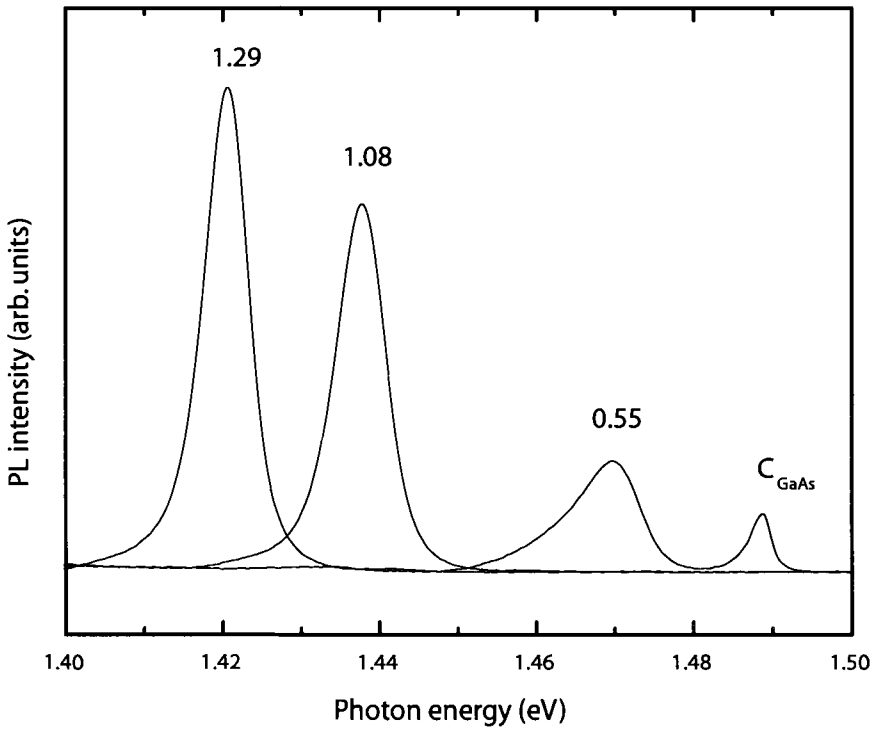

Figure 5.10: PL spectra of InAs/GaAs MQW samples, 100 mW/cm^2 excitation power density. The spectra are labelled with the In incorporation per period. The carbon donor-acceptor pair luminescence line is labelled C_{GaAs}.

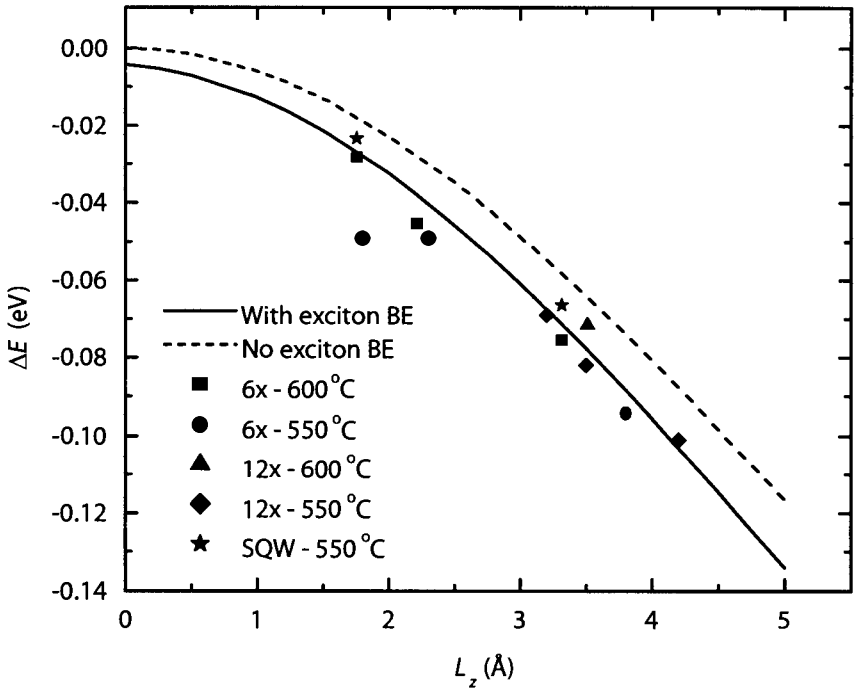

Figure 5.11: PL peak energy as a function of well width for InAs quantum wells.

from 0.7 meV for 0.3 ML InAs coverage to 7 meV for 1 ML InAs coverage was reported, and this was explained using a model of layer width fluctuations [96]. That work, however, investigated single quantum wells; in the MQW samples considered in the present work, fluctuations in the layer parameters from one period to the next may contribute additionally to the line width. The transition energies for InAs/GaAs quantum wells are closer to the GaAs bandgap than those observed for GaSb/GaAs quantum wells, which is a consequence of the smaller valence band offset of InAs on GaAs; the heavy hole binding energy increases significantly more than the electron binding energy for a given band offset, because of the larger effective mass of the heavy hole.

Fig. 5.11 shows the dependence of the PL peak energy on the In incorporation for InAs quantum well samples (ΔE represents the difference of the PL transition energy and the GaAs band gap). Experimental data are shown for a number of SQW, 6×, and

12× MQW samples, grown using conventional OMVPE sequences at either 550 °C or 600 °C. The barrier thicknesses in all of these samples are greater than 100 Å, so coupling effects are negligible. The In incorporation in the SQW samples was taken to be the same as that observed in MQW samples in which the InAs layer was grown for the same length of time; dynamical diffraction simulations of the rocking curves obtained from the SQW samples are consistent with this assumption. The curves are calculated using the EFA with the model solid theory band offsets for InAs on GaAs, with the well width scaled according to the In incorporation. In contrast to the type-II transitions in GaSb/GaAs quantum wells, the type-I transition energies calculated for InAs/GaAs quantum wells take into account the confinement of both the heavy holes and the electrons. For the dashed curve, the excitonic effect is not included. The solid line takes into account the exciton binding energy; the well width dependence of this energy is approximated by a linear interpolation between the bulk value of 4.2 meV in GaAs and 12.9 meV [91] for a 1 ML InAs quantum well. The solid curve fits the data reasonably well. In the case of InAs ultrathin quantum wells, the EFA and the model solid theory band offsets thus predict with reasonable accuracy the energy of the transition between the lowest bound electron and heavy hole states, as has also been reported previously [96, 109, 110]. The scatter in the data may result from inaccuracies in determining the well thickness and different degrees of structural imperfection, such as intermixing at the GaAs/InAs interface and layer roughness.

Chapter 6

Conclusions

The RDS signature of Sb-exposed GaAs, the effects of Sb surface segregation in GaAs, the 2D to 3D growth mode transition in strained GaSb layers, and the photoluminescence spectra of ultrathin GaSb/GaAs and InAs/GaAs quantum wells were investigated.

RDS data show that exposure of the GaAs(001) surface to TMSb under OMVPE conditions alters the surface reconstruction. The effect of small Sb concentrations appears to be a reduction of the As dimer concentration on both (2×4) and $c(4 \times 4)$ reconstructed surfaces. For larger Sb concentrations, characteristic positive features centered at 2.4 eV and 3.9 eV, which are definitely surface-related and may be due to transitions involving Sb dimers, appear in the RD spectra. During burial of the Sb-exposed surface with GaAs, Sb-related features persist in the RD spectrum, indicating the presence of a floating layer of Sb on the growing surface. The Sb surface layer desorbs under TBAs exposure, its concentration diminishing exponentially with a time constant of approximately 30 s under the conditions investigated.

GaAs overgrowth on GaSb layers leads to the formation of a floating layer of Sb on the surface, a fraction of which incorporates into the growing layer. This results in a graded, broadened quantum well if GaAs growth is continuous. XRD was used to study the partial incorporation of the floating layer Sb into the barrier layers of MQW structures. Dynamical diffraction simulations of XRD rocking curves and the dependence of the total Sb incorporation on barrier thickness are consistent with a high segregation coefficient, $\sigma = 0.95 \pm 0.02$. A small fraction (in the range 0.05–0.3) of

the Sb deposited during TMSb exposure is incorporated within the first monolayer of each period, or nominal quantum well position. The incorporation of Sb as an impurity during GaAs growth is well described by a one-dimensional segregation model, and forms graded $GaAs_{1-x}Sb_x$ barrier layers in the MQW structures. Cross-sectional TEM images showed that the interfaces are planar and that the layer parameters are consistent throughout the MQW structures.

The use of a flashoff growth sequence in which the GaSb layer is capped with a 4 ML GaAs layer, followed by a growth interruption under a supply of TBAs, effectively desorbs the Sb floating layer. Subsequent GaAs growth shows no evidence of Sb incorporation, within the limits of sensitivity of the high-resolution x-ray diffraction technique. The x-ray diffraction patterns of multiple quantum well structures grown using the flashoff sequence are in good agreement with the theoretical prediction for an ideal GaSb/GaAs heterostructure, demonstrating that the layer interfaces are abrupt and smooth. The growth of GaSb on GaAs occurs in the Stranski-Krastanov mode, with wetting of the substrate occurring for the first deposited monolayer. The transition to three-dimensional dot growth is energetically favourable for submonolayer GaSb coverage, above a value in the range 0.3–0.5 ML, but is kinetically limited. When capped immediately by GaAs, planar GaSb coverages of up to 1 ML were obtained.

Photoluminescence spectra of GaSb/GaAs MQW structures show a strong peak with a spectral position consistent with a type-II transition between heavy holes confined by the GaSb quantum well layers and electrons located in the surrounding GaAs matrix. Predictions of the transition energy using the EFA are strongly dependent on the extent of broadening of the quantum wells and on assumptions made about the band offsets. The data are, however, in reasonable agreement with calculated values assuming that the quantum wells grown by the flashoff sequence are slightly broadened by As-Sb intermixing and using previously published band offset estimates. Samples grown without growth interruptions exhibit a transition closer to the GaAs band gap than those grown with the flashoff sequence; this is qualitatively consistent with effective mass calculations for more strongly intermixed quantum wells. InAs/GaAs quantum wells show a strong type-I luminescence with a transition energy that agrees with calculations using the EFA as long as excitonic effects are taken into account.

Bibliography

[1] L. Esaki and R. Tsu, IBM J. Res. Dev. **14**, 61 (1970).

[2] I. Vurgaftman, J. R. Meyer, and L. R. Ram-Mohan, J. Appl. Phys. **89**, 5815 (2001).

[3] J. P. Silveira, J. M. Garcia, and F. Briones, J. Cryst. Growth **227–228**, 995 (2001).

[4] P. Y. Yu and M. Cardona, *Fundamentals of semiconductors : physics and materials properties* (Berlin ; New York: Springer, 1996).

[5] C. Weisbuch and B. Vinter, *Quantum semiconductor structures* (San Diego; London: Academic Press, 1991).

[6] N. N. Ledentsov, J. Böhrer, M. Beer, F. Heinrichsdorff, M. Grundmann, D. Bimberg, S. V. Ivanov, B. Ya. Meltser, S. V. Shaposhnikov, I. N. Yassievich, et al., Phys. Rev. B **52**, 14058 (1995).

[7] R. D. Wiersma, Master's thesis, Simon Fraser University (2002).

[8] C. A. Wang, S. Patnaik, J. W. Caunt, and R. A. Brown, J. Cryst. Growth **93**, 228 (1988).

[9] C. A. Wang, S. H. Groves, S. C. Palmateer, D. W. Weyburn, and R. A. Brown, J. Cryst. Growth **77**, 136 (1986).

[10] G. B. Stringfellow, *Organometallic Vapor Phase Epitaxy: Theory and Practice* (San Diego: Academic Press, 1989).

[11] D. E. Aspnes, IEEE J. Quantum Electron. **25**, 1056 (1989).

[12] E. Collett, *Polarized Light: Fundamentals and Applications* (New York: Marcel Dekker, 1993).

[13] D. K. Bowen and B. K. Tanner, *High Resolution X-ray Diffractometry and Topography* (London; Bristol, PA: Taylor & Francis, 1998).

[14] M. M. Woolfson, *An Introduction to X-ray crystallography* (Cambridge University Press, 1997).

[15] L. Tapfer and K. Ploog, Phys. Rev. B **40**, 9802 (1989).

[16] J. A. H. Stotz, Ph.D. thesis, Simon Fraser University (2002).

[17] D. Karaiskaj, Ph.D. thesis, Simon Fraser University (2002).

[18] W. Barvosa-Carter, A. S. Bracker, J. C. Culbertson, B. Z. Nosho, B. V. Shanabrook, L. J. Whitman, H. Kim, N. A. Modine, and E. Kaxiras, Phys. Rev. Lett. **84**, 4649 (2000).

[19] E. A. Wood, J. Appl. Phys **35**, 1306 (1964).

[20] I. Kamiya, D. E. Aspnes, L. T. Florez, and J. P. Harbison, Phys. Rev. B **46**, 15894 (1992).

[21] D. W. Kisker, G. B. Stephenson, I. Kamiya, P. H. Fuoss, D. E. Aspnes, L. Mantese, and S. Brennan, Phys. Stat. Sol. **152**, 9 (1995).

[22] I. Kamiya, L. Mantese, D. E. Aspnes, D. W. Kisker, P. H. Fuoss, G. B. Stephenson, and S. Brennan, J. Cryst. Growth **163**, 67 (1996).

[23] M. Pristovsek, T. Trepk, M. Klein, J.-T. Zettler, and W. Richter, J. Appl. Phys. **88**, 5554 (2000).

[24] Y.-C. Chang and D. E. Aspnes, Phys. Rev. B **41**, 12002 (1990).

[25] R. Eryiğit and I. P. Herman, Phys. Rev. B **56**, 9263 (1997).

[26] K. Uwai and N. Kobayashi, Phys. Rev. Lett. **78**, 959 (1997).

[27] A. I. Shkrebtii, N. Esser, W. Richter, W. G. Schmidt, F. Bechstedt, B. O. Fimland, and A. Kley, Phys. Rev. Lett **81**, 721 (1998).

[28] V. L. Berkovits, P. Chiaradia, D. Paget, A. B. Gordeeva, and C. Goletti, Surf. Sci. **441**, 26 (1999).

[29] V. L. Berkovits, P. Chiaradia, D. Paget, A. B. Gordeeva, and C. Goletti, Surf. Sci. **474**, 139 (2001).

[30] L. F. Lastras-Martínez, D. Rönnow, P. V. Santos, M. Cardona, and K. Eberl, Phys. Rev. B **64**, 245303 (2001).

[31] A. Balzarotti, E. Placidi, F. Arciprete, M. Fanfoni, and F. Patella, Phys. Rev. B **67**, 115332 (2003).

[32] S. M. Koch, O. Acher, F. Omnes, M. Defour, and B. Drévillon, J. Appl. Phys. **69**, 1389 (1991).

[33] K. Haberland, A. Kaluza, M. Zorn, M. Pristovsek, H. Hardtdegen, M. Weyers, J.-T. Zettler, and W. Richter, J. Cryst. Growth **240**, 87 (2002).

[34] R. Ludeke, Phys. Rev. Lett. **39**, 1042 (1977).

[35] F. Maeda, Y. Watanabe, and M. Oshima, Phys. Rev. B **48**, 14733 (1993).

[36] M. Sugiyama, S. Maeyama, F. Maeda, and M. Oshima, Phys. Rev. B **52**, 2678 (1995).

[37] P. Moriarty, P. H. Beton, Y.-R. Ma, M. Henini, and D. Woolf, Phys. Rev. B **53**, R16148 (1996).

[38] N. Esser, A. I. Shkrebtii, U. Resch-Esser, C. Springer, W. Richter, W. G. Schmidt, F. Bechstedt, and R. Del Sole, Phys. Rev. Lett. **77**, 4402 (1996).

[39] J. J. Zinck, E. J. Tarsa, B. Brar, and J. S. Speck, J. Appl. Phys. **82**, 6067 (1997).

[40] T. L. Lee and M. J. Bedzyk, Phys. Rev. B **57**, R15056 (1998).

[41] L. J. Whitman, B. R. Bennett, E. M. Kneedler, B. T. Jonker, and B. V. Shanabrook, Surf. Sci. **436**, L707 (1999).

[42] F. Maeda and Y. Watanabe, Phys. Rev. B **60**, 10652 (1999).

[43] F. Maeda and Y. Watanabe, J. Electron Spectrosc. Relat. Phenom. **101–103**, 293 (1999).

[44] W. G. Schmidt and F. Bechstedt, Phys. Rev. B **55**, 13051 (1997).

[45] W. G. Schmidt and F. Bechstedt, Surf. Sci. **377–379**, 11 (1997).

[46] G. P. Srivastava and S. J. Jenkins, Surf. Sci. **377–379**, 23 (1997).

[47] W. A. Harrison and E. A. Kraut, Phys. Rev. B **37**, 8244 (1988).

[48] Q. Xie, J. E. V. Nostrand, J. L. Brown, and C. E. Stutz, J. Appl. Phys. **86**, 329 (1999).

[49] J. Jönsson, F. Reinhardt, M. Zorn, K. Ploska, W. Richter, and J. Rumberg, Appl. Phys. Lett. **64**, 1998 (1994).

[50] A. R. Clawson and C. M. Hanson, J. Vac. Sci. Technol. B **14**, 3047 (1996).

[51] T. Nittono and F. Hyuga, J. Appl. Phys. **81**, 2607 (1997).

[52] Y. Q. Wang, Z. L. Wang, T. Brown, A. Brown, and G. May, J. Cryst. Growth **242**, 5 (2002).

[53] O. J. Pitts, S. P. Watkins, and C. X. Wang, J. Cryst. Growth **248**, 249 (2003).

[54] O. Brandt, K. Ploog, L. Tapfer, M. Hohenstein, R. Bierwolf, and F. Phillipp, Phys. Rev. B **45**, 8443 (1992).

[55] M. Copel, M. C. Reuter, E. Kaxiras, and R. M. Tromp, Phys. Rev. Lett. **63**, 632 (1989).

[56] J.-M. Gerard and J.-Y. Marzin, Phys. Rev. B **45**, 6313 (1992).

[57] G. R. Booker, P. C. Klipstein, M. Lakrimi, S. Lyapin, N. J. Mason, I. J. Murgatroyd, R. J. Nicholas, T.-Y. Seong, D. M. Symons, and P. J. Walker, J. Cryst. Growth **146**, 495 (1995).

[58] V. V. Chaldyshev, N. A. Bert, Yu. G. Musikhin, A. A. Suvorova, V. V. Preobrashenskii, M. A. Putamayo, B. R. Semyagin, P. Werner, and U. Gösele, Appl. Phys. Lett. **79**, 1294 (2001).

[59] M. Schultz, U. Egger, R. Scholz, O. Breitenstein, U. Gösele, and T. Y. Tan, J. Appl. Phys. **83**, 5295 (1998).

[60] T. Brown, A. Brown, and G. May, J. Vac. Sci. Technol. B **20**, 1771 (2002).

[61] M. Sato and Y. Horikoshi, J. Appl. Phys **69**, 7697 (1991).

[62] R. Arès, C. A. Tran, and S. P. Watkins, Appl. Phys. Lett. **67**, 1576 (1995).

[63] J. Gupta, S. Watkins, R. Arès, and G. Soerensen, J. Cryst. Growth **195**, 205 (1998).

[64] C. Giannini, L. Tapfer, S. Lagomarsino, J. C. Bouilliard, A. Taccoen, B. Capelle, M. Ilg, O. Brandt, and K. H. Ploog, Phys. Rev. B **48**, 11496 (1993).

[65] J. Gupta, J. Woicik, S. Watkins, K. E. Miyano, J. G. Pellegrino, and E. Crozier, J. Cryst. Growth **195**, 34 (1998).

[66] J. Gupta, S. Watkins, E. Crozier, J. Woicik, D. Harrison, D. Jiang, I. Pickering, and B. Karlin, Phys. Rev. B **61**, 2073 (2000).

[67] J. Steinshnider, J. Harper, M. Weimer, C.-H. Lin, S. S. Pei, and D. H. Chow, Phys. Rev. Lett. **85**, 4562 (2000).

[68] E. T. R. Chidley, S. K. Haywood, R. E. Mallard, N. J. Mason, R. J. Nicholas, P. J. Walker, and R. J. Walkerton, Appl. Phys. Lett. **54**, 1241 (1989).

[69] N. N. Ledentsov, J. Böhrer, M. Beer, M. Grundmann, F. Heinrichsdorff, D. Bimberg, S. V. Ivanov, B. Ya. Meltser, I. N. Yassievich, N. N. Faleev, et al., in

Proceedings of the 22nd International Conference on the Physics of Semiconductors (ICPS22), Vancouver, BC, Canada, 1994, edited by D. J. Lockwood (Singapore: World Scientific, 1995).

[70] B. R. Bennett, B. V. Shanabrook, and M. E. Twigg, J. Appl. Phys **85**, 2157 (1999).

[71] K. Suzuki, R. A. Hogg, and Y. Arakawa, J. Appl. Phys **85**, 8349 (1999).

[72] B. M. Kinder and E. M. Goldys, Appl. Phys. Lett **73**, 1233 (1998).

[73] L. Müller-Kirsch, U. W. Pohl, R. Heitz, H. Kirmse, W. Neumann, and D. Bimberg, J. Cryst. Growth **221**, 611 (2000).

[74] L. Müller-Kirsch, R. Heitz, U. W. Pohl, D. Bimberg, I. Häusler, H. Kirmse, and W. Neumann, Appl. Phys. Lett. **79**, 1027 (2001).

[75] D. Pal, E. Towe, and S. Chen, Appl. Phys. Lett. **78**, 4133 (2001).

[76] A. Krost, J. Bläsing, F. Heinrichsdorff, and D. Bimberg, Appl. Phys. Lett **75**, 8 (1999).

[77] R. Kaspi and K. R. Evans, J. Cryst. Growth **175/176**, 838 (1997).

[78] P. M. Thibado, B. R. Bennett, M. E. Twigg, B. V. Shanabrook, and L. J. Whitman, J. Vac. Sci. Technol. A **14**, 885 (1995).

[79] B. R. Bennett, R. Magno, and B. V. Shanabrook, Appl. Phys. Lett. **68**, 505 (1996).

[80] B. R. Bennett, P. M. Thibado, M. E. Twigg, E. R. Glaser, R. Magno, B. V. Shanabrook, and L. J. Whitman, J. Vac. Sci. Technol. B **14**, 2195 (1996).

[81] R. A. Hogg, K. Suzuki, K. Tachibana, L. Finger, K. Hirakawa, and Y. Arakawa, Appl. Phys. Lett. **72**, 2856 (1998).

[82] T. Wang and A. Forchel, J. Appl. Phys **85**, 2591 (1998).

[83] R. P. Mirin, A. Roshko, M. van der Puijl, and A. G. Norman, J. Vac. Sci. Technol. B **20**, 1489 (2002).

[84] K. Taira, H. Kawai, I. Hase, K. Kaneko, and N. Watanabe, Appl. Phys. Lett **53**, 495 (1988).

[85] M. A. Tischler, N. G. Anderson, and S. M. Bedair, Appl. Phys. Lett **49**, 1199 (1986).

[86] M. Sato and Y. Horikoshi, J. Appl. Phys **66**, 851 (1989).

[87] P. D. Wang, N. N. Ledentsov, C. M. Sotomayor Torres, P. S. Kop'ev, and V. M. Ustinov, Appl. Phys. Lett **64**, 1526 (1994).

[88] J. M. Gerard and J. Y. Marzin, Appl. Phys. Lett **53**, 568 (1988).

[89] M. Yano, K. Yoh, T. Iwawaki, Y. Iwai, and M. Inoue, J. Cryst. Growth **111**, 397 (1991).

[90] J. M. Moison, C. Guille, F. Houzay, F. Barthe, and M. Van Rompay, Phys. Rev. B **40**, 6149 (1989).

[91] R. C. Iotti and L. C. Andreani, Phys. Rev. B **57**, R15072 (1998).

[92] O. Brandt, H. Lage, and K. Ploog, Phys. Rev. B **43**, 14285 (1990).

[93] O. Brandt, G. C. La Rocca, A. Heberle, A. Ruiz, and K. Ploog, Phys. Rev. B **45**, 3803 (1992).

[94] M. V. Belousov, N. N. Ledentsov, M. V. Maximov, P. D. Wang, I. N. Yasievich, N. N. Faleev, I. A. Kozin, V. M. Ustinov, P. S. Kop'ev, and C. M. Sotomayor Torres, Phys. Rev. B **51**, 14346 (1995).

[95] W. Li, Z. Wang, J. Liang, B. Xu, Z. Zhu, Z. Yuan, and J. Li, Appl. Phys. Lett. **67**, 1874 (1995).

[96] C. A. Tran, R. A. Arès, V. A. Karasyuk, S. P. Watkins, G. Letourneau, and R. Leonelli, Phys. Rev. B **55**, 4633 (1997).

[97] J. H. Lee, K. Y. Hsieh, and R. M. Kolbas, Phys. Rev. B **41**, 7678 (1990).

[98] A. R. Goñi, M. Stroh, C. Thomsen, F. Heinrichsdorff, V. Türck, A. Krost, and D. Bimberg, Appl. Phys. Lett. **72**, 1433 (1998).

[99] H. Kurakake, T. Uchida, S. Kubota, H. Soda, and S. Yamazaki, IEEE J. Quantum Electron. **30**, 909 (1994).

[100] T. Y. Wang, E. H. Reihlen, H. R. Jen, and G. B. Stringfellow, J. Appl. Phys. **66**, 5376 (1989).

[101] T. Nittono, S. Sugitani, and F. Hyuga, J. Appl. Phys. **78**, 5387 (1995).

[102] T. K. Sharma, B. M. Arora, M. R. Gokhale, and S. Rajgopalan, J. Cryst. Growth **221**, 509 (2000).

[103] R. Kúdela, M. Kučera, B. Olejníková, P. Eliáš, S. Hasenöhrl, and J. Novák, J. Cryst. Growth **212**, 21 (2000).

[104] V. Duez, O. Vanbésien, D. Lippens, D. Vignaud, X. Wallart, and F. Mollot, J. Appl. Phys. **85**, 2202 (1999).

[105] J. P. Loehr, *Physics of Strained Quantum Well Lasers* (Boston; Dordrecht; London: Kluwer Academic Publishers, 1998).

[106] M. Di Ventra and K. A. Mäder, Phys. Rev. B **55**, 13148 (1997).

[107] O. Brandt, R. Cingolani, H. Lage, G. Scamarcio, L. Tapfer, and K. Ploog, Phys. Rev. B **42**, 11396 (1990).

[108] R. Cingolani, O. Brandt, L. Tapfer, G. Scamarcio, G. C. La Rocca, and K. Ploog, Phys. Rev. B **42**, 3209 (1990).

[109] M. Ilg, M. I. Alonso, A. Lehmann, K. H. Ploog, and M. Hohenstein, J Appl. Phys. **74**, 7188 (1993).

[110] P. D. Wang, N. N. Ledentsov, C. M. Sotomayor Torres, I. N. Yassievich, A. Pakhamov, A. Yu. Egorov, P. S. Kop'ev, and V. M. Ustinov, Phys. Rev. B **50**, 1604 (1994).

[111] M. Geddo, M. Capizzi, A. Patanè, and F. Martelli, J. Appl. Phys. **84**, 3374 (1998).

[112] V. Albe and L. J. Lewis, Physica B **301**, 233 (2001).

[113] R. P. Schneider, Jr. and B. W. Wessels, J. Appl. Phys. **70**, 405 (1991).

[114] M.-E. Pistol, M. G. D. Hessman, and L. Samuelson, Phys. Rev. B **45**, 3628 (1992).

[115] D. Hessman, M.-E. Pistol, J. Olajos, and L. Samuelson, Phys. Rev. B **49**, 17118 (1994).

[116] M. G. Burt, Phys. Rev. B **50**, 7518 (1994).

[117] M. G. Burt, J. Phys.: Condens. Matter **4**, 6651 (1992).

[118] M. G. Burt, J. Phys.: Condens. Matter **11**, R53 (1999).

[119] L. G. Shantharama, A. R. Adams, C. N. Ahmad, and R. J. Nicholas, J. Phys. C: Solid State Physics **17**, 4429 (1984).

[120] G. Ji, S. Agarwala, D. Huang, J. Chyi, and H. Morkoç, Phys. Rev. B **38**, 10571 (1988).

[121] A. D. Prins, D. J. Dunstan, J. D. Lambkin, E. P. O'Reilly, A. R. Adams, R. Pritchard, W. S. Truscott, and K. E. Singer, Phys. Rev. B **47**, 2191 (1993).

[122] M. Peter, K. Winkler, M. Maier, N. Herres, J. Wagner, D. Fekete, and K. H. Bachem, Appl. Phys. Lett. **67**, 2639 (1995).

[123] G. Liu, S.-L. Chuang, and S.-H. Park, J. Appl. Phys. **88**, 5554 (2000).

[124] R. Teissier, D. Sicault, J. C. Harmand, G. Ungaro, G. L. Roux, and L. Largeau, J. Appl. Phys. **89**, 5473 (2001).

[125] B. R. Nag, *Physics of Quantum Well Devices* (Boston; Dordrecht; London: Kluwer Academic Publishers, 2000).

[126] C. G. Van de Walle, Phys. Rev. B **39**, 1871 (1989).

[127] S. Subramanian, B. M. Arora, A. K. Srivastava, G. Fernando, and S. Banerjee, J. Appl. Phys. **74**, 7618 (1993).

[128] R. Colombelli, V. Piazza, A. Badolato, M. Lazzarino, F. Beltram, W. Schoenfeld, and P. Petroff, Appl. Phys. Lett. **76**, 1146 (2000).

[129] J. C. Woicik, J. G. Pellegrino, S. H. Southworth, P. S. Shaw, B. A. Karlin, C. E. Bouldin, and K. E. Miyano, Phys. Rev. B **52**, R2281 (1995).

[130] R. de L. Kronig and W. G. Penney, Proc. Roy. Soc. (London) A **130**, 499 (1931).

[131] R. L. Greene, K. K. Bajaj, and D. E. Phelps, Phys. Rev. B **29**, 1807 (1984).

[132] G. Bastard, E. E. Mendez, L. L. Chang, and L. Esaki, Phys. Rev. B **26**, 1974 (1982).

[133] R. Zimmermann and D. Bimberg, J. Physique IV (Colloque C5, Suppl. J. Physique II) **3**, 261 (1993).

[134] J. Böhrer, A. Krost, R. Heitz, F. Heinrichsdorff, L. Eckey, D. Bimberg, and H. Cerva, Appl. Phys. Lett. **68**, 1072 (1996).

[135] R. Planel, R. Teissier, and F. Mollot, J. Physique IV (Colloque C5, Suppl. J. Physique II) **3**, 159 (1993).

[136] W. W. Chow and H. C. Schneider, Appl. Phys. Lett. **78**, 4100 (2001).

[137] W. W. Chow, O. B. Spahn, H. C. Schneider, and J. F. Klem, IEEE J. Quantum Electron. **37**, 1178 (2001).

[138] I. V. Bradley, J. P. Creasey, and K. P. O'Donnell, J. Cryst. Growth **184/185**, 728 (1998).

[139] O. Madelung, ed., *Semiconductors: Group IV Elements and III-V Compounds* (Berlin: Springer-Verlag, 1991).

[140] F. Hatami, M. Grundmann, N. N. Ledentsov, F. Heinrichsdorff, R. Heitz, J. Böhrer, D. Bimberg, S. S. Ruvimov, P. Werner, V. M. Ustinov, et al., Phys. Rev. B **57**, 4635 (1998).

[141] Motlan and E. M. Goldys, Appl. Phys. Lett. **79**, 2976 (2001).